Photogeneration of singlet oxygen by gold nanoparticles

Thesis submitted in accordance with the requirements of the University of Liverpool for the degree of Doctor in Philosophy by:

Tiago Entradas

September 2019

“If you go back a few hundred years, what we take for granted today would seem like magic; being able to talk to people over long distances, to transmit images, flying, accessing vast amounts of data like an oracle. These are all things that would have been considered magic a few hundred years ago.”

Elon Musk
CEO Tesla, Inc.

DECLARATION

I hereby certify that this dissertation constitutes my own product, that where the language of others is set forth, quotation marks so indicate, and that appropriate credit is given where I have used the language, ideas, expressions or writings of another.

I declare that the dissertation describes original work that has not previously been presented for the award of any other degree of any institution.

Signed,

Tiago Entradas

ABSTRACT

Photogeneration of singlet oxygen by gold nanoparticles

By

Tiago Entradas

Photodynamic medicine has been known for more than 5000 years when Egyptians, Chinese and Indians used sunlight in combination with some “magic” plants to treat various disorders. Contemporary photodynamic therapy began in the 1900s, received its revival in 1970 due to hematoporphyrin derivative (HpD), and it is now an FDA approved therapeutic option for skin, early lung, and advanced oesophagal cancer in several countries. Although a few photosensitisers have been approved for clinical use, they suffer from several drawbacks such as biological and light instability and lack specificity toward specific types of cells.

In this thesis work, we propose plasmonic gold nanoparticles as photosensitisers to overcome the drawbacks of first- and second-generation photosensitiser and investigate their $^1O_2$ photogeneration efficiency upon CW-laser irradiation at their surface plasmon resonance. First, the singlet oxygen sensitivity of two molecular probes (ABDA and DPBF) in different solvent systems was determined, using Rose Bengal as a photosensitiser. Second, we showed conclusively, for the first time, that gold nanoparticles photogenerate $^1O_2$, and that the quantum yield is extremely small. Lastly, gold nanoparticles were functionalized with bovine serum albumin, and their singlet oxygen quantum yield re-evaluated. Our irradiation results showed that the protein corona, i.e. bovine serum albumin, did not affect the $^1O_2$ production.

Acknowledgements

Personally, this project and thesis represent the apogee and completion of a fantastic journey. It is the pinnacle of long-lasting hours of research, group meetings, laughs, sweat and tears which I humbly pursued the last three and a half years, none of which would have been possible without the help and guidance from several individuals to whom I am gratefully indebted. There are not enough words that can adequately describe my gratitude to those who constructively helped me during this thorny path.

First and foremost, I wish to express my deepest gratitude to my supervisor, Dr Martin Volk, for the opportunity to embrace his project, join his research group and to open the door to this challenging subject – Photo Chemistry. It was a privilege to have him as my mentor, and I am genuinely grateful for the time and effort he devoted to guiding me in a wide variety of subjects ranging from research problems to career direction. He has been fantastic in training me in the process of scientific writing, and his patience and careful proofreading have been invaluable in the development of this document. I also wish to thank my second supervisor, Dr Mathias Brust, for all the support and guidance throughout this project.

Secondly, I wish to express my gratitude to my assessors, Dr Heike Arnolds and Dr Tony Lopez-Sanchez, for the scientific advice during my PhD.

Next, I would like to thank Gareth and Etta, Luca, Marcel, Sam, Edyta, Emile, Matt, Sean, Dom, Haitham, Yuri and Ioritz for the laughs and giggles we had in the tea room, especially the “scientific” description of surface plasmon resonance or plasmonic enhancement that Luca gifted us with or the “story time” always kindly presented by Emile.

The love and company of my family during this period have been invaluable. The constant support and comprehension that I received from both my parents and my sister since I moved to the United Kingdom are priceless, and I hereby express them my sincerest gratitude.

Finally, to my dear Monica, for the support, dedication and boundless patience. She filled my life with love, happiness and joy, for being my inspiration and making everything worth it.

Table of contents

Table of figures

Table of tables

List of abbreviations and symbols

A – Absorbance

N_A – Avogadro constant

k_q – Bimolecular rate constant of the physical quenching by the sensor probe

k_r – Bimolecular rate constant of the chemical quenching by the sensor probe

BSA – Bovine serum albumin

CTAB – cetyltrimethylammonium bromide

CW – Continuous wave

D_2O – Deuterium oxide

DCS – Differential centrifugal sedimentation

D – Diffusion coefficients

k – Diffusion-limited rate constant of a bimolecular reaction

DMSO – Dimethyl sulfoxide

EtOH – Ethanol

Ɛ – Extinction coefficient

k_a – First order rate constant of the electron-electron scattering process

FTIR – Fourier-transform infrared spectroscopy

AuNPs – Gold nanoparticles

AuNPs@BSA – Gold nanoparticles functionalized with Bovine serum albumin

HCl – Hydrochloric acid

OH· – Hydroxyl radical

IC – Internal conversion

ISC – Intersystem crossing

LP – Laser power

Φ_{max} – Maximum $^1O_2$ quantum yield of AuNPs

ΔA – Measured absorbance change

S – Molecular probe

NP – Nanoparticle

NPs – Nanoparticles

HNO_3 – Nitric acid

N_2 – Nitrogen

NMR – Nuclear magnetic resonance spectroscopy

d – Optical path-length

O_2 – Oxygen

K_s – Oxygen solubility

PDT – Photodynamic therapy

PS – Photosensitiser

PTT – Photothermal therapy

RNO – p-nitrosodimethylaniline

PEG – Polyethylene glycol

QY – Quantum yield

R – Radius

N_{abs} – Rate of photon absorption

ROS – Reactive oxygen species

RB – Rose Bengal

V – Sample volume

Φ_S – Sensitivity of the $^1O_2$ sensor

$^1O_2$ – Singlet oxygen

k_0 – Singlet oxygen decay rate constant

SOSG – Singlet oxygen sensor green

NaN_3 – Sodium azide

$O_2^{\cdot-}$ – Superoxide radical anion

SPR – Surface plasmon resonance

SERS – Surface-enhanced Raman scattering

Δt – Time interval

UV-Vis – Ultraviolet-visible spectroscopy

η – Viscosity

H_2O – Water

DPBF – 1,3-diphenylisobenzofuran

Φ_{RB} – $^1O_2$ quantum yield of RB

ADPA – 9,10-anthracene dipropionic acid

ABDA – 9,10-anthracenediyl-bis(methylene)dimalonic acid

DPA – 9,10-diphenylanthracene

Chapter 1

1. Introduction

Cancers, chronic cardiovascular and respiratory diseases, and diabetes are the "plagues" of the 21st century.[1] They are the biggest causes of death worldwide. Specifically, for cancer, the number of diagnosed patients is increasing, expected to reach 22 million cases by 2030, according to the World Health Organization.[2,3] Therefore, it is essential not only to prevent, control or even reduce the number of cancer cases and cancer-related deaths, but also to improve the life quality of the patients diagnosed with cancer. However, despite all efforts applied to research in the development of new strategies for prevention, early detection, diagnosis, and treatment of cancer, the available therapeutic options remain the same as twenty years ago, namely surgery, radiotherapy, and chemotherapy.[3,4] In other words, there is a wall that needs to be surpassed, and it is essential to broaden our horizons and put more emphasis on other existing but underappreciated treatments or develop new therapeutic methods.

Photodynamic therapy (PDT) is an example of an underappreciated FDA approved therapy available nowadays. Its availability is quite limited, and it is rarely mentioned as a possible therapeutic option for the patient. It is available almost exclusively to research/academic hospitals.[5] Clinical studies suggest that PDT can be a potent tool against early-stage tumours and increase the survival probability in cases where cancers are inoperable.[5]

The purpose of this thesis is to determine the efficiency of gold nanoparticles (AuNPs) as photosensitisers (PS) for a PDT application.

1.1 Photodynamic therapy

PDT is a localised therapy that induces oxidative damage to cells by photochemically generated reactive oxygen species (ROS). Its success derives from the

high reactivity and short lifetime of ROS in the cell environment. It involves three key components, light, a photosensitiser and tissue oxygen. When these three components are present, a photochemical reaction is initiated by a PS, after being excited by the appropriate wavelength of light. Oxygen is then excited by the excited PS to generate ROS, which are toxic to cells.[6]

1.1.1 Advantages and limitations

When compared to conventional cancer therapies, PDT has several advantages. It has no long-term side effects, which can significantly improve the patient's quality of life.[7] For cancer at an advanced stage, PDT can lengthen survival significantly and, for early or localised diagnosis, it can be a selective and curative therapy with many advantages over alternative treatments.[8] It is less invasive than surgical procedures, and the side effects are milder and last significantly shorter than those of chemo- or radiotherapy.[7] PDT can be directed precisely to a target tissue due to its dual selectivity – the PS can be tailored to accumulate specifically in the tumour cells, and it is only toxic/activated upon irradiation.[9] PDT can be repeated several times in the same location, unlike radiation, and more importantly, it generally costs less than other cancer treatments.[8,10] It has also been shown that tissues targeted with PDT heal faster with little or no scarring, which improves patient recovery.[11,12] Lastly, PDT does not damage major vascular structures, and it does not cause nerve damage.[12]

However, similar to every therapy, PDT has some limitations as well. The photodynamic effect only takes place selectively at the irradiated location, which makes it unfeasible for patients with disseminated metastases because available technology does not allow full-body irradiation with the appropriate light intensity.[8] Also, the first- and second-generation PSs can cause minor photosensitivity to the eyes and skin, are biologically unstable due to cellular metabolism, which significantly decreases the drugs' efficiency, and are photo unstable, i.e. they bleach in light, either by direct photodegradation or because the ROS generated upon excitation of the PS react with the PS itself, causing its degradation which further reduces its efficiency.[10,13,14] Oxygenation of the tissue and tumour cells is also crucial for the photodynamic effect. Tumour areas surrounded by necrotic tissue or solid tumour masses usually have less oxygen, which

impairs the therapy. Moreover, light delivery to deep tumours is hard to achieve due to low tissue penetration of visible light.[15]

The advantages and limitations of PDT are summarised in Table 1.1.

Table 1.1 – Summary of the advantages and limitations of PDT.

Advantages	Limitations
• Fewer side effects when compared with other therapeutic options • Less invasive • Shorter treatment time • Double selectivity • Repeatable • Little to no scarring after healing • Lower costs when compared with other treatments	• Some degree of photosensitivity after treatment • Treatment efficiency dependent on light delivery • Tissue oxygenation • Impossible to apply to metastatic cancers • PS suffers from photo instability and biological metabolization

1.1.2 Mechanism of action

During PDT, ROS production occurs upon excitation of a PS with light at an appropriate wavelength in the presence of O_2. Figure 1.1 illustrates a schematic Jablonski diagram for the excitation of a PS by light.

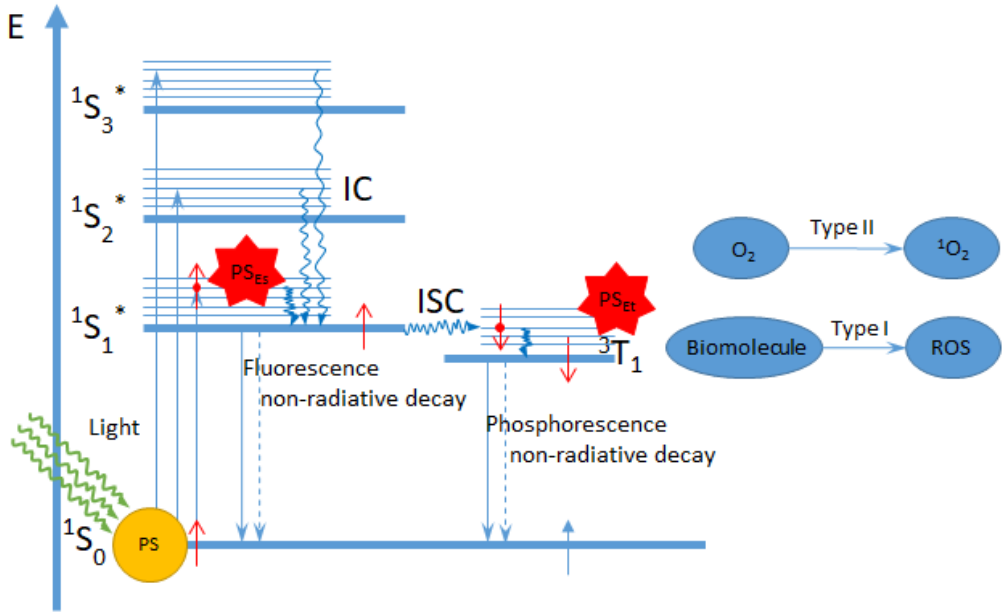

Figure 1.1 - Type I and type II reactions in PDT. Schematic Jablonski diagram describing the PDT mechanism of action following light absorption by a PS.

When a PS, usually a dye, is irradiated, it can be excited to a vibrationally excited higher electronic state (singlet state) without changing the spin (PS_{Es}), followed by vibrational relaxation, leaving the excited molecule in the vibrationally equilibrated electronically excited state. At this point, several processes can occur. The ground state can be regenerated by internal conversion (IC), releasing the energy as heat, or by the emission of a photon (fluorescence). Alternatively, if it is thermodynamically and kinetically favourable, intersystem crossing (ISC) can occur, changing the spin state to populate the lowest energy triplet state (PS_{Et}). At this stage, PS regeneration can be achieved by the emission of a photon (phosphorescence) or by releasing the energy as heat. Additionally, there is a possibility that the photosensitiser (PS_{Et}) is quenched directly by molecular oxygen, which leads to singlet oxygen ($^1O_2$), following the Dexter mechanism, also known as Type II reaction.[17,18]

The Dexter electron exchange mechanism is a quenching mechanism in which an excited electron is transferred from a donor (PS_{Et}) to an acceptor (in this case, molecular oxygen). It can be described as a simultaneous transfer of an electron from one of the $2\pi^*$ molecular orbitals from O_2 to a photogenerated hole in the PS, and of an electron with opposite spin from a high energy excited PS level to the other $2\pi^*$ orbital, to generate a $^1\Delta_g$ singlet state, as shown in Figure 1.2. This process requires an overlap of wavefunctions between donor and acceptor and generates a singlet state of oxygen from a ground state oxygen (triplet state).

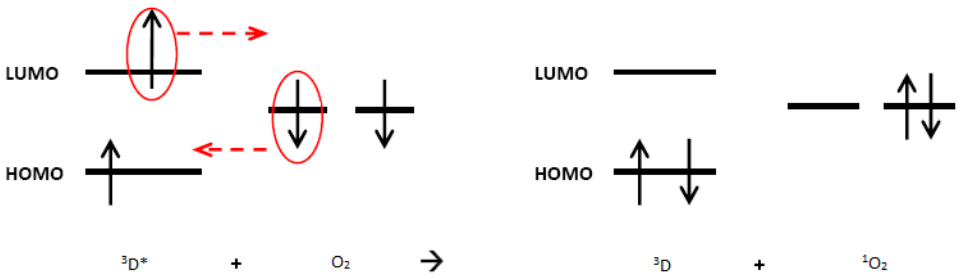

Figure 1.2 – Scheme of the Dexter electron exchange mechanism for the excitation of O_2 to its singlet state ($^1O_2$) by a triplet donor. Image adapted from [19].

Another possible pathway to quench the triplet state of the donor ($^3D^*$) is via Forster resonance energy transfer. In this case, the excess energy would be transferred from the donor to the acceptor through nonradiative dipole-dipole coupling.

As shown in Figure 1.1, there is also the possibility of the photosensitiser (PS_{Et}) to be quenched by a biomolecule – Type I reaction. This pathway can lead to the oxidation or reduction of the biomolecule, which in contact with oxygen might lead to the generation of superoxide radical anion ($O_2^{\cdot-}$), or follow a radical process generating hydroxyl radical (OH·). Finally, $O_2^{\cdot-}$ has also been reported to be produced directly by electron transfer from PS_{Et}.[20]

Effectively, independent of the reaction type, the PS acts as an antenna that absorbs light to activate the surrounding oxygen and returns to its ground state at the end of the process. As such, it can be activated repeatedly during the therapeutic period until it is photobleached, metabolised or eliminated from the cells or tissue. According to the literature, the predominant mechanism to induce cytotoxicity in PDT is the type II reaction. Therefore, the most crucial cytotoxic agent generated during PDT is $^1O_2$.[21,22]

1.1.3 Singlet oxygen and its detection

$^1O_2$ has a vital role in many processes in the field of biology, material science, chemistry and medicine. $^1O_2$ is highly reactive and readily reacts with unsaturated organic molecules in a spin-allowed process to generate peroxides.[23] The first excited state of oxygen, $^1O_2$, is a singlet with two electrons with an opposite spin in the same molecular orbital, as shown in Figure 1.3.

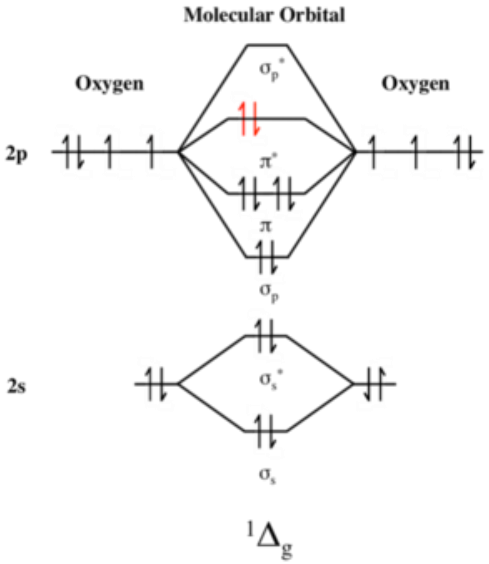

Figure 1.3 - Molecular orbital diagram of $^1O_2$. Image adapted from [24].

$^1O_2$ has only one direct detection method, via the phosphorescence emission at 1270 nm[25] and, by time-resolved experiments, it was possible to determine the $^1O_2$ lifetime (i.e. the inverse of the experimental decay rate constant, k_0) in different solvents.[26] The detection of $^1O_2$ has also been achieved by indirect measurements based on its chemical trapping. This methodology relies on the observation of a signal change produced by a chemical reaction between a chemical probe and $^1O_2$. One of the most commonly used chemical traps in the literature is 1,3-diphenylisobenzofuran (DPBF).[27–29] More recently, anthracene moieties, such as 9,10-diphenylanthracene (DPA)[30–32], 9,10-anthracenediyl-bis(methylene)dimalonic acid (ABDA)[33,34] or singlet oxygen sensor green (SOSG)[35–37] have also been reported as $^1O_2$ chemical traps, see Figure 1.4.

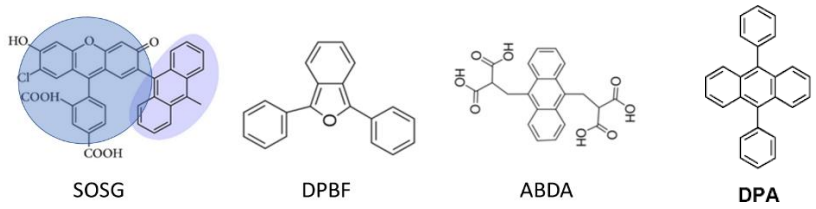

Figure 1.4 – SOSG, DPBF, ABDA and DPA molecular structures.

DPBF is a molecule that reacts irreversibly with $^1O_2$ to form an endoperoxide (see Figure 1.5) and has the advantage of having negligible physical quenching effects.[38,39] However, DPBF is insoluble in water, which limits its use in aqueous solution, and reacts with other ROS.[40]

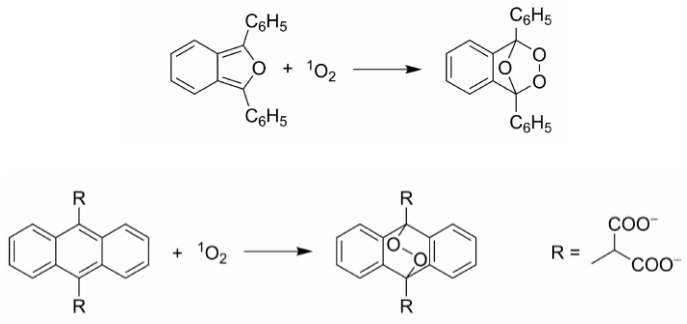

Figure 1.5 – Reaction of $^1O_2$ with DPBF (top) and ABDA (bottom).

ABDA and DPA are anthracene moieties that also react with $^1O_2$ to form endoperoxides, Figure 1.5. In contrast to DPBF, this family of molecules reacts specifically with $^1O_2$ and ABDA is water-soluble.[41,42] However, they have the drawbacks of suffering from physical quenching effects, and their reactivity is significantly smaller when compared to DPBF, as we will show in chapter 2.

More recently, a new fluorescence $^1O_2$ probe has been commercialised by Invitrogen/Molecular Probes, SOSG. SOSG is a probe composed of an anthracene moiety (electron donor) that quenches the fluorescence of the fluorochrome (electron acceptor) through electron transfer, as highlighted in Figure 1.4. Once the anthracene moiety traps $^1O_2$, the resultant O_2 adduct does not donate electrons anymore, and the fluorescence is recovered. Invitrogen claims that SOSG has good selectivity for $^1O_2$, and its response towards other ROS is negligible. However, the literature showed that SOSG is unstable under irradiation because it can act as a photosensitiser, generating $^1O_2$, which complicates its application.[43]

During this project, DPBF and ABDA were chosen to detect $^1O_2$. DPBF was selected because it is the most common $^1O_2$ probe described in the literature and ABDA because it reacts specifically with $^1O_2$, and it is water-soluble. Mechanistically, the reaction of $^1O_2$ with DPBF and ABDA typically occurs by the formation of a 2,5-endoperoxide, as shown in Figure 1.5. This species generally evolves into a final product or a mixture of products. At the moment, there is not a consensus regarding which final products are generated after the generation of the endoperoxide. The recognised reactions and rearrangements that follow the production of the endoperoxide for DPBF and ABDA have been summarised by Clennan and Pace[23] and You[44], respectively. Despite the uncertainty, the transformation into the endoperoxide and its products leads to a decrease of the absorbance of the aromatic compound, which is used to monitor the $^1O_2$ generation by a PS.

1.2 Gold nanoparticles

Gold is one of the least chemically reactive metals. It does not oxidise or burn in the air even when heated, and it is inert to strong alkalis and virtually all acids apart from selenic acid and aqua regia.[45,46]

The first information on colloidal gold traces back as early as the fifth and fourth centuries B.C. and one of its uses was for medical purposes, the "gold solution" or "liquid gold" as the Chinese and Indians used to call it.[47] Yet, the first person to report the controlled synthesis of AuNPs (nanospheres) was Turkevich *et al.* in 1951.[48] The synthesis method was later improved by Frens *et al.*[49]

The synthesis method is based on the reduction of tetrachloroauric acid ($HAuCl_4$) by trisodium citrate. This method allows the synthesis of AuNPs with a diameter which can range from 9 to 120 nm, depending on the relative amount of the reactants in the solution, the reaction time and the strength of the reductant. The citrate ions work both as a reducing agent, as well as a stability agent due to the negative charge which covers the NPs surface preventing the AuNPs' aggregation in aqueous solution.[50]

1.2.1 Optical properties

One of the most impressive and useful characteristics of AuNPs is their interaction with light. AuNPs absorb and scatter light with remarkable efficiency. This strong interaction with light happens due to the conduction electrons undergoing a collective coherent and resonant oscillation when they are excited by light at specific wavelengths (Figure 1.6).[51]

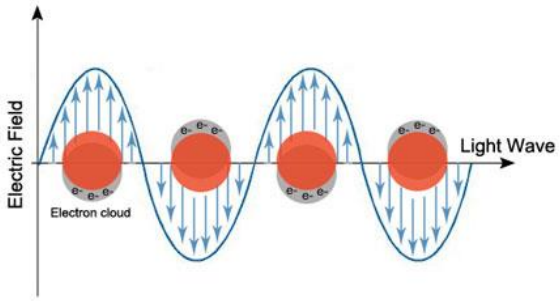

Figure 1.6 – Illustration of the SPR upon excitation of AuNPs. Image taken from [52].

The collective oscillation of conduction electrons in metals are defined as plasmons, and this coherent oscillation is defined as surface plasmon resonance (SPR), and it is quantitatively described by Mie theory.[51] According to the Fermi model, plasmons can be characterised as a negatively charged electron cloud displaced from

their equilibrium position around a metal lattice made of positively charged ions. When this effect occurs at the surface, the plasmons are called surface plasmons, which can be excited by electromagnetic waves. When the size of a AuNP is small in comparison to the resonant electromagnetic wavelength, the electric field throughout the particle is uniform, which leads to a coherent electron cloud polarisation in the nanoparticle (NP), hence an excitation of the dipolar plasmon oscillations. As the particles grow bigger, the electric field distribution throughout the NP becomes less uniform, and the coherence in the electron cloud polarisation starts to decrease which leads to an excitation of multipolar plasmon oscillations, hence the redshift and broadening of the SPR peak.[51]

The SPR of AuNPs can be observed by optical absorption spectroscopy (Figure 1.7). For AuNPs with a diameter of 10 to 30 nm, the position of the SPR peak of AuNPs is centred around 520 nm, and it is overlapped with the absorption of interband transitions, namely by excitation of electrons from the occupied 5d band to the unoccupied levels of the 6s and 6p band of the metal. For larger NPs, the band shifts to higher wavelengths.

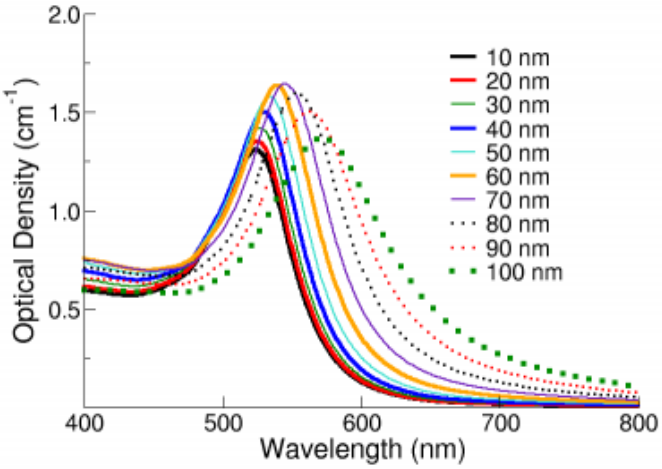

Figure 1.7 – Absorption spectra of AuNPs with different sizes, ranging from 10 nm to 100 nm. Image taken from [53].

The extinction coefficient of the SPR band scales with the number of conduction electrons in the AuNP, where each gold atom contributes one conduction electron. Since many electrons contribute to the SPR effect, the absorption and scattering cross-section of gold is extremely high when compared with a typical organic chromophore molecule.[51] This effect grants AuNPs a high efficiency in converting light to heat and the ability to amplify the electromagnetic field near the metal surface. Additionally, the SPR position and shape is connected to the NP size and shape. The chemical environment surrounding

the AuNPs also affects the SPR position, which is known as chemical interface damping. The chemical interface damping induces a widening and a redshift of the SPR peak when the AuNPs are coated. This effect holds for both chemisorption and physisorption because the adsorbates provide new relaxation pathways for the excited electrons in the metal.[51]

1.2.2 Medical applications

Many studies have been devoted to the application of nanoparticles to medical applications and among them, a large part was focussed on AuNPs. AuNPs have been studied as drug carriers (drug delivery vehicles), energy transducers, PS efficiency enhancers, and as PS themselves.[45,54–56]

1.2.2.1 Toxicity

Gold is known to have low toxicity in humans and to be biocompatible. Such properties made gold a practical metal to be used for therapeutic applications and suitable for *in vivo* applications.[5,55,57] As with any other metal, the toxicity associated with gold depends on its oxidation state when administered to the patient. Metallic gold, gold (0), is an inert metal which is widely used in medicine as prosthesis, especially in the mouth.[58]

However, the toxicity of AuNPs is still questionable at this point. AuNPs have been described as nontoxic [59,60] or toxic.[60,61] Pernodet *et al.* showed that the uptake of citrate AuNPs (diameter 13 ± 1 nm) to human dermal fibroblast cells induced a significant adverse effect on cell viability.[61] In contrast, Connor *et al.* reported that Cysteine- and citrate-capped AuNPs (4 nm), glucose-reduced AuNPs (12 nm) and citrate, biotin and CTAB (cetyltrimethylammonium bromide) capped AuNPs (18 nm) were all endocytosed without signs of cytotoxicity.[59] Furthermore, Goodman *et al.* demonstrated that cationic AuNPs are moderately toxic, but anionic AuNPs were nontoxic.[60]

In another study, Pan *et al.* investigated the cytotoxicity of AuNPs depending on the size and concluded that the toxicity depends primarily on the size and not on the

ligand chemistry. The authors reported that AuNPs of 2 nm diameter were highly toxic and, on the other hand, smaller gold salts like Tauredon® or AuNPs larger than 15 nm were comparatively non-toxic.[62]

To sum it up, although AuNPs hold great promises for future medical applications, the scientific community still needs more information about the pharmacokinetics and biodistribution of AuNPs in the human body to accept them as non-toxic. So, according to the regulatory authorities, the effects of AuNPs in the human body are still unclear[63] and, as such, there are no official regulatory safety documents on AuNPs toxicity.

1.2.2.2 Size and shape effects

It is crucial to consider the size of the AuNPs when designing a new medical drug because it determines how the AuNPs are going to be distributed in the human body.[64,65] According to the literature, small NPs (up to 10 nm diameter) do not accumulate efficiently in tumour sites because they can be rapidly distributed to various organ systems, such as blood, liver, spleen, lung, heart, and brain.[66] On the other hand, AuNPs larger than 100 nm become recognised as external entities by the reticuloendothelial system and are quickly transported to the liver and spleen.[67,68] The size of spherical AuNPs is also important when taking into consideration the medical application. Spherical AuNPs of small sizes are more suitable for absorption-dependent photo processes, such as PDT and photothermal therapy (PTT).[69] On the other hand, bigger particles have a higher scattering cross-section and, therefore, are more suitable for imaging and diagnosis applications.[70]

Also, the variety of shapes in which AuNPs can be synthesised grant them excellent therapeutic flexibility because each shape has its unique SPR wavelength (depending on the size as well). AuNPs can be synthesised as nanospheres[71], nanotriangles[72], nanorods[72], nanostars[72], nanoshells[64] and nanocubes[72]. Nowadays, in the USA, gold nanoshells (trade name AuroShell®) are under clinical trials in the treatment of head and neck, and lung cancer as PTT agents.[73]

In this project, we will focus mainly on spherical AuNPs. An extensive review of the synthesis, optical properties, and applications of the other AuNPs shapes has been published recently by Huang *et al.*[73] and Ogarev *et al.*.[74]

1.2.2.3 Functionalization

AuNPs have also attracted interest because their surface can be readily functionalized, either non-covalently due to electrostatic interactions[60,75] or covalently via thiol or amino groups.[76–80] By designing such functionalization with specific ligands, it is possible to design AuNPs to use them as drug delivery vehicles, have an increased selectivity towards particular types of cells and improve their uptake, and/or extend their circulation times in the human body.[54,81,82]

A non-covalently bound drug can be delivered to a targeted location without losing its chemical and physical properties and thus retaining its therapeutic attributes. However, the non-covalent interaction is significantly more sensitive to the cell environment; hence, there is a high probability of AuNPs-drug equilibrium disruption.[83]

AuNPs with covalently bound ligands are considerably more stable when dispersed in a biological environment, i.e. the bloodstream. Also, by functionalizing AuNPs with a specific ligand, it is possible to increase both the uptake and the selectivity towards particular types of cells.[84,85] In recent research, it has been shown that it is possible to decorate the surface of AuNPs to avoid neutralisation by the immune system and increase the selectivity of the drug towards certain types of cells.[86,87] One of the most common ligands used for surface functionalization of AuNPs is polyethylene glycol (PEG), which is approved for human i.v. application.[88] It has been shown that a PEG layer increases the resistance to protein adsorption[89] and increases the circulation time of AuNPs@PEG in the bloodstream.[54,90] The current trends and applications of AuNPs coated with different polymers for cancer therapy have been reviewed recently by Muddineti *et al.*.[91] In addition to polymers, AuNPs have also been functionalized with biological molecules[92], such as proteins[83] or antibodies[57].

Lastly, it has been shown that AuNPs can be functionalized with two or more functional ligands, which further improve their range of applications, e.g. improving their drug delivery ability and, at the same time, improving the specificity to a specific type of cells.[91]

1.2.2.4 PDT enhancement and PS delivery

In addition to the passive surface functionalization described in the previous subsection, AuNPs can also be designed to enhance the PDT drug efficiency to generate ROS. When plasmonic AuNPs are functionalized with PSs and exposed to an external optical field, plasmonic coupling causes electric field enhancement near the surface of the AuNPs, which enhances the photon absorption by the PSs, hence increasing their efficiency.

Among the AuNPs@PSs nanocomposites being developed nowadays, AuNPs-phthalocyanines are the most researched.[54] These compounds have a high extinction coefficient for far-red light (~670 nm) and long-lived triplet excited states, which increases the ROS generation.[93] Moeno *et al.* demonstrated that a monolayer of Zn-phthalocyanine on the surface of AuNPs enhanced the $^1O_2$ production when compared with the free PS.[94] Also, Wieder *et al.* not only showed that Zn-phthalocyanine bound to 2-4 nm AuNPs increases the $^1O_2$ generation quantum yield by 44% when compared with the free PS, but also showed that phthalocyanine in a nanocomposite form is 2.4 times more selectively accumulated in the tumour after 24 hours upon intravenous injection than the free PS.[95]

AuNPs have also been decorated simultaneously with specific peptide sequences to improve the transport and targeting of tumours and PSs. Cheng. *et al.* designed a peptide sequence and coated it on 5 nm AuNPs to try to target glioblastoma multiform, an aggressive form of brain cancer.[96] The co-nanocomposite was constituted of the AuNPs, a 12 amino acid epidermal growth peptide and a PS (Pc 4). The authors suggest that the dominant pathway for the drug uptake by the brain tumour cells was the receptor-mediated endocytosis induced by the 12 amino acid peptide sequence.

Overall, the surface modification of AuNPs described above represents only a small fraction of all ligands that have been functionalized on AuNPs surfaces. Jain *et al.*,[45] Joanna *et al.*,[97] and more recently Krzysztof *et al.*,[98] have reviewed the uses of AuNPs for cancer therapy and provide a broader overview of the capping layers tested.

1.2.3 Gold nanoparticles as PDT photosensitisers

The medical uses of spherical AuNPs presented in the literature are mostly motivated both by their passive transport, heat generation and plasmonic enhancement functions. However, recently it has been shown that AuNPs photogenerate $^1O_2$ in solution when irradiated with pulsed and continuous wave (CW) laser light, and thus AuNPs should be useful as PDT PSs.[36,71,99]

In fact, Krpetic *et al.*[100] have shown that cancer cells (HeLa cells) uptake AuNPs@Citrate into endosomes, which upon low-intensity laser irradiation generate ROS, causing the endosomes to rupture and allowing the AuNPs to diffuse to the cytosol, without triggering cell death; however, at slightly higher irradiation powers, cell death was observed. More recently, Chadwick[101] explored the photothermal and photodynamic effect of laser irradiation using AuNPs and confirmed that it is possible to kill HeLa cells photodynamically, and further suggested that the ROS species being generated was $^1O_2$.

Unlike conventional PSs, AuNPs are photostable and biological inert, i.e. are resistant to enzymatic degradation, have strong optical properties due to the localised SPR and have good passive transport and plasmonic enhancement functions.[45,46,102,103] Other advantageous qualities include the ease in control over particle size and shape during synthesis which allows the plasmon resonance peaks of gold nanostructures (gold nanorods and gold nanostars) to be tuned to higher wavelengths when compared to conventional PSs, to get into the biological window (between 620 to 1300 nm), where tissue has light penetration of a few centimetres.[104] Finally, AuNPs are easily functionalized, which improves the AuNPs' versatility and allow for selective targetting.[74,105]

1.2.3.1 Singlet oxygen photogeneration

The first indication that AuNPs could undergo a photoinduced reaction with O_2 was revealed by Sakamoto *et al.* in 2009.[106] The authors showed that Au nanoclusters (~ 1 nm) in the absence of O_2 exhibited luminescence emission at 490 nm when excited

at 409 nm. In contrast, when exposed to O_2, the luminescence decreased significantly. Despite the observations, the authors did not correlate the decrease of the fluorescence to a possible ROS generation.

It was only in 2011 that Vankayala *et al.* showed the production of $^1O_2$ upon irradiation at the SPR of 22 nm AuNPs in D_2O.[25] To support their claims, Vankayala *et al.* showed a phosphorescence spectrum with a characteristic $^1O_2$ emission peak at 1268 nm. The peak shown in the phosphorescence spectrum was suggested as evidence that AuNPs can also generate $^1O_2$ in the absence of other PSs. This conclusion was also supported by H^1 NMR experiments, i.e. analysis of the photoinduced peroxidation of cyclohexene in the presence of AuNPs upon CW-irradiation. The authors further suggest that the $^1O_2$ generation quantum yield (QY) was 0.037 under their CW-irradiation conditions, determined by comparing the phosphorescence emission area of $^1O_2$ from 1225 to 1300 nm obtained from the irradiation of AuNPs and Rose Bengal (RB), a well-characterised PS dye, independently.[25] Later, in 2013, an independent study by Pasparakis further confirmed that AuNPs by themselves generate $^1O_2$ in the absence of a classical PS. In his research, Pasparakis also showed the characteristic $^1O_2$ phosphorescence peak at 1270 nm upon irradiation of AuNPs in D_2O and the respective control experiment in the absence of AuNPs (no peak present). Pasparakis also irradiated the AuNPs in the presence of DPBF and, indirectly, observed the generation of $^1O_2$. Similarly to Vankayala *et al.*, Pasparakis also reports a $^1O_2$ generation QY of 0.03 upon CW-irradiation at 532 nm, determined from a p-nitrosodimethylaniline (RNO) – histidine colourimetric assay.[99]

In another study, Chadwick *et al.* also showed that AuNPs could generate $^1O_2$.[71] In this study, DPBF was used to evaluate the $^1O_2$ photogeneration upon irradiation of AuNPs with CW and pulsed laser irradiation. Chadwick *et al.*, in contrast to what Vankayala *et al.* and Pasparakis reported, claimed a $^1O_2$ generation QY several orders of magnitude smaller (~10^{-6} and ~10^{-4} for CW and pulsed irradiation, respectively).[71] The authors went a step further and suggested a mechanism for the $^1O_2$ photogeneration by AuNPs.

Despite the QY controversy, the studies mentioned above showed that $^1O_2$ is generated upon irradiation of AuNPs, but the efficiency of the process is not clear. Nonetheless, the application of AuNPs in the field of PDT is a promising avenue for optimisation. However, to steer its development in replacing PSs in clinical practice, it is

crucial to quantify the $^1O_2$ QY of AuNPs upon irradiation accurately and solve the discrepancy between these very different previous results.

1.2.3.2 Mechanism

In contrast to organic dye molecules, metal NPs such as AuNPs do not have discrete electronic energy states, as shown in the Jablonski diagram (Figure 1.1). Instead, AuNPs have an extended band of states resulting from the overlap of atomic orbitals of the gold atoms that constitute the AuNP. Upon irradiation of a colloidal solution of AuNPs, the free electrons of AuNPs are excited by light and, if an oxygen molecule is nearby, the ground state oxygen can be excited to its singlet state. This process is thought to involve three phases, the interaction of light with the AuNP, relaxation processes within the AuNP, and Dexter type exchange energy transfer in collision complexes between the AuNP and molecular oxygen.[71,99]

The relaxation processes of AuNPs under laser irradiation have been described in great detail,[51,107] and were observed using femtosecond transient absorption spectroscopy. The sequence of events and approximate times scales that follow the absorption of a photon by a AuNP are shown in Figure 1.8.[51]

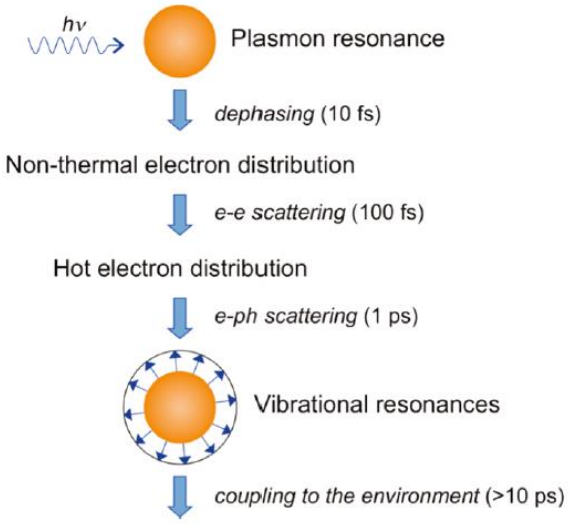

Figure 1.8 - Sequence of events and approximate times scales that follow the absorption of a photon by a AuNP. Image taken from [51].

At low temperatures, i.e. before laser irradiation, most of the states below the Fermi level are occupied, and most states above are vacant. Upon exposure to laser irradiation, the electromagnetic field of the light induces a dipolar oscillation of the electrons - the SPR, which rapidly dephases (~ 10 fs). The electron distribution can absorb a photon, exciting electrons from the electron gas, leading to an excited electron distribution across different levels in the conduction band, also known as non-thermal electron distribution. These excited electrons quickly equilibrate via electron-electron scattering to yield a Fermi distribution, and these new equilibrated electron distributions are called "hot electrons". This process occurs on a time scale of a few 100 fs. The energy excess of the hot electrons can then be dumped by electron-phonon scattering (~ 1 ps). The electron-phonon interaction leads to a temperature increase of the lattice, hence causing increased lattice vibrations. Finally, the excess energy from the vibrations of the lattice decay by heat energy transfer to the solvent on the 10 ps time scale. This results in cooling of the lattice and the electron gas, and the system returns to its initial electron temperature before laser excitation.

Chadwick *et al.* suggested that the generation of $^1O_2$ upon CW irradiation occurs during the initially created "primary hot electrons" following the Dexter electron exchange coupling mechanism of these "primary hot electrons" with O_2[71]; i.e. it occurs during the short time period which the excited electrons have not yet relaxed to a thermal distribution. This is because during CW irradiation the excitation rate is so low that essentially only the energy of at most one photon is present at any time, so that the "hot" electrons do not have sufficient energy for the formation of $^1O_2$. In the case of AuNPs, an electron from the $2\pi^*$ orbitals of oxygen will simultaneously transfer to a photogenerated hole on the AuNP while, simultaneously, one high energy excited electron with the opposite spin transfers from the AuNP, to fill the other $2\pi^*$ orbital on oxygen, generating the singlet state.

Due to the short lifetime of hot electrons (~ 1 ps) and the even shorter lifetime of the primary excited electrons (~100 fs) and the short distance requirement for the Dexter mechanism to occur, it is reasonable to suggest that this process must have an extremely low QY, closer to that reported by Chadwick *et al.*, rather than those values reported by Vankayala *et al*. and Pasparakis. A more detailed analysis and a comparison of these reports will be given in the discussion of the results presented in this thesis (Chapter 3).

1.3 Scope of the study

As outlined above, significant progress is being made to use AuNPs as a PS for PDT to overcome some of the issues associated with the use of conventional PSs (see section 1.2.3). In light of this, this thesis presents a thorough study to determine how efficiently AuNPs can photogenerate $^1O_2$ when excited at their SPR. In continuation of work carried out by our research group, the $^1O_2$ photogeneration of AuNPs has been investigated in greater detail.

A series of irradiation experiments have been performed in the presence of ABDA and DPBF using Rose Bengal (RB) as a (well-characterized) $^1O_2$ PS to quantitatively determine the sensitivity* of these molecular probes towards $^1O_2$; Chapter 2. Taking into consideration the sensitivity of the molecular probes, CW-irradiation of AuNPs in the presence of both molecular probes was performed to prove conclusively that AuNPs upon irradiation generate $^1O_2$, and the efficiency of the process (QY) determined; Chapter 3. To foresee a future medical application, i.e. investigate the effect of a protein corona on the $^1O_2$ QY, AuNPs were functionalized with bovine serum albumin (BSA), irradiated and their $^1O_2$ generation efficiency evaluated; Chapter 4.

The main aim of this thesis is to conduct a thorough study of the $^1O_2$ photogeneration efficiency of AuNPs upon CW-irradiation (532 nm) at their SPR and show that the functionalization of AuNPs with proteins does not impairs the $^1O_2$ photogeneration.

* Probability of the reaction of $^1O_2$ with the sensor leading to sensor bleach.

1.4 References

(1) https://www.who.int/news-room/fact-sheets/detail/the-top-10-causes-of-death (accessed Mar 18, 2019).

(2) Wild, C. P.; Stewart, B. W.; World Cancer Report 2014. **2014**, 630.

(3) American Cancer Society. Cancer Treatment & Survivorship Facts & Figures 2016-2017. *Am. Cancer Soc.* **2016**, 44.

(4) Broekgaarden, M.; Weijer, R.; van Gulik, T. M.; Hamblin, M. R.; Heger, M.; Gulik, T. M. Van. Tumor Cell Survival Pathways Activated by Photodynamic Therapy: A Molecular Basis for Pharmacological Inhibition Strategies. *Cancer Metastasis Rev.* **2015**, *34*, 643.

(5) Agostinis, P.; Berg, K.; Cengel, K. A.; Foster, T.; Girotti, A. W.; Gollnick, S. O.; Hahn, S. M.; Hamblin, M.R.; Juzeniene, A.; Kessel, D.; Koberlik, M.; Moan, J.; Mroz, P.; Nowis, D.; Piette, J.; Wilson, B.; Golab, J. Photodynamic Terapy of Cancer: An Update. *CA Cancer J Clin.* **2011**, *61*, 250.

(6) Gold, M. *Photodynamic Therapy in Dermatology*; Springer New York: New York, 2011.

(7) O'Connor, A. E.; Gallagher, W. M.; Byrne, A. T. Porphyrin and Nonporphyrin Photosensitizers in Oncology: Preclinical and Clinical Advances in Photodynamic Therapy. *Photochem. Photobiol.* **2009**, *85*, 1053.

(8) Brown, S. B.; Brown, E. A.; Walker, I. The Present and Future Role of Photodynamic Therapy in Cancer Treatment. *Lancet Oncol.* **2004**, *5*, 497.

(9) Mehraban, N.; Freeman, H. S. Developments in PDT Sensitizers for Increased Selectivity and Singlet Oxygen Production; *Materials (Basel)*, **2015**, 8, 4421.

(10) Calin, M. ; Parasca, S. V.; Triesscheijn, M.; Baas, P.; Schellens, J. H.; Stewart, F. A. Photodynamic Therapy in Oncology. *Oncologist* **2006**, *11*, 1034.

(11) Grant, W. E.; Speight, P. M.; Hopper, C.; Bown, S. G. Photodynamic Therapy: An Effective, but Non-Selective Treatment for Superficial Cancers of the Oral Cavity. *Int. J. Cancer* **1997**, *71*, 937.

(12) Rhodes, L. E.;Rie, M.; Enström, Y.; Groves, R.; Morken, T.; Goulden, V.; Wong, G.; Grob, J.; Varma, S.; Wolf, P. Photodynamic Therapy Using Topical Methyl Aminolevulinate vs Surgery for Nodular Basal Cell Carcinoma. *Arch. Dermatol.* **2004**, *140*, 17.

(13) Zhang, J.; Jiang, C.; Longo, J. P.; Azevedo, R. B.; Zhang, H.; Muehlmann, L. A. An Updated Overview on the Development of New Photosensitizers for Anticancer Photodynamic Therapy. *Acta Pharm. Sin. B* **2018**, *8*, 137.

(14) Ormond, A. B.; Freeman, H. S. Dye Sensitizers for Photodynamic Therapy, *Materials (Basel).* **2013**, *6*, 817.

(15) Wright, K. E.; Liniker, E.; Loizidou, M.; Moore, C.; Macrobert, A. J.; Phillips, J. B. Peripheral Neural Cell Sensitivity to mTHPC-Mediated Photodynamic Therapy in a 3D in Vitro Model., *J. Cancer* **2009**, *101*, 658.

(16) Calixto, G. M. F.; Bernegossi, J.; De Freitas, L. M.; Fontana, C. R.; Chorilli, M.; Grumezescu, A. M. Nanotechnology-Based Drug Delivery Systems for Photodynamic Therapy of Cancer: A Review. *Molecules* **2016**, *21, 342*.

(17) Skourtis, S. S.; Liu, C.; Antoniou, P.; Virshup, A. M.; Beratan, D. N. Dexter Energy Transfer Pathways. *Proc. Natl. Acad. Sci.* **2016**, *113*, 8115.

(18) Murphy, C. B.; Zhang, Y.; Troxler, T.; Ferry, V.; Martin, J. J.; Jones, W. E. Probing Förster and Dexter Energy-Transfer Mechanisms in Fluorescent Conjugated Polymer Chemosensors. *J. Phys. Chem. B* **2004**, *108*, 1537.

(19) https://chem.libretexts.org/Bookshelves/Physical_and_Theoretical_Chemistry_Textbook_Maps/Supplemental_Modules_(Physical_and_Theoretical_Chemistry)/Fundamentals/Dexter_Energy_Transfer (accessed Jul 22, 2019).

(20) Castano, A. P.; Demidova, T. N.; Hamblin, M. R. Mechanisms in Photodynamic Therapy: Part One—Photosensitizers, Photochemistry and Cellular Localization. *Photodiagnosis Photodyn. Ther.* **2004**, *1*, 279.

(21) Krukiewicz, K., The Phenomenon of Singlet Oxygen, *Chemik*, **2011**, *65*, 1190.

(22) Dai, T.; Huang, Y.; Hamblin, M. R. Photodynamic Therapy for Localized Infections—State of the Art. *Photodiagnosis Photodyn. Ther.* **2009**, *6*, 170.

(23) Clennan, E. L.; Pace, A. Advances in Singlet Oxygen Chemistry. *Tetrahedron* **2005**, *61*, 6665.

(24) Housecroft, C. E.; Sharpe, A. G. *Inorganic Chemistry*; Pearson Prentice Hall, 4th Edition, **2005**.

(25) Vankayala, R.; Sagadevan, A.; Vijayaraghavan, P.; Kuo, C. L.; Hwang, K. C. Metal Nanoparticles Sensitize the Formation of Singlet Oxygen. *Angew. Chemie - Int. Ed.* **2011**, *50*, 10640.

(26) Alexander, K. J.; Christopher, F. Time-Resolved Measurements of Singlet Oxygen Dimol-Sensitized Luminescence. *J. Am. Chem. Soc.* **1993**, *115*, 6013.

(27) Antosiewicz, J.; Wozniak, M.; Tanfani, F.; Bertoli, E.; Zolese, G.; Antosiewicz, J. A New Fluorescence Method to Detect Singlet Oxygen inside Phospholipid Model Membranes. *Biochim. Biophys. Acta (BBA)/Lipids Lipid Metab.* **1991**, *1082*, 94.

(28) Carloni, P.; Damiani, E.; Greci, L.; Stipa, P.; Tanfani, F.; Tartaglini, E.; Wozniak, M. On the Use of 1,3-Diphenylisobenzofuran (DPBF). Reactions with Carbon and Oxygen Centered Radicals in Model and Natural Systems. *Res. Chem. Intermed.* **1993**, *19*, 395.

(29) Wang, G.; Wang, B.; Park, J.; Yang, J.; Shen, X.; Yao, J. Synthesis of Enhanced Hydrophilic and Hydrophobic Graphene Oxide Nanosheets by a Solvothermal Method. *Carbon N. Y.* **2009**, *47*, 68.

(30) Umezawa, N.; Tanaka, K.; Urano, Y.; Kikuchi, K.; Higuchi, T.; Nagano, T.; Cryst, M.; Cryst, L.; Kaupp, G.; Novel Fluorescent Probes for Singlet Oxygen. *Angew. Chemie-Int. Ed.* **1999**, *38*, 2899.

(31) Wilson, T. Excited Singlet Molecular Oxygen in Photooxidation. *J. Am. Chem. Soc.* **1966**, *88*, 2898.

(32) Stevens, B.; Perez, S. R. The Photoperoxidation of Unsaturated Organic Molecules. *J. Photochem.* **2002**, *1*, 283.

(33) Yuan, Y.; Zhang, C.J.; Xu, S.; Liu, B. A Self-Reporting AIE Probe with a Built-in Singlet Oxygen Sensor for Targeted Photodynamic Ablation of Cancer Cells. *Chem. Sci.* **2016**, *7*, 1862.

(34) Chauhan, P.; Hadad, C.; Sartorelli, A.; Zarattini, M.; Herreros-López, A.; Mba, M.; Maggini, M.; Prato, M.; Carofiglio, T. Nanocrystalline Cellulose–porphyrin Hybrids: Synthesis, Supramolecular Properties, and Singlet-Oxygen Production. *Chem. Commun.* **2013**, *49*, 8525.

(35) Vankayala, R.; Lin, C.; Kalluru, P.; Chiang, C.; Hwang, K. Gold Nanoshells-Mediated Bimodal Photodynamic and Photothermal Cancer Treatment Using Ultra-Low Doses of near Infra-Red Light. *Biomaterials* **2014**, *35*, 5527.

(36) Vankayala, R.; Huang, Y.; Kalluru, P.; Chiang, C.; Hwang, K. First Demonstration of Gold Nanorods-Mediated Photodynamic Therapeutic Destruction of Tumors via Near Infra-Red Light Activation. *Small* **2014**, *10*, 1612.

(37) Lin, H.; Shen, Y.; Chen, D.; Lin, L.; Wilson, B.; Li, B.; Xie, S. Feasibility Study on Quantitative Measurements of Singlet Oxygen Generation Using Singlet Oxygen Sensor Green. *J. Fluoresc.* **2013**, *23*, 41.

(38) Gollnick, K.; Miinchen, D.; Singlet Oxygen Photooxygenation of Furans. *Tetrahedron* **1985**, *41*, 2057.

(39) Aubry, J.; Mandard-Cazin, B.; Rougee, M.; Bensasson, R. Kinetic Studies of Singlet Oxygen [4+2]-Cycloadditions with Cyclic 1,3-Dienes in 28 Solvents. *J. Am. Chem. Soc.* **1995**, *117*, 9159.

(40) Wu, H.; Song, Q.; Ran, G.; Lu, X.; Xu, B. Recent Developments in the Detection of Singlet Oxygen with Molecular Spectroscopic Methods. *TrAC Trends Anal. Chem.* **2011**, *30*, 133.

(41) Arian, D.; Kovbasyuk, L.; Mokhir, A. 1,9-Di(Alkoxy)Anthracene as a $^1O_2$-Sensitive Linker. *J. Am. Chem. Soc.* **2011**, 133, 3972.

(42) Lindig, B. A.; Rodgers, M.; Schaaplc, A. P.; Schaap, A. P. Determination of the Lifetime of Singlet Oxygen in Water-D_2 Using 9,10-Anthracenedipropionic Acid, a Water-Soluble Probe. *J. Am. Chem. Soc.* **1980**, *102*, 5590.

(43) Kim, S.; Fujitsuka, M.; Majima, T. Photochemistry of Singlet Oxygen Sensor Green. *J. Phys. Chem. B* **2013**, 117, 13985.

(44) You, Y. Chemical Tools for the Generation and Detection of Singlet Oxygen. *Org. Biomol. Chem.* **2018**, *16*, 4044.

(45) Jain, S.; Hirst, D. G.; O'Sullivan, J. M. Gold Nanoparticles as Novel Agents for Cancer Therapy. *Br. J. Radiol.* **2012**, *85*, 101.

(46) Yao, C.; Zhang, L.; Wang, J.; He, Y.; Xin, J.; Wang, S.; Xu, H.; Zhang, Z. Gold Nanoparticle Mediated Phototherapy for Cancer, *J. Nanomat*, **2016**, *2016, 1*.

(47) Pricker, S. P. Medical Uses of Gold Compounds: Past, Present and Future. *Gold Bull.* **1996**, *29*, 53.

(48) Turkevich, J.; Stevenson, P. C.; Hillier, J. A Study of the Nucleation and Growth Processes in the Synthesis of Colloidal Gold. *Discuss. Faraday Soc.* **1951**, *11*, 55.

(49) Frens, G. Controlled Nucleation for the Regulation of the Particle Size in Monodisperse Gold Suspensions. *Nat. Phys. Sci.* **1973**, *241*, 20.

(50) Shi, L.; Buhler, E.; Boué, F.; Carn, F. How Does the Size of Gold Nanoparticles Depend on Citrate to Gold Ratio in Turkevich Synthesis? Final Answer to a Debated Question. *J. Colloid Interface Sci.* **2017**, *492*, 191.

(51) Hartland, G. V. Optical Studies of Dynamics in Noble Metal Nanostructures. *Chem. Rev.* **2011**, *111*, 3858.

(52) http://www.cytodiagnostics.com/store/pc/Gold-Nanoparticle-Properties-d2.htm (accessed Mar 18, 2019).

(53) https://nanocomposix.com/pages/gold-nanoparticles-optical-properties (accessed Mar 18, 2019).

(54) Lucky, S. S.; Soo, K. C.; Zhang, Y. Nanoparticles in Photodynamic Therapy. *Chem. Rev.* **2015**, *115*, 1990.

(55) Thakor, S.; Jokerst, J.; Zavaleta, C.; Massoud, T. F.; Gambhir, S. S. Gold Nanoparticles: A Revival in Precious Metal Administration to Patients. *Nano Lett.* **2011**, *11*, 4029.

(56) Trouiller, A. J.; Hebie, S.;Bahhaj, F.; Napporn, T. W.; Bertrand, P. Chemistry for Oncotheranostic Gold Nanoparticles. *Eur. J. Med. Chem.* **2015**, *99*, 92.

(57) Jazayeri, M. H.; Amani, H.; Pourfatollah, A. A.; Pazoki-Toroudi, H.; Sedighimoghaddam, B. Various Methods of Gold Nanoparticles (GNPs) Conjugation to Antibodies. *Sens. Bio-Sensing Res.* **2016**, *9*, 17.

(58) Merchant, B. Gold, the Noble Metal and the Paradoxes of Its Toxicology. *Biologicals* **1998**, *26*, 49.

(59) Connor, E. E.; Mwamuka, J.; Gole, A.; Murphy, C. J.; Wyatt, M. D. Gold Nanoparticles are taken up by Human cells but do not cause acute cytotoxicity. *Small* **2005**, *1*, 325.

(60) Goodman, C. M.; McCusker, C. D.; Yilmaz, T.; Rotello, V. M. Toxicity of Gold Nanoparticles Functionalized with Cationic and Anionic Side Chains. *Bioconjug. Chem.* **2004**, *15*, 897.

(61) Pernodet, N.; Fang, X.; Sun, Y.; Bakhtina, A.; Ramakrishnan, A.; Sokolov, J.; Ulman, A.; Rafailovich, M. Adverse Effects of Citrate/Gold Nanoparticles on Human Dermal Fibroblasts. *Small* **2006**, *2*, 766.

(62) Pan, Y.; Bartneck, M.; Jahnen-Dechent, W. Cytotoxicity of Gold Nanoparticles *Methods Enzymol.*, **2012**, 509, 42.

(63) Yah, C. S. The Toxicity of Gold Nanoparticles in Relation to Their Physiochemical Properties. *Biomed. Res.* **2013**, *24*, 400.

(64) Khlebtsov, N.; Dykman, L. Biodistribution and Toxicity of Engineered Gold Nanoparticles: A Review of in Vitro and in Vivo Studies. *Chem. Soc. Rev.* **2011**, *40*,

1647.

(65) Sonavane, G.; Tomoda, K.; Makino, K. Biodistribution of Colloidal Gold Nanoparticles after Intravenous Administration: Effect of Particle Size. *Colloids Surfaces B Biointerfaces* **2008**, *66*, 274.

(66) De Jong, W. H.; Hagens, W. I.; Krystek, P.; Burger, M. C.; Sips, A. J.; Geertsma, R. E. Particle Size-Dependent Organ Distribution of Gold Nanoparticles after Intravenous Administration. *Biomaterials* **2008**, *29*, 1912.

(67) Trono, J. D.; Mizuno, K.; Yusa, N.; Matsukawa, T.; Yokoyama, K.; Uesaka, M. Size, Concentration and Incubation Time Dependence of Gold Nanoparticle Uptake into Pancreas Cancer Cells and Its Future Application to X-Ray Drug Delivery System. *J. Radiat. Res.* **2011**, *52*, 103.

(68) Jiang, W.; Kim, B. Y. S.; Rutka, J. T.; Chan, W. C. W. Nanoparticle-Mediated Cellular Response Is Size-Dependent. *Nat. Nanotechnol.* **2008**, *3*, 145.

(69) Arvizo, R. R.; Bhattacharyya, S.; Kudgus, R. A.; Giri, K.; Bhattacharya, R.; Mukherjee, P. Intrinsic Therapeutic Applications of Noble Metal Nanoparticles: Past, Present and Future. *Chem. Soc. Rev.* **2012**, *41*, 2943.

(70) Huang, X.; El-Sayed, M. A. Gold Nanoparticles: Optical Properties and Implementations in Cancer Diagnosis and Photothermal Therapy. *J. Adv. Res.* **2010**, *1*, 13.

(71) Chadwick, S. J.; Salah, D.; Livesey, P. M.; Brust, M.; Volk, M. Singlet Oxygen Generation by Laser Irradiation of Gold Nanoparticles. *J. Phys. Chem. C* **2016**, *120*, 10647.

(72) Xie, X.; Liao, J.; Shao, X.; Li, Q.; Lin, Y. The Effect of Shape on Cellular Uptake of Gold Nanoparticles in the Forms of Stars, Rods, and Triangles. *Sci. Rep.* **2017**, *7*, 1.

(73) https://clinicaltrials.gov/ct2/show/NCT00848042 (accessed Feb 12, 2019).

(74) Ogarev, V. A.; Rudoi, V. M.; Dement'eva, O. V. Gold Nanoparticles: Synthesis, Optical Properties, and Application. *Inorg. Mater. Appl. Res.* **2018**, *9*, 134.

(75) Chen, S.; Lei, Q.; Qiu, W. X.; Liu, L. H.; Zheng, D. W.; Fan, J. X.; Rong, L.; Sun, Y. X.; Zhang, X. Z. Mitochondria-Targeting "Nanoheater" for Enhanced Photothermal/Chemo-Therapy. *Biomaterials* **2017**, *117*, 92.

(76) Porcaro, F.; Battocchio, C.; Antoccia, A.; Fratoddi, I.; Venditti, I.; Fracassi, A. Synthesis of Functionalized Gold Nanoparticles Capped with 3-Mercapto-1-Propansulfonate and 1-Thioglucose Mixed Thiols and " in Vitro " Bioresponse. *Colloids Surfaces B Biointerfaces* **2016**, *142*, 408.

(77) Krpetic, Z.; Davidson, A. M.; Volk, M.; Levy, R.; Brust, M.; Cooper, D. L. High Resolution Sizing of Monolayer Protected Gold Clusters by Differential Centrifugal Sedimentation. *ACS Nano* **2013**, 7, 8881.

(78) Selvakannan P.; Mandal S.; Sumant P.; Renu P.; Sastry, M. Capping of Gold Nanoparticles by the Amino Acid Lysine Renders Them Water-Dispersible. *Langmuir* **2003**, *19*, 3545.

(79) Zarabi, M. F.; Arshadi, N.; Farhangi, A.; Akbarzadeh, A. Preparation and

Characterization of Gold Nanoparticles with Amino Acids, Examination of Their Stability. *Indian J. Clin. Biochem.* **2014**, *29*, 306.

(80) Hussain, I.; Nichols, R. J.; Schiffrin, D. J.; Brust, M.; Fernig, D. G.; Lévy, R.; Thanh, N. T. K. K.; Christopher Doty, R.; Hussain, I.; Rational and Combinatorial Design of Peptide Capping Ligands for Gold Nanoparticles. *J. Am. Chem. Soc.* **2004**, *126*, 10076.

(81) Quirk, B. J.; Brandal, G.; Donlon, S.; Vera, J. C.; Mang, T. S.; Foy, A. B.; Lew, S. M.; Girotti, A. W.; Jogal, S.; LaViolette, P. S.; Connelly, J. M.; Whelan, H. T. Photodynamic Therapy (PDT) for Malignant Brain Tumors - Where Do We Stand? *Photodiagnosis Photodyn. Ther.* **2015**, *12*, 530.

(82) Bacellar, I. O.; Tsubone, T. M.; Pavani, C.; Baptista, M. S. Photodynamic Efficiency: From Molecular Photochemistry to Cell Death. *Int. J. Mol. Sci.* **2015**, *16*, 20523.

(83) Wang, A.; Perera, Y. R.; Davidson, M. B.; Fitzkee, N. C. Electrostatic Interactions and Protein Competition Reveal a Dynamic Surface in Gold Nanoparticle-Protein Adsorption. *J. Phys. Chem. C. Nanomater. Interfaces* **2016**, *120*, 24231.

(84) Alea-Reyes, M. E.; Rodrigues, M.; Serrà, A.; Mora, M.; Sagristá, M. L.; González, A.; Durán, S.; Duch, M.; Plaza, J. A.; Vallés, E.; Russell, D. A.; Pérez-García, L. Nanostructured Materials for Photodynamic Therapy: Synthesis, Characterization and in Vitro Activity. *RSC Adv.* **2017**, *7*, 16963.

(85) Blanco, E.; Shen, H.; Ferrari, M. Principles of Nanoparticle Design for Overcoming Biological Barriers to Drug Delivery. *Nat. Biotechnol.* **2015**, *33*, 941.

(86) Byrne, J. D.; Betancourt, T.; Brannon-Peppas, L. Active Targeting Schemes for Nanoparticle Systems in Cancer Therapeutics. *Adv. Drug Deliv. Rev.* **2008**, *60*, 1615.

(87) Acharya, S.; Dilnawaz, F.; Sahoo, S. K. Targeted Epidermal Growth Factor Receptor Nanoparticle Bioconjugates for Breast Cancer Therapy. *Biomaterials* **2009**, *30*, 5737.

(88) Niidome, T.; Yamagata, M.; Okamoto, Y.; Akiyama, Y.; Takahashi, H.; Kawano, T.; Katayama, Y.; Niidome, Y. PEG-Modified Gold Nanorods with a Stealth Character for in Vivo Applications. *J. Control. Release* **2006**, *114*, 343.

(89) Davidson, A. M.; Brust, M.; Cooper, D. L.; Volk, M. Sensitive Analysis of Protein Adsorption to Colloidal Gold by Differential Centrifugal Sedimentation. *Anal. Chem.* **2017**, *89*, 6807.

(90) Gilles, M.; Brun, E.; Sicard-roselli, C. Gold Nanoparticles Functionalization Notably Decreases Radiosensitization through Hydroxyl Radical Production under Ionizing Radiation. *Colloids Surfaces B Biointerfaces* **2014**, *123*, 770.

(91) Muddineti, O. S.; Ghosh, B.; Biswas, S. Current Trends in Using Polymer Coated Gold Nanoparticles for Cancer Therapy. *Int. J. Pharm.* **2015**, *484*, 252.

(92) Oo, K. 5-aminolevulinic Acid-conjugated Gold Nanoparticles for Photodynamic Therapy of Cancer. *Nanomedicine* **2008**, *3*, 777.

(93) Kuznetsova, N. A.; Gretsova, N. S.; Derkacheva, V. M.; Oleg, L.; Lukyanets, E. A.;

Kaliya, O. L.; Lukyanets, E. A. Sulfonated Phthalocyanines: Aggregation and Singlet Oxygen Quantum Yield in Aqueous Solutions. *J. Porphyr. Phthalocyanines* **2003**, *7*, 147.

(94) Moeno, S.; Krause, R. W. M.; Ermilov, E. A.; Kuzyniak, W.; Höpfner, M. Synthesis and Characterization of Novel Zinc Phthalocyanines as Potential Photosensitizers for Photodynamic Therapy of Cancers. *Photochem. Photobiol. Sci.* **2014**, *13*, 963.

(95) Wieder, M. E.; Hone, D. C.; Cook, M. J.; Handsley, M. M.; Gavrilovic, J.; Russell, D. A. Intracellular Photodynamic Therapy with Photosensitizer-Nanoparticle Conjugates: Cancer Therapy Using a 'Trojan Horse.' *Photochem. Photobiol. Sci.* **2006**, *5*, 727.

(96) Zhao, T.; Yu, K.; Li, L.; Zhang, T.; Guan, Z.; Gao, N.; Yuan, P.; Li, S.; Yao, S. Q.; Xu, Q.-H.; Xu, G. Q. Gold Nanorod Enhanced Two-Photon Excitation Fluorescence of Photosensitizers for Two-Photon Imaging and Photodynamic Therapy. *ACS Appl. Mater. Interfaces* **2014**, *6*, 2700.

(97) Lim, Z.; Li, J.J.; Ng, C.; Yung, L. L.; Bay, B. Gold Nanoparticles in Cancer Therapy. *Acta Pharmacol. Sin.* **2011**, *32*, 983.

(98) Sztandera, K.; Gorzkiewicz, M.; Klajnert-Maculewicz, B. Gold Nanoparticles in Cancer Treatment. *Mol. Pharm.* **2019**, *16*, 1.

(99) Pasparakis, G. Light-Induced Generation of Singlet Oxygen by Naked Gold Nanoparticles and Its Implications to Cancer Cell Phototherapy. *Small* **2013**, *9*, 4130.

(100) Krpetić, Ž.; Nativo, P.; Sée, V.; Prior, I. A.; Brust, M.; Volk, M.; Inflicting Controlled Nonthermal Damage to Subcellular Structures by Laser-Activated Gold Nanoparticles. *Nano Lett.* **2010**, *10*, 4549.

(101) Chadwick, S. Photodynamic and Photothermal Human Cancer Cell Killing Using Gold Nanoparticles, PhD thesis, University of Liverpool, **2015**.

(102) Kong F.; Zhang J.; Li R.; Wang Z. Unique Roles of Gold Nanoparticles in Drug Delivery, Targeting and Imaging Applications. *Molecules* **2017**, *22*, 1445.

(103) Singh, P.; Pandit, S.; Mokkapati, V.; Garg, A.; Ravikumar, V.; Mijakovic, I. Gold Nanoparticles in Diagnostics and Therapeutics for Human Cancer, *Int. J. Mol. Sci.*, **2018,** 19, 1979.

(104) Peng, Q.; Juzeniene, A.; Chen, J.; Svaasand, L. O.; Warloe, T.; Giercksky, K.E.; Moan, J. Lasers in Medicine. *Reports Prog. Phys.* **2008**, *71*, 56701.

(105) Verma, H. N.; Singh, P.; Chavan, R. M. Gold Nanoparticle: Synthesis and Characterization. *Vet. World* **2014**, *7,72*.

(106) Sakamoto, M.; Tachikawa, T.; Fujitsuka, M.; Majima, T. Photoreactivity of As-Fabricated Au Clusters at the Single-Cluster Level. *J. Am. Chem. Soc.* **2009**, *131*, 6.

(107) Link, S.; El-Sayed, M. A. Shape and Size Dependence of Radiative, Non-Radiative and Photothermal Properties of Gold Nanocrystals. *Int. Rev. Phys. Chem.* **2000**, *19*, 409.

Chapter 2

2. Detection sensitivity of singlet oxygen sensors ABDA and DPBF

2.1 Introduction

It is widely accepted that $^1O_2$ is the primary cytotoxic agent responsible for the phototoxic activity in PDT.[1] However, due to its high reactivity, it is difficult to detect and quantify accurately. The only direct detection method relies on the detection of its weak photon emission at 1270 nm, directly emitted during the decay of $^1O_2$, which requires expensive specialised equipment.[2] In addition to the detection of $^1O_2$ luminescence, $^1O_2$ can also be monitored indirectly using molecular probes whose consumption can be monitored spectrophotometrically, which is considerably less expensive when compared to the direct detection methodology and more commonly available.[3]

Here, we will determine the sensitivity of two molecular probes, DPBF and ABDA, to $^1O_2$, i.e. the probability of the reaction of $^1O_2$ with the sensor leading to sensor bleach, in different solvents. In the presence of $^1O_2$ both sensors photobleach, as is expected due to their reaction with $^1O_2$, *i.e.* the cycloaddition reactions shown in Figure 1.5, which results in the loss of absorbance in the near UV or visible spectral region because of the less extended conjugated π-system of the endoperoxide products. The sensitivity determined in this chapter for both sensors in different solvents is important because it will allow the determination of the quantum efficiency of AuNPs for the formation of $^1O_2$ in the following chapters.

2.2 Experimental

2.2.1 Materials

ABDA, Rose Bengal (RB), sodium azide (NaN_3) and D_2O were purchased from Sigma-Aldrich and, DPBF, EtOH and DMSO were purchased from Fisher Scientific. All

chemicals were used as received. Milli-Q water (>18.2 MΩ cm) was prepared freshly before the experiment using a Barnstead Smart2Pure water purification system (Thermo Scientific).

Before use, all glassware, cuvettes and stirrer bars were cleaned in Aqua Regia (3:1 HCl:HNO_3) and thoroughly rinsed with Milli-Q water and set to dry. All handling of Aqua Regia was done with glassware inside a fume hood using the appropriate personal protective equipment, i.e. lab coat, safety glasses and gloves compatible with HNO_3 and HCl. A more detailed protocol for the cleaning of cuvettes and stirrer bars can be found in Appendix 1, section A1.1 and A1.2. All solutions were prepared and kept stirring until used. All the sample preparation involving the chemical traps were carried out in the dark.

2.2.2 Sample preparation

$^1O_2$ was photogenerated via irradiation of RB solutions with CW-laser light (532 nm) and detected via photobleaching of DPBF and ABDA solutions measured by UV-Vis spectroscopy.

Due to DPBF insolubility in neat water, all experiments with DPBF were conducted in 50/50 (v/v) EtOH/H_2O or EtOH/D_2O. To prepare the DPBF solutions, a DPBF stock solution (~ 0.1 mM) was initially prepared in EtOH, kept stirring in the dark and used within 24 hours. The DPBF ethanolic stock solution was then diluted 1:1 in a cuvette with either Milli-Q H_2O or D_2O and used immediately.

ABDA stock solution was prepared in DMSO (~ 10 mM) because it was found to be difficult to fully dissolve ABDA in neat water. To prepare the ABDA solutions, an aliquot of ABDA stock solution (1% of the total volume) was added to either Milli-Q H_2O, D_2O or 50/50 (v/v) EtOH/D_2O solution mixtures.

A stock solution of RB (~0.5 mM) was prepared in H_2O and kept stirring in the dark. A small aliquot was added to the ABDA or DPBF solutions to achieve the desired concentration of RB, which was always below 10^{-5} M.

For experiments in the presence of sodium azide, a small aliquot of a 2 M sodium azide stock solution in H_2O or D_2O was added to yield a final concentration of 20 mM in the irradiated solution.

For determining the extinction coefficients of DPBF and ABDA, a minimum of 10 mg of each compound was weighed accurately on a digital analytical balance (4 S.F.) to achieve sufficient accuracy.

2.2.3 Irradiation setup

For the irradiation experiments, the solutions were placed into a 10 mm path-length cuvette (Starna Special Optical Glass, SOG) equipped with a magnetic stirrer bar and sealed with an airtight stopper. The solution was kept stirring before and throughout the irradiation experiment.

The irradiation was performed at 532 nm using a continuous-wave diode-pumped solid-state laser (Opus 532, Laser quantum) with a beam diameter of 1.85 mm. The laser powers used for the irradiation of DPBF and ABDA solutions (200 mW[♣]) was reduced to 0.14 mW and 2.4 mW using calibrated neutral density filters. The laser power was further reduced by reflection losses of 4.6%[♣♣] on the front face of the cuvette. The rate of photon absorption during the irradiation, N_{abs}, was determined from the power incident on the sample itself and the sample absorbance at 532 nm, which results exclusively from RB, see Figure 2.1.

The samples were irradiated for regular intervals and the absorbance spectrum recorded using a Genesys 10 UV or Ocean Optics USB4000 spectrometer between each interval.

The solution stability was checked in the absence of irradiation to confirm the chemical stability of DPBF, ABDA and RB. The control experiments showed no spectra changes over a time interval of 30 minutes prior to the irradiation, see Appendix 2 – Figure A2. 1.

2.2.4 Results analysis

The progressive photobleach of ABDA and DPBF was quantified by averaging the absorbance around the maximum peak (see Figure 2.1) at 398 (between 398 – 400 nm)

♣ - The laser power was verified using a power meter Ophir Optronics Nova, with a 30A-P-SH sensor.
♣♣ - Determined from the Fresnel equations.

and 410 nm (between 410 and 412 nm), respectively, and subtracting the residual absorbance of RB at those wavelengths, which was estimated from the absorbance at 465 - 470 nm, with a correction factor determined from the spectrum of RB in absence of any sensor. The strategy described above was used to improve the signal-to-noise ratio of the measurement and correct for any potential baseline offsets.

2.2.5 Determination of $^1O_2$ sensor sensitivity

2.2.5.1 $^1O_2$ photogeneration by Rose Bengal

The irradiation of RB is one of the most common methods to photochemically generate $^1O_2$ in aqueous solutions, and RB is one of the molecules with the highest efficiencies of $^1O_2$ photogeneration in polar solvents, see Table 2.1.

Table 2.1 – Quantum yield of $^1O_2$ generation by RB, Φ_{RB}, in different solvents.

Solvent	Φ_{RB}
H_2O	0.75[4–6]
D_2O	0.76[4–8]
MeOH	0.80[5,8,9]

Unfortunately, the $^1O_2$ quantum yield of RB (Φ_{RB}) in ethanol or ethanolic mixtures is less well characterised. However, it has been reported that the Φ_{RB} in EtOH is similar to that in MeOH[5] and value of Φ_{RB} = 0.75 has been reported for 50/50 (v/v) MeOH/H_2O solution mixture.[10] Thus, the ABDA and DPBF sensitivity toward $^1O_2$ will be calculated from the absorbance variation of the chemical probes and a Φ_{RB} = 0.76 for all solvent mixtures tested (H_2O, D_2O, 50/50 (v/v) EtOH/H_2O and 50/50 (v/v) EtOH/D_2O).

The $^1O_2$ quantum yield of RB (Φ_{RB}) was reported to be independent of the concentration of RB and the excitation wavelength.[11–13] In line with this observation, RB in its ground state has also been reported not to quench $^1O_2$.[14] Finally, Φ_{RB} has been reported to be independent of the O_2 concentration under our irradiation conditions due to the large lifetime of the RB triplet state[7,12,13] - the reaction of O_2 with the triplet-RB is faster than the intrinsic triplet decay even at reduced O_2 concentrations.[7]

It is important to mention that parallel to the photogeneration of $^1O_2$, the irradiation of RB also photogenerates superoxide radical ($O_2^{-\cdot}$) with a yield of 0.2 in aqueous solutions.[7,15,16] This only had a minor effect on our results♣, see section 2.3.3.

2.2.5.2 The lifetime of singlet oxygen

Undoubtedly, the most important breakthrough in the scientific community of $^1O_2$ in the last fifty years was the development of tools to monitor the decay rates of $^1O_2$ directly by its characteristic phosphorescence emission at 1270 nm in time-resolved experiments.[2,17] These experiments allowed a more accurate determination of the $^1O_2$ lifetime (t_0), or its reciprocal parameter, the $^1O_2$ decay rate constant (k_0), in different solvent systems, revealing that the $^1O_2$ lifetime is extremely dependent on the environment where $^1O_2$ is located.[18] The deactivation back to the triplet ground state occurs mainly via non-radiative energy transfer to solvent vibrations.[18–20] The lifetime of $^1O_2$ in different solvents can be found in Table 2.2.

Table 2.2 – Lifetime of $^1O_2$ in different solvents found in the literature[18] and determined from a theoretical model.[19] The literature values shown are the average of the values obtained from the compilation of Wilkinson *et al.*.[18] The standard deviation of the latter are shown between brackets.

Solvent	t_0[18*] /µs	t_0 (Model) /µs
H_2O	4 (± 0.2)	4.2
D_2O	68 (± 3)	68
98/2 (v/v) D_2O/H_2O	---	52
EtOH	14 (± 2)	15
50/50 (v/v) $EtOH/H_2O$	---	6.6
50/50 (v/v) $EtOH/D_2O$	---	24

* - $^1O_2$ lifetimes obtained independently from $O_2(^1\Delta_g) \rightarrow O_2(^3\Sigma_g^-)$ phosphorescence measurements.

Note that the $^1O_2$ lifetime in H_2O is significantly smaller when compared to that in D_2O. This variation has been explained using a model which assumes that the overall $^1O_2$ decay rate constant is due to additive contributions from energy transfer to the different types of bonds which are proportional to the bond concentrations and bond-specific rate constants.[19–21] Since O-H vibration frequency is higher than O-D frequency and therefore, closer in energy to the $^1O_2$, the O-H is more efficient in quenching the $^1O_2$ state. This model was found to reproduce the lifetime of $^1O_2$ in H_2O, D_2O and EtOH accurately, as shown in Table 2.2 (column "Model"). Also, to the best of our knowledge,

♣ - Note that ABDA[24,35,36,42] does not react with $O_2^{-\cdot}$ but DPBF is known to do so.[37]

no experimental data have been reported for the $^1O_2$ lifetime in 50/50 (v/v) EtOH/H_2O or EtOH/D_2O. Due to the model consistency obtained for the $^1O_2$ lifetimes in H_2O, D_2O and EtOH, the same model was applied to the ethanolic mixtures and the $^1O_2$ lifetime calculated.

Finally, FTIR spectroscopy showed that our D_2O samples were contaminated with ~ 1% H_2O (see Appendix 2, Figure A2. 2). Since RB stock was always prepared in H_2O, of which typically 10 µL were added to a 1 mL sample, a total H_2O content of ~2% was present in our D_2O samples. For consistency, the same model was used to predict the $^1O_2$ lifetime in D_2O contaminated with 2% H_2O. The model predicted a reduction of the $^1O_2$ lifetime in D_2O from 68 to 52 µs upon addition of only 2% H_2O and a similar observation had been reported by Bilski *et al.*.[22] This interaction also effects the 1O2 lifetime (τ) described by the Stern-Volmer equation (Equation 2.1).

Equation 2.1

$$\frac{t_0}{\tau} = 1 + (k_r + k_q)t_0[S]$$

2.2.5.3 ABDA and DPBF reaction with singlet oxygen

Two different outcomes are possible when a $^1O_2$ molecule encounters either an ABDA or DPBF molecule. Its excess energy is either transferred to the molecular probe re-generating O_2 to its triplet ground state, or it chemically reacts with the molecular probe via [4+2]-cycloaddition, generating an endoperoxide, see Figure 1.5. These processes can be described as physical or chemical quenching by the sensor, with bimolecular rate constants, k_q and k_r respectively.

The $^1O_2$ physical quenching for DPBF has been reported to be negligible, i.e. $k_q < 0.1\ k_r$ in a range of solvents, including EtOH, MeOH, and mixtures of MeOH with H_2O or D_2O.[23] On the other hand, no information on the relative contribution of physical and chemical quenching of $^1O_2$ has been reported for ABDA. Yet, the rate constants for overall quenching ($k_q + k_r$) and chemical quenching (k_r) of $^1O_2$ in aqueous solutions by a similar anthracene-based molecule (9,10-anthracene dipropionic acid – ADPA) have been reported to be 8.2 x 10^7 M^{-1} s^{-1} [24] and 7.4 x 10^7 M^{-1} s^{-1} [25], respectively. The ratio of the reported values suggests that 11% of the $^1O_2$ molecules that interact with ADPA are physically quenched. Note that the latter conclusion is based on measurements by two different laboratories, hence their direct comparability is somewhat questionable. The

most direct and relevant observation in this context, obtained from one coherent set of data, is the report that $k_q/k_r = 0.35$ for another water-soluble anthracene derivative, 9,10-bis(ethanesulfonate)anthracene, determined both in H_2O and D_2O.[26] For consistency, this value will be used for the determination of the singlet oxygen sensitivity of ABDA.

2.2.5.4 Determination of singlet oxygen sensitivity

Here, the sensitivity of the $^1O_2$ sensor (Φ_S) is defined as the probability that a photogenerated $^1O_2$ reacts irreversibly with the molecular probe (S) before it is deactivated by solvent quenching, and it is related to the possible reaction pathways of $^1O_2$ outlined before, as shown in *Equation 2.2*,

Equation 2.2

$$\Phi_S = \frac{k_r\,[S]}{(k_r + k_q)[S] + k_0}$$

where k_r and k_q denote the bimolecular rate constants for the chemical reaction with S and physical quenching of $^1O_2$ by S, respectively, and k_0 the pseudo-first order rate constant for deactivation by the solvent, which is the inverse of the intrinsic lifetime summarised in Table 2.2. It is important to emphasise that Φ_S depends both on the molecular probe concentration [S] and on the solvent, which affects the intrinsic lifetime of $^1O_2$ (k_0), as explained before. Therefore, it is important to determine the value of Φ_S for each specific experimental condition. In contrast, the rate constants k_q and k_r are independent of the molecular probe concentration. Yet, viscosity and other solvent effects directly affect the value of the bimolecular rate constant for the reaction between $^1O_2$ and S.[27]

Φ_S was determined experimentally for each irradiation interval by calculating the number of sensor molecules which photobleached during the irradiation for a given time interval (Δt) and relating it to the amount of $^1O_2$ generated in the same time interval. The former is given by the measured absorbance change (ΔA), the extinction coefficient (ε), and the sample volume (V), whereas the latter can be calculated from the rate of photon absorption N_{abs} and the quantum yield of $^1O_2$ photogenerated by RB, as shown in *Equation 2.3*. d denotes the optical path-length and N_A Avogadro's constant.

Equation 2.3

$$\Phi_S = \frac{\Delta A \; V \; N_A}{\varepsilon \; d \; N_{abs} \; \Phi_{RB} \; \Delta t}$$

It is important to reinforce that *Equation 2.3* is only valid for small absorbance changes or short time intervals because the reaction probability of the molecular probe with $^1O_2$ is dependent on the probe concentration. Therefore, Φ_S changes throughout the irradiation, but *Equation 2.3* provides an absolute value which is independent of any assumptions regarding the relative contributions of k_q and k_r.

A more thorough approach is proposed here, which avoids the approximation of constant Φ_S over the experimental irradiation time intervals by explicitly accounting for the change of the molecular probe concentration and thus allows the analysis of the full data set. This methodology must consider the kinetics of the reaction. This approach is based on the observation that the steady-state concentration of $^1O_2$ at any given time t can be determined by equating the rates of its photogeneration and its decay via solvent quenching or reaction with a sensor molecule, *Equation 2.4*. This is possible because the lifetime of $^1O_2$ is significantly smaller than the experimental time scale (minutes).

Equation 2.4

$$\frac{N_{abs} \; \Phi_{RB}}{V \; N_A} = \; (k_0 + (k_r + k_q)[S])[\; ^1O_2]_{ss}$$

Using this steady-state concentration of $^1O_2$ yields the rate of bleach of molecular probe S due to reaction with $^1O_2$, *Equation 2.5*.

Equation 2.5

$$\frac{d[S]}{dt} = -\; k_r[S][^1O_2] = -k_r\,[S] \frac{N_{abs} \; \Phi_{RB}}{V \; N_A (k_0 + (k_r + k_q)[S])}$$

Equation 2.5 was integrated as a function of time, which yielded the relationship between the measured time-dependent molecular probe absorbance during irradiation, A(t), and time t, as shown in *Equation 2.6*. A_0 denotes the initial absorbance at t = 0 minutes. The integration is shown explicitly in Appendix 2, section A2.1.

Equation 2.6

$$t = C_1 \left(C_2 \ln \frac{A_0}{A(t)} + C_3 \left[A_0 - A(t) \right] \right)$$

$$C_1 = \frac{V N_A}{\varepsilon d N_{abs} \Phi_{RB}} \qquad C_2 = \frac{\varepsilon d k_0}{k_r} \qquad C_3 = \frac{k_r + k_q}{k_r}$$

The constant C_1 is determined by the $^1O_2$ quantum yield of RB, the extinction coefficient (ε) of the molecular probe and the experimental conditions (V, d, N_{abs}). Parameter C_2 relates the rate constant for the chemical quenching of $^1O_2$ by the sensor to the intrinsic $^1O_2$ lifetime ($1/k_0$), and C_3 provides the relationship of the rate constants for the physical and chemical quenching of $^1O_2$ by the sensor. Therefore, *Equation 2.6* was used to fit the experimental data, using a non-linear least-square fitting routine (Levenberg-Marquardt) using Origin. It was found that the time dependence of the two terms inside the brackets in *Equation 2.6* was not sufficiently different to allow an independent determination of the parameters C_2 and C_3 from our data. Therefore, the parameter C_3, which quantifies the relative contributions of physical and chemical quenching of $^1O_2$ by the molecular probe, was fixed to the values mentioned above (section 2.2.5.3). It will be shown below that the exact value chosen for C_3 does not significantly affect the $^1O_2$ sensitivity reported here, and it only has a minor effect on the rate constant k_r. Thus, the fits were performed with only two free fit parameters, C_2 and A_0. Finally, k_r and by extension k_q were determined from the value obtained for C_2, using the solvent-dependent intrinsic lifetimes of $^1O_2$ given in Table 2.2. The k_q and k_r values determined here from our data for different molecular probes and solvent conditions will be applied in the next chapter for the quantification of $^1O_2$ photogeneration quantum yield of AuNPs.

2.3 Results

2.3.1 Extinction coefficient

Figure 2.1 shows the UV-Vis spectra of ABDA, DPBF and RB. These show that the sensors do not have any absorbance at the excitation wavelength used in our experiments, 532 nm, whereas the sensitiser has almost no absorbance at the

wavelengths where the sensors have strong absorbance, 410 nm for DPBF and 380 or 400 nm for ABDA.

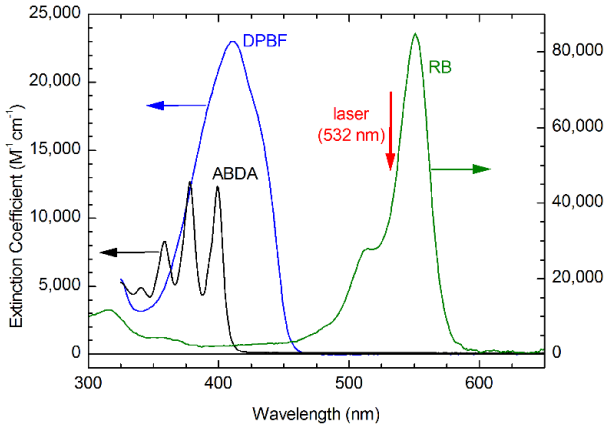

Figure 2.1 – UV-vis spectra of RB in H_2O (green, right scale), ABDA in H_2O (Black, left scale) and DPBF in 50/50 (v/v) EtOH/H_2O (Blue, left scale). The red arrow indicates the wavelength of the laser used for photosensitization.

Quantitative analysis of the sensor bleaching due to $^1O_2$, i.e. the determination of the singlet oxygen sensitivity, requires knowledge of the sensor extinction coefficient (see *Equation 2.3* and *Equation 2.6*). The exact values of the extinction coefficient are expected to depend on the solvent; moreover, values of the extinction coefficient of DPBF reported in the literature show some variability, whereas, to the best of our knowledge, no values for ABDA obtained with sufficient spectral resolution have been reported. Therefore, we accurately determined these values for the different solvents used here (Table 2.3).

Table 2.3 - Extinction coefficients of ABDA and DPBF in different solvents.

$^1O_2$ sensor	**Solvent**	**Wavelength[a] /nm**	**ε[b] /M-1 cm-1**
ABDA[c]	H_2O	398 - 400	11990 ± 60
	D_2O		11770 ± 90
	EtOH/H_2O[d]		13170 ± 40
	EtOH/D_2O[d]		13310 ± 60
DPBF	EtOH/H_2O[d]	410 - 412	23000 ± 250
	EtOH/D_2O[d]		22710 ± 140

[a] Wavelength range over which results were averaged, here and in the analysis of the photobleaching experiments.
[b] errors determined from the standard deviation of several repeat experiments.
[c] ABDA samples contained 1% (v/v) DMSO.
[d] 50/50 (v/v)

The extinction coefficient value determined for ABDA in H_2O and D_2O was found to be similar within the error of the measurement. Increasing the EtOH volume fraction to 50% resulted in a slight increase in the extinction coefficient. The extinction coefficient

of DPBF was found to be almost twice the value of that of ABDA. The extinction coefficients of DPBF reported here are in good agreement with literature values reported for organic solvents[28–30].

2.3.2 Sensor bleaching upon photoexcitation of Rose Bengal

The $^1O_2$ sensitiser, RB, and both $^1O_2$ molecular probes, ABDA and DPBF, when used separately, are stable in the dark, as well as under the irradiation conditions used here, see Appendix 2, Figure A2. 1. Yet, the irradiation of ABDA or DPBF in the presence of RB resulted in photobleaching of both molecular probes, as expected due to their reaction with $^1O_2$ generated by the irradiation of RB, i.e. the cycloaddition reactions (see Introduction Figure 1.5) which result in the loss of absorbance in the near UV or visible spectral region because of the disruption of the conjugated π-system of the endoperoxide product. The observed photobleach in the presence of RB agrees with the well-known ability of ABDA and DPBF to act as $^1O_2$ molecular probes. Figure 2.2 shows the absorbance change of ABDA (A) and DPBF (B) in 50/50 (v/v) EtOH/D_2O upon CW-irradiation at 532 nm with a laser power of 0.14 mW in the presence of RB. Note that the ABDA spectra were taken every 10 minutes over a time interval of 40 minutes, whereas DPBF spectra were taken every minute over a time interval of 8 minutes.

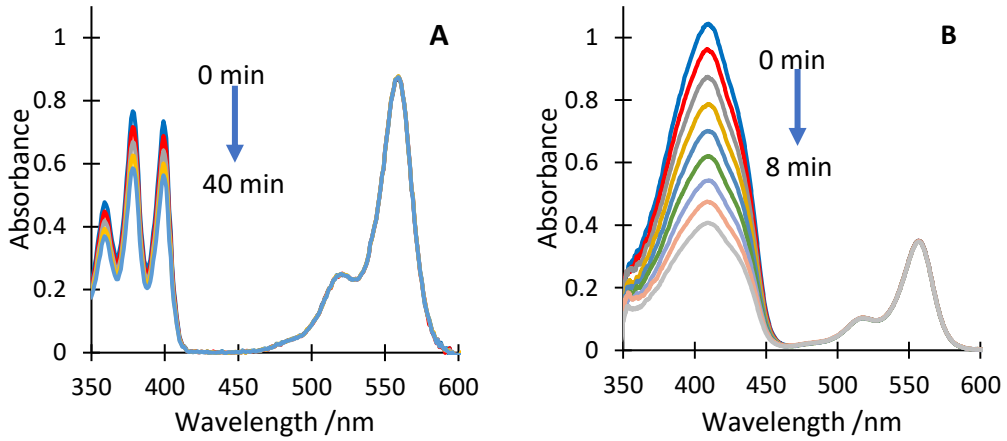

Figure 2.2 - Photobleaching of ABDA (A) and DPBF (B) in 50/50 (v/v) EtOH/D_2O upon CW-irradiation at 532 nm with a laser power of 0.14 mW in the presence of RB; the spectra were taken every 10 minutes over a time interval of 40 minutes (ABDA – A) and every minute over a time interval of 8 minutes (DPBF – B).

It was observed that, under the same irradiation conditions, ABDA photobleached at a significantly lower rate when compared with DPBF, in spite of the higher $^1O_2$ photogeneration resulting from the higher RB concentration used in these

particular sets of experiments, see Figure 2.2 A and B. This is partly due to the higher extinction coefficient of DPBF determined in the previous section (see Table 2.3); however, it is also a clear indication, that DPBF has a significantly higher sensitivity for $^1O_2$ when compared to ABDA, which will be quantified below. Lastly, no variation of the RB absorbance was observed under our irradiation conditions. Hence it can be concluded that the $^1O_2$ photogeneration rate is constant throughout the irradiation experiment.

The irradiation was performed again for different solvents, and the photobleach of ABDA and DPBF evaluated. For a first comparison, the sensor absorbance was normalised to the absorbance at the start of the irradiation. It is important to emphasise that the concentration of RB varied to some extent between the different experiments (as shown in Figure 2.2) so that they are not fully quantitatively comparable. Figure 2.3 shows the photobleaching of ABDA and DPBF in different solvents in the presence of RB upon CW-irradiation at 532 nm with 0.14 mW (A) or 2.4 mW (B).

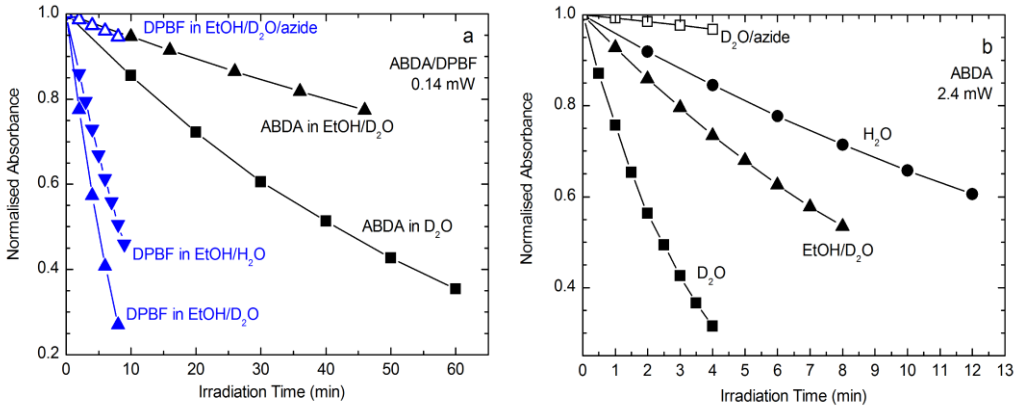

Figure 2.3 – Photobleaching of ABDA (black) and DPBF (blue) in different solvents upon irradiation with 0.14 mW (A) or 2.4 mW (B) CW laser light at 532 nm in the presence of RB; shown here is the sensor absorbance at 398-400 nm (ABDA) or 410-412 nm (DPBF), normalised to the absorbance at the start of the irradiation, averaged over several repeat experiments at a similar concentration of RB, resulting in standard deviations for the individual data points, which are smaller than the size of the symbols; however, the concentration of RB (~ 2-4 µM) varied slightly in the different experiments, and hence the amount of photogenerated $^1O_2$ varied between the different curves, so that they are quantitatively not fully comparable; solid and open symbols refer to measurements in the absence and presence of 20 mM NaN_3, respectively; mixed solvents are 50/50 (v/v) mixtures.

The results presented above show several trends clearly:

(i) the solvent has a significant effect on the sensor bleaching, with particularly pronounced bleaching found in D_2O, whereas the slowest bleaching occurs in H_2O, in good agreement with the solvent-dependent $^1O_2$ lifetimes summarised in section 2.2.5.2;

(ii) as already shown in Figure 2.2, when comparing results in the same solvent, ABDA bleaches significantly more slowly than DPBF, suggesting that it has a significantly lower sensitivity for $^1O_2$ than DPBF;

(iii) the addition of the $^1O_2$ quencher NaN_3 suppresses the photobleaching almost completely, which proves that photobleaching is largely due to $^1O_2$, as discussed in more detail in the next section.

2.3.3 Sensor bleaching due to singlet oxygen

Before the analysis and discussion of the irradiation results, it is important to highlight that the literature suggests two alternative mechanisms for the photobleaching of ABDA and DPBF upon photoexcitation of RB which do not involve the generation of $^1O_2$, namely:

i) Quenching of triplet state of RB by the molecular probes which leads to the sensor bleach (Equation 2.7).

ii) Photogeneration of superoxide radical ($O_2^{-\cdot}$) by RB and reaction with the sensor (Equation 2.8).

Equation 2.7

$$^3RB + S \rightarrow RB + \ ^3S \overset{O_2}{\rightarrow} RB + S - O_2$$

Equation 2.8

$$^3RB + O_2 \rightarrow RB + \ O_2^{-\cdot} \overset{S}{\rightarrow} RB + S - O_2$$

According to the literature, the energy of the triplet states of 9,10-substituted anthracene moieties[31,32], DPBF[33] and RB[9] are ~41, ~34 and ~41 kcal mol^{-1}, which suggests that the quenching of ^{3}RB energy by ABDA and DPBF is possible (to generate ^{3}ABDA and ^{3}DPBF). It has been shown experimentally that in the presence of a well-known $^1O_2$ quencher (NaN_3), an anthracene derivative similar to ABDA (9,10-anthracene dipropionic acid (ADPA)) still bleaches (~23% of the bleach in the absence of NaN_3) upon RB photosensitization, that is, NaN_3 was not able to quench all of the ADPA bleach upon RB photosensitization even at saturating concentrations.[6] To explain this observation, the authors suggest that ADPA is excited to the triplet state (^{3}ADPA) by energy transfer from

^{3}RB and then reacts with ground state oxygen.[6] These conclusions were confirmed in experiments which directly measured the rate constant for quenching of ^{3}RB by ADPA and O_2, respectively.[7] In similar experiments, the rate of DPBF photobleach upon RB irradiation in pyridine has been shown to drop to approximately 10% of the quencher-free rate in the presence of tetramethylethylene ($^1O_2$ quencher) at saturating concentrations, which suggests that DPBF has a small contribution to its photobleach due to a triplet energy transfer from ^{3}RB to DPBF.[34]

The generation of $O_2^{-\cdot}$ upon photoexcitation of RB, with a yield of approximately 0.20 in aqueous solution,[7,15,16] provides another possible mechanism for the observed photobleaching of DPBF. Note that anthracene-based sensors such as ABDA do not react with $O_2^{-\cdot}$.[24,35,36]

To investigate the contribution of the two alternative mechanisms, we repeated the irradiation experiments in the presence of NaN_3 (20 mM). NaN_3 is a well-characterized $^1O_2$ quencher,[6] does not interfere with the triplet energy transfer from RB to ABDA or DPBF and does not quench $O_2^{-\cdot}$.[37] A concentration of 20 mM NaN_3 was chosen because it is above the concentration at which saturation of $^1O_2$ quenching was observed experimentally.[7] As shown in Figure 2.3 A and B, a significant reduction of the ABDA and DPBF photobleach in the presence of NaN_3 was observed. The rate of absorbance bleach of ABDA in D_2O in the presence of NaN_3 was found to be only 4% of that in the absence of NaN_3 under identical irradiation conditions. A similar observation has been reported in the literature.[38] In the case of DPBF, the addition of NaN_3 reduced the rate of the photobleach to 5 and 10% in EtOH/D_2O and EtOH/H_2O respectively, when compared to the irradiation results in the absence of NaN_3. Our irradiation results show that, neither the triplet state energy transfer from ^{3}RB to the sensor nor the generation of $O_2^{-\cdot}$ upon photoexcitation of RB greatly affect the outcome of the experiments presented in the previous section. For ABDA and DPBF in EtOH/D_2O, the observed effect from these two reported mechanisms is at most a few percent, essentially within the uncertainty of our irradiation results, whereas for DPBF in EtOH/H_2O, our $^1O_2$ sensitivity results (Table 2.4) might be overestimated by at most 10% when neglecting these effects. Therefore, we conclude that photobleach of DPBF and ABDA directly reflects the reaction of the molecular probes with $^1O_2$ generated by the RB photosensitization.

2.3.4 Singlet oxygen sensitivity

The sensitivity of a $^1O_2$ sensor (Φ_S) for the different solvents was determined experimentally from the amount of $^1O_2$ generated during the irradiation for a given time interval and the number of sensor molecules which bleach in this time interval, determined by the bleach of the sensor absorbance (*Equation 2.3*).

This analysis yielded Φ_S values of 0.018, 0.05 and 0.12 for ABDA in H_2O, 50/50 (v/v) EtOH/D_2O and D_2O, respectively, and 0.4 and 0.65 for DPBF in 50/50 (v/v) EtOH/H_2O and 50/50 (v/v) EtOH/D_2O, respectively. Note that the values reported are regarding the first irradiation interval for the data presented in Figure 2.3. It should also be noted that these values do not depend on the concentration of RB, but depend on the concentration of the molecular probe, which here was chosen so that the initial sensor absorbance was in the vicinity of 1. Due to the concentration dependence of the molecular probe, the Φ_S value decreases as the irradiation progresses. It is important to reinforce that Φ_S determined is not a universally applicable number due to its dependence on the sensor concentration and variation during the experiment. However, Φ_S can be calculated for any given concentration from the rate constants k_q and k_r, which are independent of the sensor concentration (*Equation 2.2*). Here, we determined the values of these rate constants for ABDA and DPBF in different solvents and then used them for comparing the $^1O_2$ sensitivity of these sensors at concentrations corresponding to a sensor absorbance of 1 in a 1 cm pathlength cell, which are the typical experimental conditions, since it allows for high signal-to-noise absorbance measurements.

k_q and k_r were determined from the non-linear least-square fitting routine described in section 2.2.5.4, based on the time-dependent sensor absorbance data. Some example sets of experimental data and the resulting fits are shown in appendix A2, Figure A2. 3, which shows that *Equation 2.6* allows a good fit of all our data. Similarly, a summary of the fit results obtained for a wide range of values of C_3 (Appendix 2, Table A2. 1) shows that the k_r results reported here do not greatly depend on the exact value of C_3 assumed in the fits, if these are kept within a reasonable range from those suggested by the literature, as discussed in the section 2.2.5.3.

More specifically, the value of k_q for DPBF has been reported to be less than 10% of that of k_r ($C_3 < 1.1$), see section 2.2.5.3. Our fit attempts directly rule out values of $C_3 \geq 1.6$ for DPBF since they lead to a poorer fit (see appendix A2, Figure A2. 4). Increasing the

C_3 value from 1.2 to 1.6 showed to increase the value of k_r obtained in EtOH/D_2O and EtOH/H_2O, and the reaction becomes faster in EtOH/D_2O than in EtOH/H_2O for $C_3 \geq 1.2$. However, the viscosity of D_2O is higher than that of H_2O, which contradicts the latter observation and further supports the literature evidence of negligible physical quenching of $^1O_2$ by DPBF. Therefore, we will use the fit results obtained for $C_3 = 1$.

As for ABDA, no literature values were available for C_3. As shown in appendix A2 Table A2.1, C_3 can be varied between 1 and 2 without significantly affecting the k_r values, which can be explained by the low reactivity of ABDA towards $^1O_2$, i.e. $(k_r+k_q)[S] << k_0$, so that *Equation 2.2* can be approximated to $\Phi_S = k_r[S]/k_0$ (i.e., independent of k_q). Here, we will use the fit results obtained for $C_3 = 1.35$ which is the value obtained in the most direct and relevant experimental report obtained from one coherent set of data for 9,10-bis(ethanesulfonate)anthracene in H_2O and D_2O.[26]

Finally, it is important to stress that our experiments were undertaken at different laser powers and with different concentrations of RB. Although both factors directly affect the rate of $^1O_2$ generation and, by consequence, the rate of sensor bleaching, there was no effect of either of these factors on the resulting values of the rate constant k_r within the error of the measurement. Table 2.4 summarises the k_r and Φ_S results determined from the fit of the experimental data.

Table 2.4 – Rate constant k_r for the deactivation of $^1O_2$ by a chemical reaction with ABDA and DPBF and resulting $^1O_2$ sensitivity for a molecular probe concentration corresponding to a maximum absorbance of 1 in different solvents.

$^1O_2$ sensor	**Solvent**	**k_r (10^7 $M^{-1}s^{-1}$)[a]**		**Φ_S[a]**	
ABDA[b,c]	H_2O	5.63	+/- 0.12	0.0192	+/- 0.0004
	D_2O	3.98	+/- 0.18	0.175[e]	+/- 0.005
	EtOH/D_2O[f]	2.79	+/- 0.14	0.050[e]	+/- 0.002
DPBF[d]	EtOH/H_2O[f]	283	+/- 11	0.449	+/- 0.010
	EtOH/D_2O[f]	231	+/- 9	0.722[e]	+/- 0.008

[a] Errors determined from the standard deviation of several repeat experiments
[b] ABDA samples contained 1% (v/v) DMSO
[c] Data analysed with $C_3 = 1.35$
[d] Data analysed with $C_3 = 1$
[e] Assuming neat solvents, i.e. no contamination by H_2O
[f] 50/50 (v/v)

Our results show that the reactivity of DPBF with $^1O_2$ is significantly higher than that of ABDA, with a rate constant which is almost two orders of magnitude larger when comparing the same solvents. A closer look at the results showed that the bimolecular

rate constant k_r changes for both sensors when replacing H_2O by D_2O, as expected from the higher viscosity of D_2O (~ 25% higher with respect to H_2O), which results in a slower diffusion of O_2.[39] In concordance, the higher viscosity of a 50/50 (v/v) mixture of EtOH and D_2O (see Table 3.2) slows down the reaction even further when compared to neat H_2O or D_2O. Further discussion of the bimolecular rate constant k_r will be given below (section 2.3.5).

Regarding the $^1O_2$ sensitivities at sensor concentrations corresponding to a maximum absorbance of 1 for ABDA and DPBF in different solvents, the value of Φ_S reflects the variation of viscosity as well as the $^1O_2$ lifetime. A shorter lifetime, such as 4 μs in H_2O, makes the sensitivity significantly smaller when compared to that in D_2O, which has a $^1O_2$ lifetime of 68 μs, hence making the detection of $^1O_2$ in H_2O significantly more challenging than in D_2O. Also, the higher extinction coefficient of DPBF in comparison to ABDA makes DPBF as $^1O_2$ sensor even more sensitive in practical terms.

2.3.5 Discussion

It is important to highlight that k_r is highly dependent on the solvent (see Table 2.4), therefore it is important to be careful when comparing our k_r values with the ones found in the literature because the absolute rate constants for the chemical quenching may vary significantly in different solvents. For this reason, we will compare the values of k_r determined from our experiments with values found in the literature for the same solvent conditions, when possible, or similar solvents where the value of k_r is not expected to change considerably.

In general, the bimolecular rate constants (k_r) found from our irradiation experiments agree, within an order of magnitude, with the values reported in the literature. More specifically for DPBF, our results yielded a k_r of 2.8×10^9 and 2.3×10^9 M^{-1} s^{-1} in a 50/50 (v/v) solution mixture of EtOH/H_2O and EtOH/D_2O, respectively. In comparison, Krasnovsky Jr.[40] reported a k_r for DPBF in ethanol of 1×10^9 M^{-1} s^{-1}. Similarly, in independent studies, Merkel *et al.*[41] and Young *et al.*[29] reported values of k_r in methanol of 1.3×10^9 and 0.8×10^9 M^{-1} s^{-1}, respectively. The latter authors further expanded their study and determined a k_r for DPBF in 50/50 (v/v) MeOH/H_2O of 5.1×10^9 M^{-1} s^{-1} which appears to be in good agreement with our value in 50/50 (v/v) EtOH/H_2O, when taking into account the higher viscosity of MeOH when compared to that of EtOH. From another

perspective, we also determined the theoretical maximum diffusion-limited rate constant for a bimolecular reaction between DPBF and $^1O_2$ (for further details, see section 3.5.5, equation 3.5). Assuming an effective radius of DPBF of 0.75 nm, the theoretical maximum value of k_r in 50/50 (v/v) EtOH/H_2O was found to be 4 x 10^9 M^{-1} s^{-1}. This value is in good agreement with the value of k_r determined experimentally, thus showing that the reaction between DPBF and $^1O_2$ is diffusion-limited. Lastly, as highlighted in the previous section, the variation of k_r determined for DPBF in 50/50 (v/v) EtOH/H_2O and EtOH/D_2O is mainly due to the viscosity of the solvent.

As for ABDA, our results yielded values of k_r of 5.6 x 10^7, 4.0 x 10^7 and 2.8 x 10^7 M^{-1} s^{-1} in H_2O, D_2O and 50/50 (v/v) EtOH/D_2O, respectively, and, as far as we are aware, no literature values have been reported for ABDA. Nonetheless, a similar molecule has been studied - anthracene-9,10 diproprionic acid (ADPA). Lindig *et al.*[24], Gimenez *et al.*[25] and Aubry *et al.*[27] reported values for (k_r + k_q) of 8.2 x 10^7 , 7.4 x 10^7 and 9.7 x 10^7 M^{-1} s^{-1} for ADPA in D_2O, respectively. The (k_r + k_q) values reported by the authors are slightly higher when compared to the value of (k_r + k_q) found in our D_2O experiments 5.4 x 10^7 M^{-1} s^{-1}, taking into consideration C_3= 1.35, as described above. It is reasonable to suggest that the slight difference is due to the ABDA being a slightly different molecule, hence it affects the reactivity of ABDA towards $^1O_2$ slightly. Also, when comparing the value of k_r with the theoretical maximum value determined above, it is clear that the reaction is not diffusion limited as concluded for DPBF, hence other factors which directly affect the reaction probability upon an encounter will play a role in the reaction. In particular, the larger side chains of ABDA would be expected to increase steric hindrance for the access of $^1O_2$ to the aromatic ring compared to the smaller side chains of ADPA.

2.4 Conclusion

Overall, we determined the $^1O_2$ sensitivities for ABDA and DPBF in different solvents. DPBF is significantly more sensitive to $^1O_2$ when compared to ABDA, but it is insoluble in neat aqueous conditions whereas ABDA has the advantage of being useful in fully aqueous solvents, and it is relatively easier to work with when compared with DPBF.

From all solvent conditions tested during our irradiation experiments, the conditions where a deuterated solvent was present were the ones that yielded a higher $^1O_2$ sensitivity, both for DPBF and ABDA, due to the longer $^1O_2$ lifetime.

Finally, the knowledge of the bimolecular rate constant k_r and the $^1O_2$ sensitivity which can be calculated from this rate constant for given experimental conditions will allow us to study different photosensitisers further and evaluate the amount of $^1O_2$ generated. More specifically, it will allow us to measure the quantum yield of $^1O_2$ generated by AuNPs.

2.5 References

(1) Blázquez-castro, A. Redox Biology Direct $^1O_2$ Optical Excitation : A Tool for Redox Biology. *Redox Biol.* **2017**, *13*, 39.

(2) Jockusch, S.; Turro, N. J.; Thompson, E. K.; Gouterman, M.; Callis, B.; Khalil, G. E.; Callis, J. B.; Khalil, G. E. Singlet Molecular Oxygen by Direct Excitation. *Photochem. Photobiol. Sci.* **2008**, *7*, 235.

(3) Pitts Jr. J.; Hammond G.; Noyes Jr. W.; Advances in Photochemistry, John Wiley & Sons, Inc., Volume 7, 1969.

(4) Nardello, V.; Brault, D.; Chavalle, P.; Aubry, J. M. M. Measurement of Photogenerated Singlet Oxygen ($^1O_2(^1\Delta_g)$) in Aqueous Solution by Specific Chemical Trapping with Sodium 1,3-Cyclohexadiene-1,4-Diethanoate. *J. Photochem. Photobiol. B Biol.* **1997**, *39*, 146.

(5) Wilkinson, F; Phillip W. Quantum Yields for the Photosensitized Formation of the Lowest Electronically Excited Singlet State of Molecular Oxygen in Solution. *J. Phys. Chem. Ref. Data* **1993**, *22*, 113.

(6) Gandin, E.; Lion, Y.; Van de Vorst, A. Quantum yield of singlet oxygen production by xanthene derivatives. *Photochem. Photobiol.* **1983**, *37*, 271.

(7) Lee, P.; Rodgers, M. Laser flash photokinetic studies of Rose Bengal sensitized photodynamic interactions of nucleotides and DNA. *Photochem. Photobiol.* **1987**, *45*, 79.

(8) Redmond, R. W.; Gamlin, J. N. A Compilation of Singlet Oxygen Yields from Biologically Relevant Molecules. *Photochem. Photobiol.* **1999**, *70*, 391.

(9) Gollnick, K.; Franken, T.; Schade, G.; Dörhöfer, G. Photosensitized oxygenation as a function of the triplet energy of sensitizers. *Ann. N. Y. Acad. Sci.* **1970**, *171*, 89.

(10) Wagner, Jr; Ali, H.; Langlois, R.; Brasseur, N.; Ller, J. E. Biological activities of Phthalocyanines - VI. Photooxidation of L-tryptophan by selectively sulfonated gallium phthalocyanines: singlet oxygen yields and effect of aggregation. *Photochem. Photobiol.* **1987**, *45*, 587.

(11) Bilski, P.; Dabestani, R.; Chignell, C. F. Influence of Cationic Surfactant on the Photoprocesses of Eosine and Rose Bengal in Aqueous Solution. *J. Phys. Chem.* **1991**, *95*, 5784.

(12) Gollnick, K.; Schenck, G. O. Mechanism and Stereoselectivity of Photosensitized Oxygen Transfer Reactions. *Pure Appl. Chem.* **1964**, *9*, 507.

(13) Lion, Y.; Gandin, E.; Vorst, A. On the production of nitroxide radicalsby singlet oxygen reaction: an EPR study. *Photochem. Photobiol.* **1980**, *31*, 305.

(14) Tanielian, C.; Golder, L. Quenching of singlet oxygen by sensitizer in dye-sensitized photooxigenation. *Photochem. Photobiol.* **1981**, *34*, 411.

(15) Srinivasan, V. S.; Podolski, D.; Westrick, N. J.; Neckers, D. C. Photochemical Generation of Superoxide Ion (O_2^-) by Rose Bengal and $Ru(Bpy)_3^{2+}$. *J. Am. Chem. Soc.* **1978**, *100*, 6513.

(16) Murasecco-Suardi, P.; Gassmann, E.; Braun, A. M.; Oliveros, E. Determination of

the Quantum Yield of Intersystem Crossing of Rose Bengal. *Helv. Chim. Acta* **1987**, *70*, 1760.

(17) Niedre, M.; Patterson, M. S.; Wilson, B. C. Direct Near-Infrared Luminescence Detection of Singlet Oxygen Generated by Photodynamic Therapy in Cells In Vitro and Tissues In Vivo. *Photochem. Photobiol.* **2010**, *75*, 382.

(18) Wilkinson, F.; Helman, W. P.; Ross, A. B. Rate Constants for the Decay and Reactions of the Lowest Electronically Excited Singlet State of Molecular Oxygen in Solution. An Expanded and Revised Compilation. *J. Phys. Chem. Ref. Data* **1995**, *24*, 663.

(19) Schmidt, R.; Afshari, E. Collisional Deactivation of $O_2(^1\Delta_g)$ by Solvent Molecules. Comparative Experiments with $^{16}O_2$ and $^{18}O_2$. *Berichte der Bunsengesellschaft für Phys. Chemie* **1992**, *96*, 788.

(20) Rodgers, M. Solvent-Induced Deactivation of Singlet Oxygen: Additivity Relationships in Nonaromatic Solvents. *J. Am. Chem. Soc.* **1983**, *105*, 6201.

(21) Hurst, J. R.; Schuster, G. B. Nonradiative Relaxation of Singlet Oxygen in Solution. *J. Am. Chem. Soc.* **1983**, *105*, 5756.

(22) Bilski, P.; Holt, R. N.; Chignell, C. F. Properties of Singlet Molecular Oxygen $O_2(^1\Delta_g)$ in Binary Solvent Mixtures of Different Polarity and Proticity. *J. Photochem. Photobiol. A Chem.* **1997**, *109*, 243.

(23) Merkel, P. B.; Kearns, D. R. Rate Constant for the Reaction between 1,3-Diphenylisobenzofuran and Singlet Oxygen. *J. Am. Chem. Soc.* **1975**, *97*, 462.

(24) Lindig, B. A.; Rodgers, M. A. J. J.; Schaaplc, A. P.; Schaap, A. P. Determination of the Lifetime of Singlet Oxygen in Water-D_2 Using 9,10-Anthracenedipropionic Acid, a Water-Soluble Probe. *J. Am. Chem. Soc.* **1980**, *102*, 5590.

(25) Giménez, R. E.; Vargová, V.; Rey, V.; Turbay, M. B. E.; Abatedaga, I.; Morán Vieyra, F. E.; Paz Zanini, V. I.; Mecchia Ortiz, J. H.; Katz, N. E.; Ostatná, V.; Borsarelli, C. D. Interaction of Singlet Oxygen with Bovine Serum Albumin and the Role of the Protein Nano-Compartmentalization. *Free Radic. Biol. Med.* **2016**, *94*, 99.

(26) Evans, D. F.; Upton, M. W. Studies on Singlet Oxygen in Aqueous Solution. Part 1. Formation of Singlet Oxygen from Hydrogen Peroxide with Two-Electron Oxidants. *J. Chem. Soc. Dalt. Trans.* **1985**, 6, 1141.

(27) Aubry, J.; Mandard-Cazin, B.; Rougee, M.; Bensasson, R. Kinetic Studies of Singlet Oxygen [4+2]-Cycloadditions with Cyclic 1,3-Dienes in 28 Solvents. *J. Am. Chem. Soc.* **1995**, *117*, 9159.

(28) Gorman, A..; Lovering, G.; Rodgers, M., Pulse Radiolysis Study of the Triplet Sensitized Production of Singlet Oxygen: Determination of Energy Transfer Efficiencies. *J. Am. Chem. Soc.* **1978**, *100*, 4527.

(29) Young, R. H.; Brewer, D.; Keller, R. A. Determination of Rate Constants of Reaction and Lifetimes of Singlet Oxygen in Solution by a Flash Photolysis Technique. *J. Am. Chem. Soc.* **1973**, *95*, 375.

(30) Singh, A.; McIntyre, N. R.; Koroll, G. W. Photochemical formation of metastable species from 1,3-diphenylisobenzofuran, *Photochem. Photobiol.* **1978**, *28*, 595.

(31) Chattopadhyay, S. K.; Kumar, C. V.; Das, P. K. Triplet-Related Photophysics of 9,10-

Diphenylanthracene. A Kinetic Study of Reversible Energy Transfer from Anthracene Triplet by Nanosecond Laser Flas. *Chem. Phys. Lett.* **1983**, *98*, 250.

(32) Brinen, J. S.; Koren, J. G. The Lowest Triplet State of 9,10-Diphenylanthracene. *Chem. Phys. Lett.* **1968**, *2*, 671.

(33) Herkstroeter, W. G.; Merkel, P. B. The Triplet State Energies of Rubrene and Diphenylisobenzofuran. *J. Photochem.* **1981**, *16*, 331.

(34) Wilson, T. Excited Singlet Molecular Oxygen in Photooxidation. *J. Am. Chem. Soc.* **1966**, *88*, 2898.

(35) Umezawa, N.; Tanaka, K.; Urano, Y.; Kikuchi, K.; Higuchi, T.; Nagano, T.; Cryst, M.; Cryst, L.; Kaupp, G. Novel Fluorescent Probes for Singlet Oxygen. *Angew. Chemie-International Ed.* **1999**, *38*, 2899.

(36) Gomes, A.; Fernandes, E.; Lima, J., Fluorescence Probes Used for Detection of Reactive Oxygen Species. *J. Biochem. Biophys. Methods* **2005**, *65*, 45.

(37) Ohyashiki, T.; Nunomura, M.; Katoh, T. Detection of Superoxide Anion Radical in Phospholipid Liposomal Membrane by Fluorescence Quenching Method Using 1,3-Diphenylisobenzofuran. *Biochim. Biophys. Acta - Biomembr.* **1999**, *1421*, 131.

(38) Kuznetsova, N. A.; Gretsova, N. S.; Yuzhakova, O. A.; Negrimovskii, V. M.; Kaliya, O. L.; Luk'yanets, E. A. New Reagents for Determination of the Quantum Efficiency of Singlet Oxygen Generation in Aqueous Media. *Russ. J. Gen. Chem.* **2001**, *71*, 36.

(39) Han, P.; Bartels, D. M. Temperature Dependence of Oxygen Diffusion in H_2O and D_2O, *J. Phys. Chem.* **1996**, *100*, 5597.

(40) Krasnovsky, A. A.; Luminescence and Photochemical Studies of Singlet Oxygen Photonics. *J. Photochem. Photobiol. A Chem.* **2008**, *196*, 210.

(41) Merkel, P. B.; Kearns, D. R. Radiationless Decay of Singlet Molecular Oxygen in Solution. Experimental and Theoretical Study of Electronic-to-Vibrational Energy Transfer. *J. Am. Chem. Soc.* **1972**, *94*, 7244.

(42) Dąbrowski, J. M. Reactive Oxygen Species in Photodynamic Therapy: Mechanisms of Their Generation and Potentiation. *Adv. Inorg. Chem.* **2017**, *70*, 343.

Chapter 3

3. Gold nanoparticles as singlet oxygen photosensitisers

3.1 Introduction

Recently, the use of AuNPs has increased significantly in biomedical applications.[1] In particular, they have been suggested as useful sensitising agents in PDT due to their unique size and shape-dependent optical properties, high absorption coefficient and biocompatibility.[2–6] It has been suggested that citrate-stabilised AuNPs can generate $^1O_2$ when excited at their SPR.[7–11] The photogeneration of $^1O_2$ has been investigated both by a direct detection approach via the characteristic $^1O_2$ luminescence at 1270 nm,[7,8] and by indirect methods using chemical traps.[7,9,10] However, the efficiency with which AuNPs can generate $^1O_2$ is still in question at this point. Some authors reported a $^1O_2$ photogeneration quantum yield of ~ 3 – 4 %[7,8] upon irradiation of AuNPs while others report a much lower quantum yield of an order of magnitude of 10^{-6}.[9,10]

Here, we show conclusively that the irradiation of 15 – 16 nm AuNPs in their surface plasmon band with CW laser light (at 532 nm) leads to the generation of $^1O_2$, detected indirectly by the variation of the absorbance of ABDA and DPBF. We further use the reactivity of the chemical probes ABDA and DPBF towards $^1O_2$, determined in the previous chapter, to accurately determine the efficiency with which AuNPs can generate $^1O_2$ and compare it to the literature.

3.2 Experimental

3.2.1 Materials

ABDA, gold (III) chloride trihydrate, trisodium citrate, sucrose, hydrochloric acid (HCl), nitric acid (HNO_3) and D_2O were purchased from Sigma-Aldrich and DPBF, EtOH and DMSO were purchased from Fisher Scientific. Oxygen (O_2, 99.5%) and Nitrogen (N_2 – oxygen-free) gases were purchased from BOC. All chemicals were used as received. Milli-Q water (>18.2 MΩ cm) was prepared freshly before the experiment using a Barnstead Smart2Pure water purification system (Thermo Scientific).

Before use, all glassware, cuvettes and stirrer bars were cleaned in Aqua Regia (3:1 HCl:HNO_3) and thoroughly rinsed with Milli-Q water and set to dry. A more detailed protocol for the cleaning of cuvettes and stirrer bars for the irradiation experiments, as well as a discussion of the importance of a thorough cleaning, can be found in Appendix 1, section A1.1. All solutions were prepared and kept stirring until used. All sample preparations involving the chemical traps were carried out in the dark.

3.2.2 Gold nanoparticles

3.2.2.1 Gold nanoparticles preparation

Citrate-stabilized AuNPs (AuNPs@Citrate) were synthesised by citrate reduction of $HAuCl_4$ according to the Turkevich-Frens method.[12,13]

$$3\ C_3H_5O(COO)_3^{3-} + 2\ Au^{3+} \rightarrow 3\ C_3H_4O(COO)_2^{2-} + 2\ Au^0 + 3\ CO_2 + 3\ H^+$$

The AuNPs were prepared both in Milli-Q water and D_2O. In a 250 mL round bottom flask, 150 mL of 0.3 mM $HAuCl_4$ solution was heated to the boiling point and left refluxing while stirring for 5 minutes. Then 4.5 mL of a 34 mM trisodium citrate solution was quickly added to the reflux solution, and the mixture was left refluxing. The AuNPs synthesised in Milli-Q H_2O were refluxed for a further 30 minutes while the ones synthesised in D_2O were refluxed for 35 minutes. This additional five minutes of reflux in D_2O were needed to overcome the effect of solvent isotopic replacement (H for D) and achieve a similar size of AuNPs in both solvents, as demonstrated by Ojea-Jimenez *et al.*.[14]

Upon addition of trisodium citrate, the solution colour changed from light yellow to transparent, to black and finally to a deep red colour, characteristic of the AuNPs. After the reflux period, the heater mantle was turned off and removed from the setup. The solution was left stirring and allowed to cool overnight. The AuNPs solution was filtered through a fluted filter paper, stored in the fridge and characterised by UV-Vis spectroscopy and differential centrifugal sedimentation (DCS).

The H_2O content of the AuNPs in D_2O samples was monitored and confirmed by FTIR spectroscopy. The FTIR spectra were recorded on a Bio-Rad FTS-40 FTIR spectrometer, using an IR cell with CaF_2 windows and 50 µm pathlength. The intensity of the O-H stretch vibration at 3400 cm^{-1} was measured and the effective H_2O content determined according to the molar absorptivity of the O-H stretch vibration.[15] The H_2O content increased slightly, from 1.5% to 2%, over six months, see Appendix 3 – Figure A3. 1. For analysis purposes, the AuNPs in D_2O samples were considered to be contaminated with 2% H_2O content, since all relevant experiments were undertaken a few months after NP synthesis.

3.2.2.2 Gold nanoparticles characterisation

The UV-Vis absorption spectra were recorded with a GENESYS™ 10S UV-Vis spectrophotometer at room temperature, using a cuvette with a path length of 1 cm. The AuNPs size distribution was measured by DCS using a DCS disc centrifuge DC24000 (CPS Instruments Inc.). The DCS rotating disc (at 24 000 rpm) was loaded with a freshly prepared 8% wt. % sucrose in Milli-Q H_2O and, over nine successive additions, the sucrose concentration was increased to 24 wt. %. The system was calibrated before each sample measurement against 377 nm poly(vinyl chloride) particles (Analytik Ltd.). All samples were analysed at least three times to verify data reproducibility.

The AuNPs synthesised in H_2O and D_2O have the characteristic SPR band with its maximum at 519 and 520 nm, respectively, as shown below (Figure 3.1A). The typical SPR band is responsible for the red colour of the colloidal solution, and the position of the absorbance band depends on the size of the NPs. Figure 3.1B shows the raw results of DCS experiments used to measure the apparent size distribution of NPs. As reported by the DCS software, the AuNPs synthesised in H_2O and D_2O have an apparent average

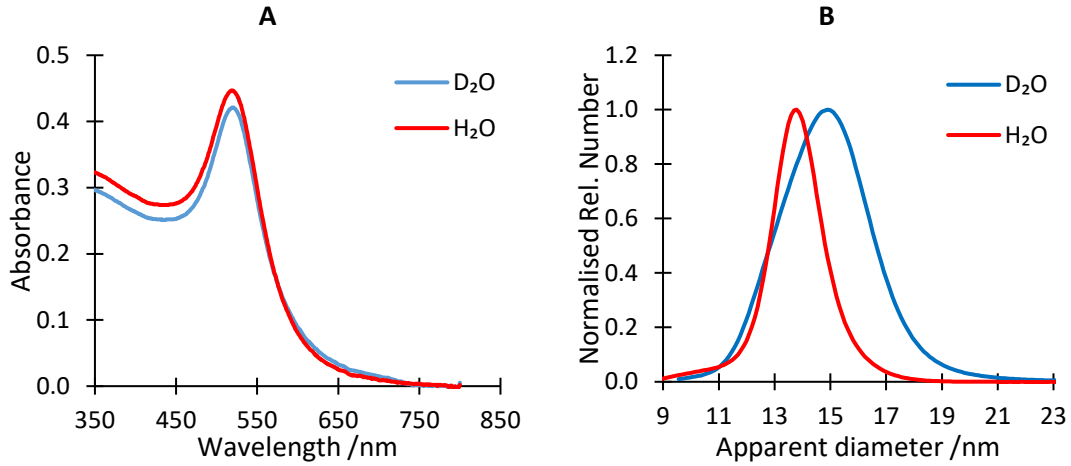

Figure 3.1 – A) UV-Vis absorbance spectra of AuNPs in H_2O and D_2O with λ_{max} at 519 and 520 nm, respectively, and, B) Differential centrifugal sedimentation result of AuNPs in H_2O and D_2O with a maximum non-corrected diameter of 13.8 and 14.9 nm, respectively.

diameter of 13.8 (± 1.0) nm and 14.9 (± 1.9) nm, respectively. The "apparent" AuNPs diameter obtained directly from DCS analysis (maxima of the distributions) results from a simplification implicit in the algorithm by which the instrument determines the NPs diameter. The DCS software works with the assumption that the density of the AuNPs is that of gold (19.3 $g.cm^{-3}$), ignoring the ligand shell. However, AuNPs are citrate stabilised, and the average density of the AuNP with the citrate shell is smaller, which results in an apparent diameter that is smaller than the real AuNPs diameter. Krpetic *et al.*[16] recently published a simple protocol to correct for the particle density in the presence of ligand shells and so it was possible to determine the real AuNPs diameter – 14.7 and 15.8 nm for AuNPs synthesised in H_2O and D_2O, respectively. Lastly, the SPR absorbance also allows the determination of the AuNPs' concentration if the AuNPs' diameter is known, as shown by Haiss *et al.*.[17] The AuNPs synthesised in H_2O and D_2O have a concentration of ~ 1.1 (± 0.2) nM.

3.2.3 Sample preparation

Due to DPBF insolubility in neat water, all experiments with DPBF were conducted in 50/50 (v/v) mixtures of EtOH and H_2O or D_2O, unless stated otherwise. This solution mixture was required due to the AuNPs' instability in neat ethanol. A DPBF stock solution (~ 0.1 mM) was prepared in EtOH (5 mL), kept stirring in the dark and used within 24

hours. The DPBF ethanolic stock solution (3 mL) was then diluted 1:1 with either Milli-Q water, D_2O or AuNPs solution (3 mL) and kept stirring in the dark for at least 60 minutes before use.

An ABDA stock solution (~ 10 mM) was prepared in DMSO because it was found to be difficult to dissolve ABDA in neat water fully. 10 µL of ABDA stock solution was then added to 1 mL of D_2O, 50/50 (v/v) EtOH/D_2O, AuNPs solution in D_2O or 50/50 (v/v) EtOH/AuNPs solution to prepare the irradiation samples with 1% (v/v) DMSO.

The ethanolic mixtures of ABDA and DPBF (EtOH/H_2O, EtOH/D_2O or EtOH/AuNPs) were left stirring for 60 minutes before use because ethanol has a higher oxygen solubility than H_2O or D_2O. Upon mixture, the resulting ethanol-H_2O/D_2O mixture is O_2 supersaturated due to a non-linearity of the solubility concentration curve.[18] It was observed that the irradiation of O_2 supersaturated DPBF solution mixtures leads to a faster photobleach of DPBF, which disappears after stirring for 60 minutes. Further details and a discussion of the effect can be found in Appendix 1, section A1.5. The other solutions were prepared and used immediately.

$^1O_2$ was detected in DPBF and ABDA solutions with different O_2 concentrations – O_2, air and N_2 saturated (O_2 depleted) solutions. ABDA solutions were prepared as O_2, air and N_2 saturated solutions, while DPBF solutions were only prepared as air and N_2 saturated solutions because DPBF bleaches during the O_2 bubbling procedure. H_2O, D_2O, EtOH or AuNPs solutions (10 mL) were bubbled individually in vials sealed with parafilm for approximately 30 minutes with O_2 or N_2 before use, to vary the O_2 concentration in solution. N_2 was used to remove (almost) all O_2 from the solvents. After the 30 minutes and while still bubbling, aliquots were taken from the 10 mL vials and used to prepare the sample in the cuvette used for the irradiation. After sample preparation, the cuvette was closed with an airtight lid with a septum; the solution was further bubbled through the septum for 30 seconds and the cuvette headspace filled with the bubbled gas to maintain the gas saturation during the experiment.

3.2.4 Irradiation setup

For the irradiation experiments, the solutions were placed into a 10 mm path-length cuvette (Starna Special Optical Glass, SOG), equipped with a magnetic stirrer bar and sealed with an airtight stopper. The solution was kept stirring before and throughout the irradiation experiment.

The irradiation was performed at 532 nm using a continuous-wave diode-pumped solid-state laser with a $1/e^2$ beam diameter of 1.85 mm (Opus 532, Laser Quantum). The laser powers used for the irradiation of DPBF and ABDA solutions were 1 and 3 W, respectively, unless stated otherwise. A cut-off filter (GG375, Schott, Germany) was used to eliminate residual light under 375 nm, which is emitted by the laser, and consequently avoid direct photodegradation of the $^1O_2$-sensor molecules. Further details can be found in Appendix 1, section A1.3. Due to the cut-off filter absorbance at 532 nm (A = 0.05), the laser power was reduced by 10%. The laser power was further reduced by reflection losses of 4.6% on the front face of the cuvette, determined from the Fresnel equations.

All samples were cooled using a fan during irradiation experiments. To better control the temperature when high irradiation powers were used (Irradiation of ABDA samples in the presence of AuNPs – 3 W), the cuvette was placed inside a three by two cm quartz container filled with room temperature water to cool more efficiently the solution. The samples were irradiated for 10 minutes, removed from the laser setup and kept stirring in the dark for 10 minutes and then the absorbance spectrum was recorded (Ocean Optics USB4000). This procedure was repeated until the sample had been irradiated for a total of 60 minutes. The increase of the solution temperature during irradiation of ABDA solutions in the presence of AuNPs and its effect on the absorbance of ABDA was investigated, see Appendix 1, section A1.4, where it is shown that the procedure described here was sufficient to avoid any distortion by heating.

Before any irradiation experiments, the solution stability was checked in the absence of irradiation to confirm the chemical stability of DPBF, ABDA and AuNPs using a UV-Vis absorbance spectrometer. This experimental control showed no spectral changes over a time interval of 60 minutes, see Appendix 3 – Figure A3. 2.

3.2.5 Data analysis - Progressive photobleach of ABDA and DPBF

The UV-Vis spectra of AuNPs and the $^1O_2$ molecular probes, DPBF and ABDA, in the presence of AuNPs are shown in Figure 3.2.

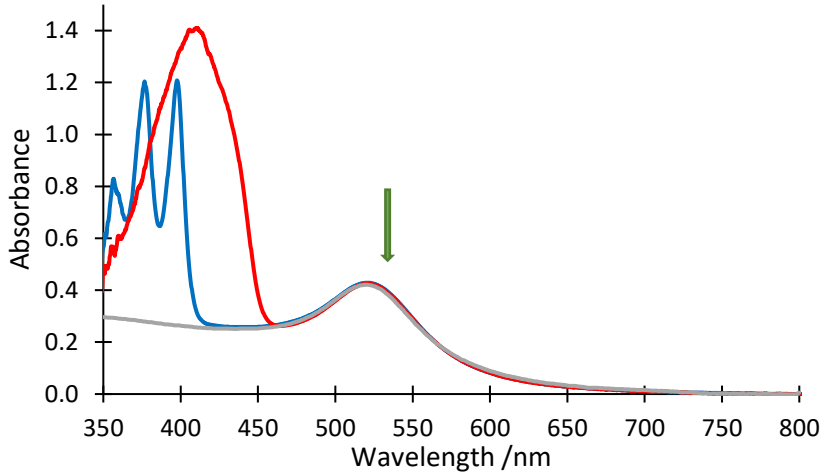

Figure 3.2 – Absorbance spectra of AuNPs in D_2O (grey line), DPBF in 50/50 (v/v) EtOH/D_2O (red line) and ABDA in D_2O (blue line) in the presence of AuNPs. The green arrow shows the irradiation wavelength (532 nm).

As shown in Chapter 2, Figure 2.1, the molecular probes do not have any absorbance at the excitation wavelength used in our experiments (532 nm). However, the AuNPs have a significant absorbance at the wavelengths where the molecular probes have strong absorbance, 410 nm for DPBF and 380 and 400 nm for ABDA. Therefore, the progressive photobleach of ABDA and DPBF due to photosensitization by AuNPs was quantified from spectra as those shown in Figure 3.2 by measuring the absorbance at the maximum of the near-UV absorbance band (A_{Probe}), averaged over a limited wavelength range (ABDA: 398 – 399 nm, DPBF: 408 – 411 nm), and subtracting both the offset and the residual absorbance of AuNPs at those wavelengths (RA_{AuNPs}). The offset was estimated by averaging over the wavelength range 750 – 800 nm and accounts for spectrometer baseline drifts. The residual absorbance of AuNPs was estimated by averaging the absorbance over a limited wavelength range (437 - 439 nm and 462 – 465 nm for ABDA and DPBF samples, respectively), and multiplying it by a correction factor (f), as demonstrated for DPBF (Equation 3.1). These wavelength ranges were chosen because they are outside of the bands of ABDA and DPBF, Figure 2.1, hence the absorbance at these wavelengths arises exclusively from the AuNPs. The correction factor

f was determined from the absorbance spectrum of AuNPs in the absence of ABDA or DPBF.

Equation 3.1

$$RA_{AuNPs(408-411\,nm)} = (A_{(462-465\,nm)} - offset)f$$

$$f = \frac{A_{AuNPs\,(408-411\,nm)} - offset}{A_{AuNPs\,(462-465\,nm)} - offset}$$

In the absence of AuNPs, the ABDA absorbance and DPBF self-photobleach was quantified by measuring the molecular probe's absorbance at the maximum of the near-UV absorbance band (A_{Probe}), averaged over a limited wavelength range (ABDA: 398 – 399 nm, DPBF: 408 – 411 nm) and subtracting the base line absorbance averaged over the wavelength range 750 – 800 nm for both molecular probes. The strategies described above were used to improve the signal-to-noise ratio of the measurement, to correct for any potential baseline offsets and correct for the residual AuNPs absorbance.

The concentrations of DPBF and ABDA were chosen to give an absorbance near 1 unless stated otherwise, but due to the small amounts used and the solubility issues, the exact absorbance differed from this in different samples. Therefore, for comparison charts, the ABDA results were normalised to 1 at zero irradiation time, i.e. A/A (0 min), and plotted as a function of time, whereas the DPBF results were normalised to 1 at 20 minutes irradiation time, i.e. A/A (20 min), because the DPBF self-photobleach during the first twenty minutes of irradiation is highly irreproducible (see section 3.3.1.1), as reported previously,[9]. Due to this phenomenon, only data from the second, reproducible phase, starting after 20 minutes of irradiation, will be used for quantitative comparisons.

The amount of ABDA photobleaching per minute in the presence or absence of AuNPs presented in the bar charts below shows the gradient of the time-dependent normalised absorbance change in the entire irradiation period, 60 minutes, i.e. $<\Delta(A/A(0\text{ min}))/\Delta t>_{0\text{-}60}$. The amount of DPBF photobleaching per minute in the presence or absence of AuNPs presented in the bar charts below shows the gradient of the time-dependent normalised absorbance change in the irradiation time window 20 – 60 minutes, i.e. $<\Delta(A/A(20\text{ min}))/\Delta t>_{20\text{-}60}$, due to the same reasons as described above.

The error bars presented in the graphs showing the normalised absorbance change of DPBF or ABDA correspond to the standard error of the results, obtained from the standard deviation of several repeat experiments, divided by the square root of the number of repeat experiments.

3.2.6 Shading by gold nanoparticles

The irradiation results showed that DPBF self-photobleaches in the absence of AuNPs under our CW-irradiation, and a similar observation has been reported by Chadwick *et al.* under the same irradiation conditions.[9] Our irradiation results showed that the DPBF self-photobleach effect increases linearly with the irradiation power (see Figure 3.8B) and that the DPBF photobleach induced by AuNPs is comparable to the DPBF self-photobleach in the absence of AuNPs. Therefore, careful considerations were necessary to analyse the DPBF photobleach results in the presence of AuNPs. The solutions containing AuNPs have a strong absorbance at 532 nm (the wavelength of the laser light used to irradiate the samples), which "shades" the samples significantly, i.e. it reduces the average laser power causing the DPBF self-photobleach. Therefore, it is not possible to simply subtract the DPBF self-photobleach measured in the absence of AuNPs from the DPBF photobleach in the presence of AuNPs. It was first necessary to determine how the laser power (P) varies along the beam path (x), using Equation 3.2, where LP represents the incident laser power, corrected for the losses discussed above (section 3.2.4), d is the total path length, and A denotes the absorbance of the sample at 532 nm.

Equation 3.2

$$P(x) = LP\ 10^{\frac{-Ax}{d}}$$

As shown in appendix A3, section A3.1, Equation 3.2 can be integrated along the beam path yielding the average laser power (<P>) along the beam path (Equation 3.3).

Equation 3.3

$$<\mathrm{P}> = LP\ \frac{(1 - 10^{-A})}{A \ln 10}$$

The average laser power determined with this equation was then used to determine the DPBF self-photobleach caused by the reduced laser power and subtract it from the DPBF photobleach in the presence of AuNPs, allowing the determination of the effective DPBF photobleach caused by the AuNPs. This correction was done for each sample individually because the absorbance of AuNPs varied slightly from sample to sample. Also, note that this correction only needed to be applied to DPBF samples because DPBF self-photobleaches under our CW-irradiation conditions in the absence of AuNPs, whereas ABDA solutions in the absence of AuNPs did not photobleach even when irradiated with higher powers (3 W).

3.3 DPBF self-photobleach

As mentioned at the beginning of the previous section 3.2.6, our irradiation experiments showed that DPBF photobleaches under our CW-irradiation conditions. A similar observation has been reported by Chadwick *et al.* under the same irradiation conditions.[9] Here, we thoroughly investigate this DPBF self-photobleach in the absence of AuNPs.

3.3.1 Experimental observations

Figure 3.3 shows the absorbance change of DPBF upon CW-irradiation at 532 nm with a laser power of 1 W, in a 50/50 (v/v) air-saturated EtOH/H_2O solution.

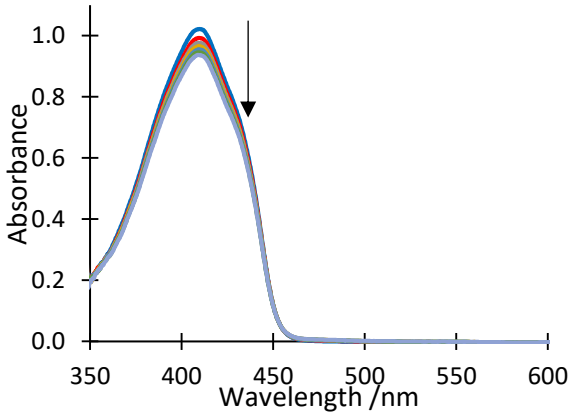

Figure 3.3 - Photobleach of DPBF absorbance upon CW-irradiation at 532 nm, 1 W, in 50/50 EtOH/H_2O solution (air-saturated). Absorbance spectra of DPBF were taken with 10 minutes intervals to a maximum irradiation period of 60 minutes. The arrow indicates the direction of change.

There is a clear decrease of the DPBF absorbance as the irradiation progresses. The DPBF absorbance decreased by ~ 9% after 60 minutes of irradiation. It is important to note that in the absence of laser light, the DPBF absorbance remains stable up to 24 hours (see Appendix 3 - Figure A3. 3) and, as shown in Appendix 2- Figure A2. 1, the absorbance of DPBF remained stable when the samples were irradiated over 50 minutes with a laser power of 0.14 mW.

3.3.1.1 Two photobleaching phases

Figure 3.4 shows the variation of the normalised DPBF absorbance at 410 nm over time for seven independent experiments under the same experimental conditions (CW-irradiation at 532 nm, 1 W, 50/50 (v/v) air-saturated EtOH/H_2O). The solid line shows the average of all seven experiments.

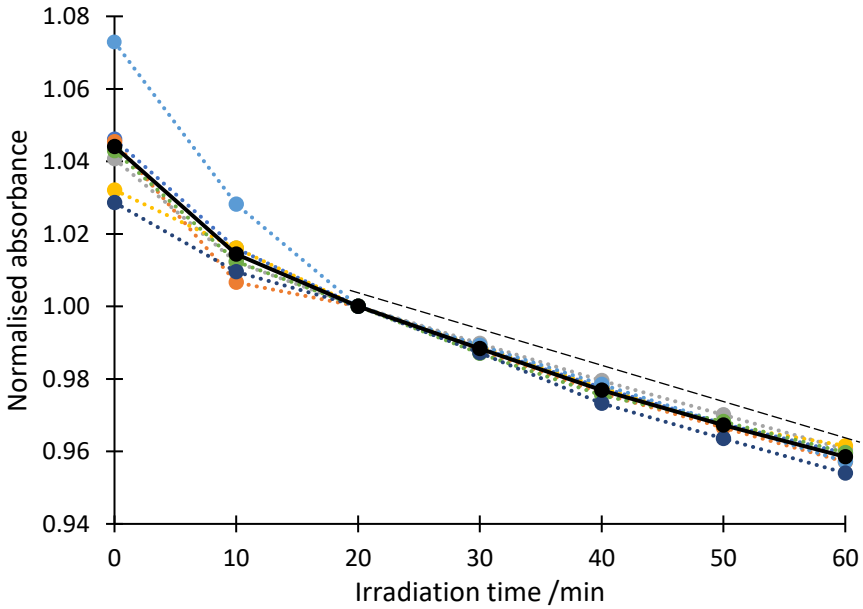

Figure 3.4 – Variation of the DPBF absorbance at 410 nm, normalised at 20 min, upon CW-irradiation at 532 nm, 1 W, 50/50 (v/v) EtOH/H_2O; shown are seven measurements (dotted lines) as well as the average of the seven experiments (thick solid black line). The absorbance of DPBF was normalised at 20 minutes due to the irreproducible variation of DPBF absorbance during the initial irradiation period. The dashed line highlights the linearity of the second, reproducible, phase present after 20 minutes of irradiation.

The photobleach of DPBF upon CW-irradiation at 532 nm appears to have two different photobleaching phases; an initial, highly irreproducible phase, present during

the first 20 minutes of irradiation and a second, reproducible phase, present after 20 minutes of irradiation that is linear with time on the time scale of the experiments, as highlighted in Figure 3.4. Because of the initial irreproducible phase observed experimentally, the absorbance of DPBF was normalised for the absorbance at a time of 20 minutes, which separates the initial phase from the second one, which is much more reproducible. Chadwick *et al.*[9] reported a similar effect. The authors observed that the photobleaching effect had two different phases, a rapid phase dependent on the presence of O_2 in the first 20 minutes of irradiation, and a linear slower phase independent of O_2, between 20 and 60 minutes. No explanation was given for the DPBF photobleach in the absence of PS, however.

3.3.1.2 Solvent effects

The DPBF self-photobleaching was investigated for different EtOH/H_2O ratios. Decreasing the ethanol content from 50% to 40% made the DPBF solution unstable even in the dark due to DPBF insolubility in H_2O, see Appendix 3 – Figure A3. 4. Increasing the ethanol content from 50% to 60% does not appear to affect the photobleach observed (Appendix 3 – Figure A3. 5). Chadwick *et al.* reported a similar observation upon comparing the irradiation of 1.2 mL in 50/50 and 80/20 (v/v) EtOH/H_2O mixtures.[9] To better compare our irradiation experiments with the results presented by Chadwick *et al.* (in 1.2 mL), some experiments were also conducted with 1.2 mL (Appendix 3 – Figure A3. 6A), which reproduced the effect reported by Chadwick *et al.*.

The DPBF self-photobleach effect was also investigated upon CW-irradiation of ethanolic mixtures with D_2O. Figure A3. 8 in Appendix 3 shows that the irradiation of DPBF in EtOH/D_2O also showed an initial, highly irreproducible phase present during the first 20 minutes of irradiation, and the second, reproducible phase, present after 20 minutes of irradiation. Figure 3.5 shows the time-dependent photobleaching of DPBF absorbance at 410 nm of EtOH/H_2O and EtOH/D_2O solutions, under the same irradiation conditions (CW-irradiation at 532 nm, 1 W). Replacing H_2O with D_2O resulted in an increase of the DPBF self-photobleach upon irradiation in both photobleaching phases. A quantitative analysis of the second DPBF self-photobleach phase showed that the irradiation of DPBF

solution in 50/50 (v/v) EtOH/D_2O increased the DPBF self-photobleach by ~ 60% when compared to the EtOH/H_2O solution, see Figure 3.5 and Figure 3.6.

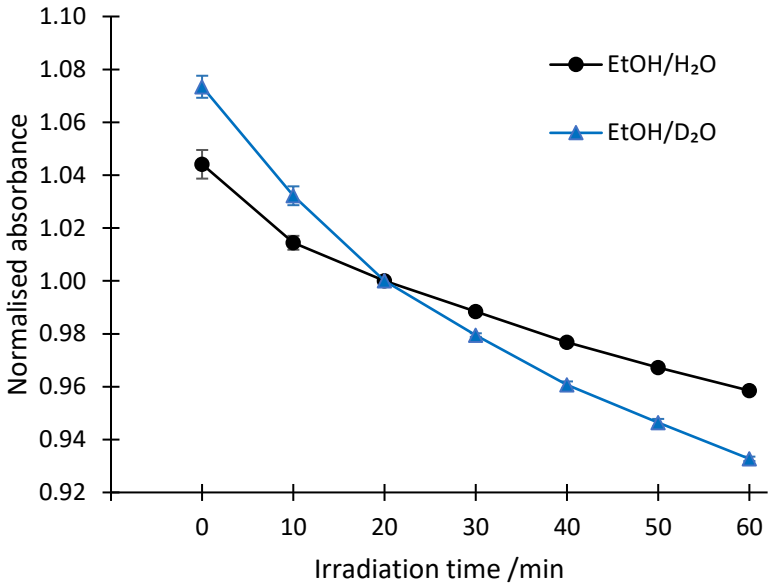

Figure 3.5 –Variation of the DPBF absorbance at 410 nm, normalised at 20 min, in air-saturated solutions in 50/50 (v/v) EtOH/H_2O (average of seven experiments) and 50/50 (v/v) EtOH/D_2O (average of six experiments) upon CW-irradiation at 532 nm, 1 W. The error bars show the standard error. The error bars are smaller than the symbol size for the points after 20 minutes.

3.3.1.3 O_2 depleted solutions

The DPBF self-photobleach was also investigated in O_2 depleted (N_2-saturated) solution mixtures. Decreasing the O_2 concentration in the solution mixtures (EtOH/H_2O and EtOH/D_2O) resulted in a decrease of the DPBF self-photobleach in both photobleaching phases when compared to air-saturated conditions (see Appendix 3, Figure A3. 14).

Figure 3.6 shows the gradients of the time-dependent DPBF photobleaching of EtOH/H_2O and EtOH/D_2O solution mixtures in the irradiation time interval 20 – 60 minutes under different gas saturation (air and N_2), upon CW-irradiation at 532 nm, 1 W. Removing the O_2 from DPBF solution mixtures reduced the DPBF self-photobleach by ~60% and 30% for the EtOH/H_2O and EtOH/D_2O solutions observed in the 2nd photobleaching phase, respectively.

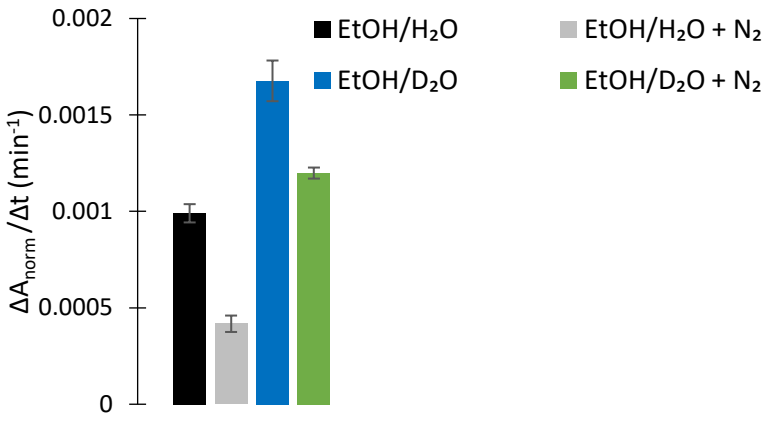

Figure 3.6 – Bar chart showing the gradient of the normalised DPBF absorbance decay per minute (measured at 410 nm) in the irradiation time interval 20 – 60 minutes in air and N_2 saturated solutions in 60/40 (v/v) EtOH/H_2O (average of five and three experiments) and air and N_2 saturated solutions in 50/50 (v/v) EtOH/D_2O (average of six and two experiments, respectively) upon CW-irradiation at 532 nm, 1 W. The error bars show the standard error of the gradient of the normalised DPBF absorbance decay per minute.

The oxygen dependence observed in our irradiation experiments is in disagreement with the results reported by Chadwick *et al.*.[9] The authors reported that the solutions bubbled with N_2 showed a reduction of the irreproducible phase (1st photobleaching phase), whereas the photobleach slope in the second phase was independent of purging. In contrast, in our irradiation experiments, removing O_2 from the solution decreased the overall DPBF self-photobleach in both phases. It is important to note that the setup used by Chadwick *et al.* for N_2 bubbling did not use a cuvette sealed with an airtight stopper and the solutions were bubbled for a shorter period (10 minutes), suggesting that Chadwick's samples may have rapidly equilibrated with air again. Therefore, it is reasonable to suggest that our N_2 bubbling protocol reduces the O_2 concentration in solution more efficiently than the one reported by Chadwick *et al.*, which resulted in a reduction of the DPBF self-photobleach. Nonetheless, our bubbling procedure cannot guarantee the complete removal of O_2 from the solution mixtures, potentially explaining the residual DPBF self-photobleach observed upon irradiation of "N_2-saturated" solution mixtures (see section 3.3.2.2 below).

3.3.1.4 DPBF concentration dependence

The DPBF self-photobleach was also investigated by irradiating DPBF solutions with different DPBF concentrations. Figure 3.7 shows the variation of the normalised

DPBF absorbance at 410 nm in the absence of AuNPs for different initial concentrations of DPBF (17, 34 and 49 µM) upon CW-irradiation at 532 nm with an irradiation power of 1 W in 60/40 (v/v) EtOH/H_2O solutions. Varying the concentration of DPBF in solution, ranging from 17 to 49 µM (0.4 to 1.2 absorbance), did not affect the normalised DPBF absorbance bleach (at 410 nm) present in the second, reproducible, linear phase observed during CW-irradiation. Additionally, the irradiation results seem to suggest that the irradiation of DPBF solutions with higher DPBF concentrations resulted in a higher DPBF self-photobleach during the irreproducible phase, present during the first twenty minutes of irradiation. An interpretation of this effect will be discussed below (section 3.3.2.3).

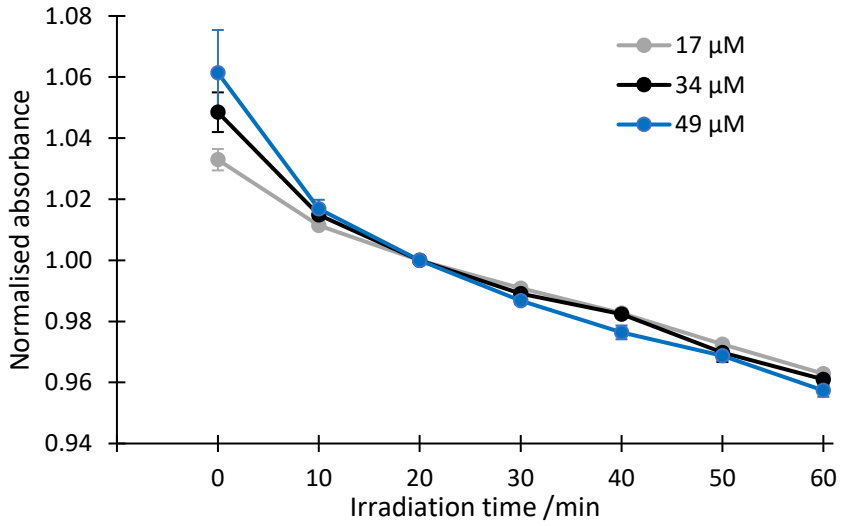

Figure 3.7 - Variation of the DPBF absorbance at 410 nm, normalised at 20 min, upon CW-irradiation at 532 nm, 1 W, 60/40 (v/v) EtOH/H_2O with different DPBF concentrations (17, 34 and 49 µM); shown is the average of three measurements for each DPBF concentration tested. Error bars show the standard error. Note that the error bars are smaller than the symbol size for the points after 20 minutes.

3.3.1.5 Power dependence of DPBF self-photobleach

The DPBF photobleaching effect was also investigated upon irradiation with different irradiation powers. Figure 3.8A shows the variation of the normalised absorbance of DPBF at 410 nm over time for several measurements with three different irradiation powers, 0.5 W, 1 W and 2 W. All solutions were prepared in an air-saturated 60/40 (v/v) EtOH/H_2O mixture. Increasing the laser power used to irradiate the DPBF solutions increased the gradient of the photobleach in both phases.

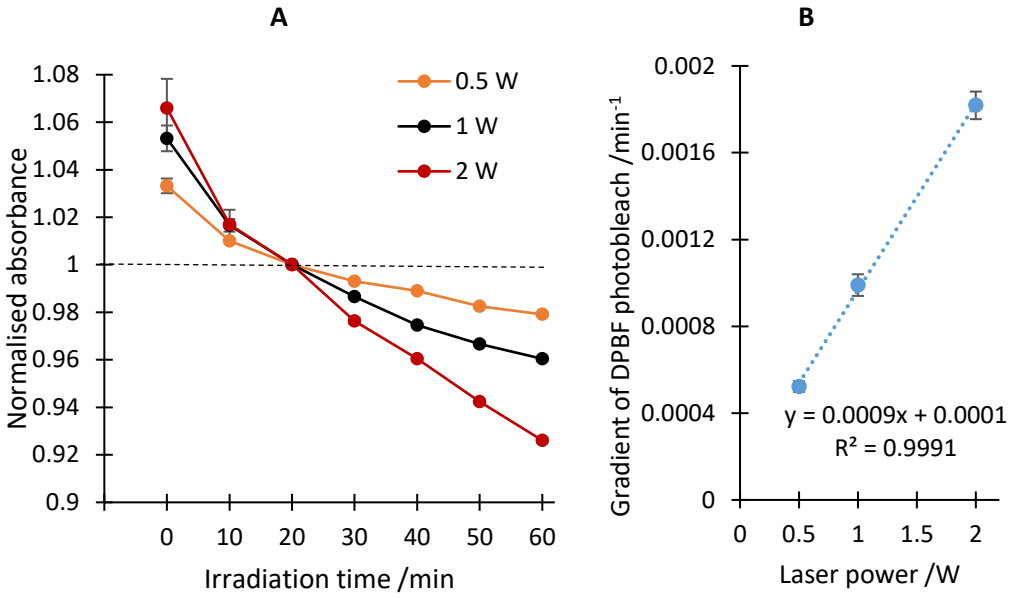

Figure 3.8 – A) Variation of the DPBF absorbance at 410 nm, normalised at 20 min, upon CW-irradiation at 532 nm with different irradiation powers, 0.5 W, 1 W and 2 W, in 60/40 (v/v) EtOH/H_2O solution, air-saturated (average of three, five and three experiments, respectively). B) Linear fit of the gradient of the DPBF absorbance bleach in the irradiation time interval 20-60 min (obtained from linear fits of the individual measurements) as a function of the laser power. Error bars show the standard error. Note that in A) the error bars are smaller than the symbol size for the points after 20 minutes.

Figure 3.8B shows the gradient of the DPBF self-photobleach during the reproducible phase after 20 minutes as a function of the laser power. As shown by the linear fit, a linear dependence of the DPBF photobleach per minute on the irradiation power was observed. Chadwick *et al.* had also studied the time-dependent photobleaching of DPBF at different irradiation powers, ranging from 0.03 to 1 W.[9] At first glance, the results presented by the authors (Appendix 3 – Figure A3. 7) seem to disagree with the results shown above. The authors suggested that the amplitude of the initial rapid phase increases with an increase in the irradiation power, but the slope of the slower linear phase was reported to be roughly independent of the laser power within the error.[9] However, careful consideration of the curves presented in the publication (see Appendix 3 – Figure A3. 7) shows a smaller slope when 500 mW was used to irradiate the DPBF solution, as observed in our experiments. Nonetheless, it is important to point out that their irradiation results with 100 mW show a similar gradient of the DPBF self-photobleach in the second self-photobleaching phase when compared to the 1 W results. An interpretation of our irradiation results in comparison with Chadwick's will be discussed below (section 3.3.2.2 and 3.3.2.3).

3.3.2 Mechanism

DPBF has been reported to self-photobleach due to a reaction with O_2 when excited at 404 nm.[19] The authors reported that, at low enough DPBF concentrations (similar to the concentration used in our experiments), 88% of the photoexcited ^{1}DPBF* molecules are regenerated to the ground state by emission of a photon (fluorescence), and the remaining 12% photobleach due to a reaction with O_2 (photooxidation). The authors further suggest that, for the DPBF concentration [~ 4 x 10^{-5} M] that we used in our irradiation solutions, the photooxidation of DPBF follows two pathways with similar probabilities; A) a reaction between ^{1}DPBF* with ground-state O_2 and B) the generation of ^{3}DPBF via intersystem crossing, which is quenched by O_2 to generate $^1O_2$. The generated $^1O_2$ is either quenched by the solvent or readily reacts with the regenerated groundstate DPBF in the solvent cage, i.e. there is no "free" diffusion of $^1O_2$ until it randomly reacts with another DPBF. Similar conclusions were reported in an independent study.[20]

$$DPBF \overset{h\upsilon}{\rightarrow} {}^1DPBF^* \overset{ISC}{\longrightarrow} {}^3DPBF \overset{O_2}{\rightarrow} S\text{-}O_2$$

Here, we suggest that the irradiation of DPBF solutions at 532 nm excites DPBF to a higher electronic state (^{1}DPBF*) which, in the presence of O_2, causes its self-photobleach, as justified below.

3.3.2.1 Residual absorbance at 532 nm

In contrast to the literature data mentioned above, where irradiation of DPBF was undertaken at the maximum of its absorbance band, in our experiments, we irradiated DPBF solutions at 532 nm, away from the DPBF absorbance band (see Figure 3.3). However, a closer look at the DPBF absorbance spectrum suggests that DPBF has a residual absorbance at 532 nm that is smaller than 1 mOD (see Appendix 3 – Figure A3. 9A) whereas, for ABDA, no such residual absorbance was observed (see Appendix 3 – Figure A3. 9B).

This residual absorbance strongly suggests that DPBF is being excited by our CW-irradiation at 532 nm, causing its self-sensitised photooxidation. Taking into consideration

the photooxidation yield (12%)[19] mentioned above, and a DPBF absorbance variation of typically 0.04 observed during the second, reproducible, linear phase in our irradiation experiments (between 20 to 60 minutes of irradiation, see Figure 3.4), a quantitative estimate showed that a residual absorbance as small as 6 x 10^{-4} mOD is enough to yield the DPBF self-photobleach effect observed in our irradiation experiments. Thus, an even higher self-photobleach than actually observed would be in agreement with the residual absorbance shown in Figure A3. 9A; the effect may be less than predicted in our estimate because the absorbance measurement is not highly accurate, the photooxidation yield was not measured in EtOH/H_2O but in benzene and/or the residual absorbance band may be due to dimerisation of DPBF (see below).

3.3.2.2 Suggested mechanism vs. experimental observations

- *Linear power dependence*

The proposed mechanism explains the linear power dependence of the DPBF self-photobleach shown in Figure 3.8B. Decreasing the laser power, maintaining the same DPBF concentration, reduces the absorbed laser power by DPBF molecules. Hence, it reduces the amount of DPBF self-photobleached molecules proportionally, as observed in our irradiation experiments (Figure 3.8).

- *Concentration independence*

Figure 3.7 shows that the DPBF self-photobleach is independent of the concentration of DPBF in solution. According to the mechanism described above, the reaction of ^{1}DPBF* with ground-state O_2 (path A) should be independent of the DPBF concentration, since it is a first-order reaction. In contrast, the $^1O_2$ mediated DPBF oxidation (path B) would not be expected to be independent of DPBF concentration, that is, the irradiation of a DPBF solution with a higher DPBF concentration has a higher sensitivity (Φ_S) to $^1O_2$, as shown in chapter 2, and, at the same time, generates more $^1O_2$. Therefore, the relative amount of DPBF photobleached should increase with an increase of the DPBF concentration. However, since the photobleaching process is mostly a geminate reaction, where the $^1O_2$ reacts with DPBF that generated it, the reaction is effectively a first-order reaction, i.e. also independent of the DPBF concentration.

- *Solvent effect (H_2O vs D_2O)*

The mechanism proposed by Olmsted *et al.* also includes a pathway where the photoexcited ^{1}DPBF* generates $^1O_2$, via ISC to ^{3}DPBF (path B).[19] This mechanism pathway explains the increased DPBF self-photobleach observed upon irradiation of 50/50 (v/v) EtOH/D_2O solution mixtures when compared to 50/50 (v/v) EtOH/H_2O (Figure 3.5). As summarised in chapter 2, Table 2.2, the intrinsic lifetime of $^1O_2$ in solution depends strongly on the solvent.[21–23] Replacing H_2O by D_2O, i.e. using a solvent where $^1O_2$ is longer lived, increases the lifetime of the generated $^1O_2$ in solution, making it more likely that it reacts with the nearby DPBF, hence inducing a larger DPBF self-photobleach.

- *O_2 depletion*

Both pathways outlined above (path A and B) require the presence of O_2 for the DPBF self-photobleach to occur. However, the mechanism proposed above suggests that the photo-oxidation pathway B is independent of the O_2 concentration, down to very low O_2 concentrations, since the quenching of ^{3}DPBF by O_2 is much faster than the intrinsic ^{3}DPBF decay•,[24]. Therefore, a minor depletion of oxygen would not affect this contribution to the DPBF self-photobleach (as observed by Chadwick *et al.*, see section 3.3.1.3) down to a small O_2 concentration, whereas at a very low O_2 concentration, one would still expect a significant reduction of the bleaching. Therefore, the quite different reduction of DPBF self-photobleach in the EtOH/H_2O and EtOH/D_2O solution mixtures presented in section 3.3.1.3 - Figure 3.6, most likely occurred due to a different residual O_2 concentration in the solution mixtures. It is important to highlight that the N_2 bubbling experiments compiled in Figure 3.6 were performed on different days, potentially with different N_2 flow rates, i.e. all data points obtained for the H_2O + N_2 experiment were obtained on the same day, and the D_2O + N_2 data were obtained on a different day. Therefore, it is reasonable to suggest that the bubbling efficiency could have been different in both data sets, which might explain the variation of the O_2 effect.

• - The intrinsic ^{3}DPBF decay rate constant (1.85 x 10^3 s^{-1}) was determined in benzene. However, one would not expect a variation of several orders of magnitude variation in EtOH/H_2O or EtOH/D_2O. [24]

3.3.2.3 DPBF dimers

In the previous sections 3.3.2.1 and 3.3.2.2, we interpreted and compared our experimental results with the proposed mechanism described in 3.3.2, which explained the 2nd linear, reproducible phase of DPBF self-photobleach in the presence of O_2. Here, we will suggest an explanation for the 1st irreproducible phase observed in our experimental results.

DPBF is insoluble in water, barely soluble in 50/50 (v/v) EtOH/H_2O and, as shown in the appendix 3 Figure A3. 4, decreasing the ethanol content from 50% to 40% made the DPBF solution unstable even in the dark. Therefore, it seems highly likely that for the solvent mixtures commonly used in our irradiation experiments, i.e. 50/50 or 60/40 (v/v) EtOH/H_2O or EtOH/D_2O, some dimerisation or residual aggregation of DPBF could occur. A similar suggestion has been reported in the literature.[25] DPBF dimers are more likely to have a residual absorbance at longer wavelengths than monomers, hence it is more likely that interaction with light at 532 nm could occur. The presence of DPBF dimers in solution could explain why the first photobleaching phase is so irreproducible, namely due to an irreproducible extent of dimerisation/residual aggregation. Therefore, we here suggest that the first irradiation phase mentioned in section 3.3.1.1 results from the self-photobleach of both DPBF monomers and dimers simultaneously. After photolysis of all DPBF dimers, only the DPBF monomer photobleach effect remains, causing the second, more reproducible, photobleaching phase.

The existence of DPBF dimers in solutions can also explain why the initial photobleaching phase varies with the variation of the initial DPBF concentration, as shown in Figure 3.7. Increasing the DPBF concentration in solution increases the dimer concentration more than proportionally to the monomer concentration, which upon irradiation results in a higher initial DPBF self-photobleach when looking at the normalised absorbance change.

Likewise, the presence of DPBF dimers in solution could explain the power dependence interpretation presented by Chadwick *et al.* (see section 3.3.1.5). The authors reported that the amplitude of the initial rapid phase increased with an increase in the irradiation power, but the slope of the slower linear phase was roughly independent of the laser power down to 100 mW. From another point of view, we suggest

that as the laser power decreases, the photodegradation of DPBF dimers becomes slower and extends in time, resulting in a constant combination of both DPBF self-photobleach effects (monomer plus dimer) at low enough powers. In comparison, as observed in our irradiation experiments, increasing the laser power from 1 W to 2 W seems to result in a photobleach of all DPBF dimers already during the first ten minutes of irradiation, and a linear DPBF self-photobleach was observed for the remaining irradiation period (50 minutes), see Figure 3.8A.

In principle, the dimmer formation could be investigated by observing the dependence of absorbance and/or fluorescence spectrum on the DPBF concentration. However, given the very small residual absorbance at 532 nm required to cause the effect (6×10^{-4} mOD, see page 68), this was not possible.

3.3.2.4 Summary

It was shown that air-saturated DPBF solutions in EtOH/H_2O or EtOH/D_2O in the absence of AuNPs photobleach under our CW-irradiation conditions. It was also observed that DPBF solutions are stable while in the dark, which showed that light irradiation is indeed necessary for the photobleaching process to occur. The experimental results suggest that the DPBF self-photobleach effect occurs due to direct excitation of DPBF because of a residual absorbance at 532 nm, following the self-photooxidation mechanism reported for DPBF in the presence of O_2.[19] The photobleaching of DPBF under our irradiation conditions has two phases, an initial highly irreproducible phase and a reproducible phase that is linear on the time scale of these experiments. Here, we suggest that the 1st DPBF photobleaching phase results from the cumulative photobleach of both DPBF monomers and dimers. Upon photolysis of all DPBF dimers, the DPBF self-photobleach becomes linear in the timescale of our irradiation experiments.

Overall, a more thorough study of the DPBF self-photobleach effect has been presented, which has allowed more accurate conclusions, including a proposal for the mechanism, when compared to the previous report on this topic (Chadwick *et al.*)[9].

Most importantly, a linear power dependence of the DPBF self-photobleaching was observed, which will be important when accounting for the DPBF self-photobleach for analysing data obtained in the presence of AuNPs.

3.4 Singlet oxygen photogeneration by irradiation of gold nanoparticles

Here, we will show that 15 - 16 nm citrate-stabilised AuNPs can indeed generate $^1O_2$ when excited at their SPR with green CW laser light at 532 nm. The $^1O_2$ generation yield will be investigated by measuring the photoinduced bleach of the chemical traps characterised in chapter 2, ABDA and DPBF.

3.4.1 Photogeneration of $^1O_2$ by irradiation of AuNPs detected by DPBF

Figure 3.9 shows the UV-Vis spectra of DPBF in solution with 15 nm AuNPs [~ 1.1 (± 0.2) nM] upon CW-irradiation at 532 nm, with a laser power of 1 W, in a 50/50 (v/v) air-saturated EtOH/H_2O solution. In the presence of AuNPs, there is a clear decrease in the DPBF absorbance as the irradiation progresses. Also, the irradiation does not affect

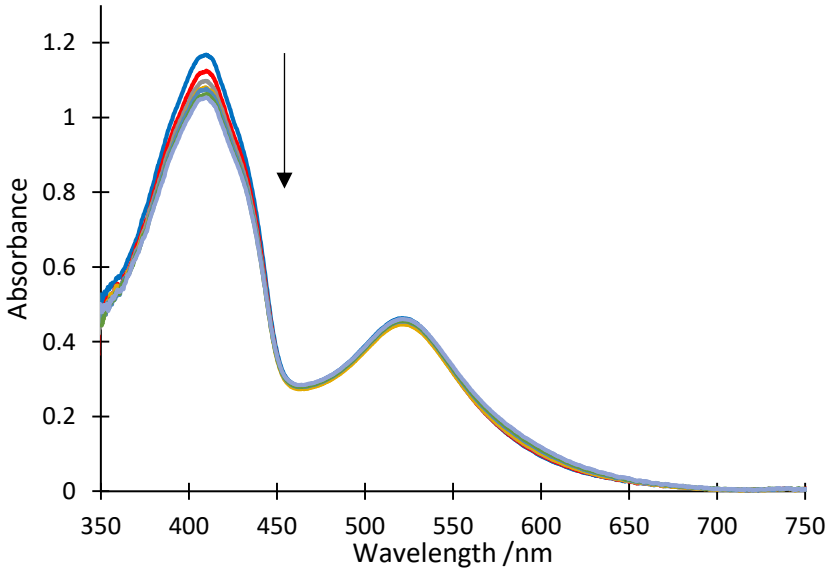

Figure 3.9 – Photobleach of DPBF absorbance upon CW-irradiation at 532 nm, 1 W in 50/50 (v/v) EtOH/H_2O (air-saturated) in the presence of 15 nm AuNPs. Absorbance spectra were taken with 10 minutes intervals to a maximum irradiation period of 60 minutes. The arrow indicates the direction of change.

the AuNPs - no significant variation of the characteristic SPR band of AuNPs absorbance at 519 nm was observed upon irradiation. The absorbance spectrum of the solution mixture of DPBF and AuNPs is the sum of the two individual spectra – see Appendix 3, Figure A3. 16. Also, in the absence of laser irradiation, the absorbance of the solution mixture of DPBF and AuNPs remains stable (see Appendix 3 – Figure A3. 2A).

Figure 3.10 shows the time dependence of DPBF photobleaching in the absence of AuNPs and in the presence of 15 - 16 nm AuNPs upon CW-irradiation at 532 nm, with a laser power of 1 W in 50/50 (v/v) EtOH/H_2O and 50/50 (v/v) EtOH/D_2O air-saturated solution. The presence of AuNPs increased the DPBF photobleach effect in both solvent conditions in comparison to the irradiation of DPBF solutions in the absence of AuNPs. Note that the DPBF photobleach effect in the presence of AuNPs also shows the two characteristic phases of DPBF photobleaching; an initial, irreproducible, phase present during the first twenty minutes of irradiation and a second, linear and reproducible, phase present during the remaining irradiation period (see Appendix 3 – Figure A3. 10), similar to DPBF photobleaching in the absence of AuNPs.

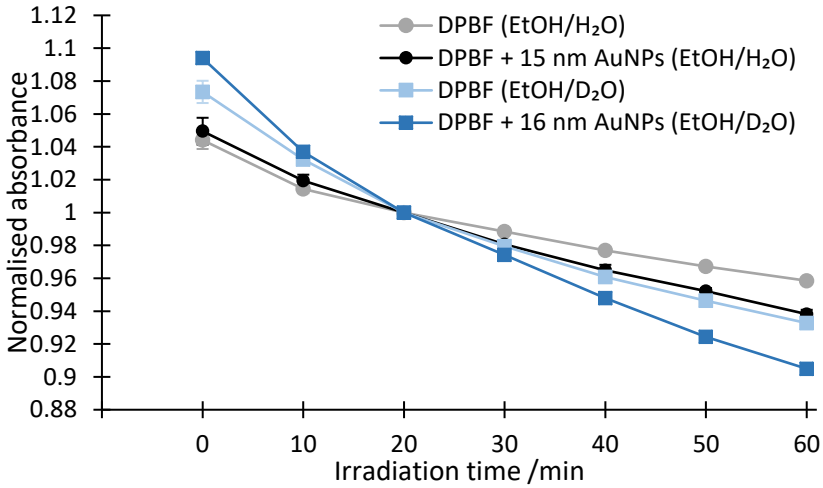

Figure 3.10 – Variation of the DPBF absorbance at 410 nm, normalised at 20 min, for air-saturated solutions in 50/50 (v/v) EtOH/H_2O and 50/50 (v/v) EtOH/D_2O in the presence of 15 and 16 nm AuNPs (black solid line with circles – average of five experiments, and dark blue solid line with squares – average of seven experiments, respectively) and in the absence of AuNPs (grey solid line with circles – average of seven experiments, and light blue solid line with squares – average of six experiments, respectively). Shown is the variation of the DPBF absorbance after subtraction of the residual AuNPs absorbance at 410 nm, as described in 3.2.5. The error bars show the standard error. Note that the error bars are smaller than the symbol size for the points after 20 minutes.

The decrease of the normalised absorbance observed in the second phase increased by ~50 and ~40%, in comparison to the photobleaching of DPBF by itself, for

the two solvent conditions used, air-saturated solution 50/50 (v/v) EtOH/H_2O and 50/50 (v/v) EtOH/D_2O, respectively. An increase in the DPBF photobleach effect caused by the irradiation of AuNPs has also been observed and reported by Chadwick *et al.* in 50/50 (v/v) EtOH/H_2O solution mixtures.[9] The authors reported a 100% increase of the DPBF photobleach when air-saturated 50/50 (v/v) EtOH/H_2O solutions containing 15 nm AuNPs were irradiated when compared to the DPBF self-photobleach in the absence of AuNPs.[9] However, the authors irradiated the solution mixture immediately after sample preparation and, as demonstrated in Appendix 1 – section A1.5, the DPBF photobleach is affected by the initial O_2 supersaturation. Therefore, it is likely that the O_2 concentration in the authors' samples was not well equilibrated, unlike in our experiments, which were conducted after O_2 equilibration, which explains the slight quantitative discrepancy between the data sets.

It is also essential to remember that the significant self-photobleach of DPBF upon CW-irradiation in the absence of AuNPs depends on the laser power (Figure 3.8B). Thus, it is necessary to take into consideration that the solutions containing AuNPs absorb the irradiation light, which reduces the laser power passing through the sample, hence reducing the DPBF self-photobleaching effect. Therefore, for accurate quantification of the DPBF photobleach caused exclusively by the AuNPs, it was first necessary to determine the DPBF self-photobleach caused by the effective laser power, reduced due to the shading by AuNPs (see section 3.2.6), and then subtract this photobleach from the DPBF photobleach in the presence of AuNPs (see section 3.2.5). Figure 3.11 shows an example of the shading correction applied to the DPBF self-photobleach and the determination of the DPBF photobleach caused exclusively by the AuNPs. This correction was done for each sample individually because the absorbance of AuNPs varied slightly from sample to sample. Most importantly, this shows that the effect caused by the AuNPs is larger than the effect suggested by the raw data of Figure 3.10.

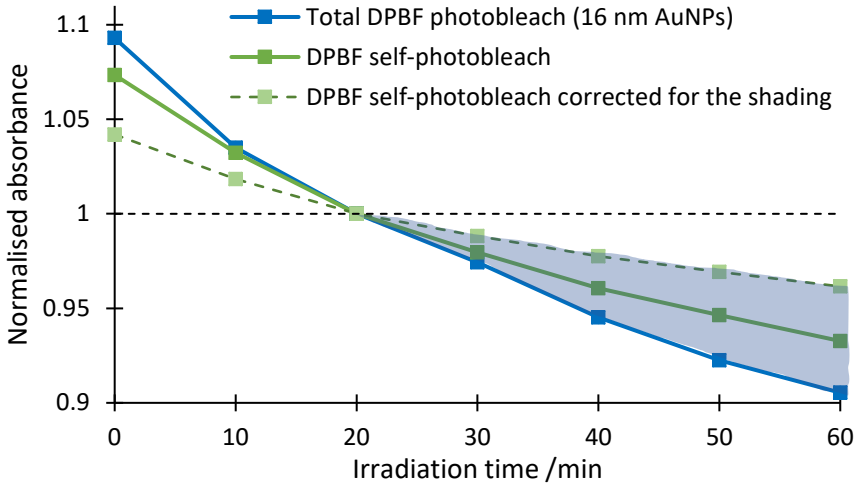

Figure 3.11 – Example of the variation of the normalised DPBF absorbance at 410 nm in air-saturated solutions in 50/50 (v/v) EtOH/D_2O in the absence (green solid lines) and presence of 16 nm AuNPs (blue solid line). The DPBF solution in the presence of AuNPs has an absorbance of 0.54 at 532 nm. The green dashed line shows the variation of the normalised DPBF absorbance (410 nm) after the shading correction (see section 3.2.6) and the shaded area shows the DPBF photobleach caused exclusively due to the irradiation of AuNPs.

Figure 3.12 shows the gradients of the variation of the normalised DPBF absorbance bleach in air-saturated 50/50 (v/v) ethanolic solution with H_2O or D_2O which is caused by the irradiation of 15 – 16 nm AuNPs, after subtracting the shading-corrected self-photobleaching of DPBF. The irradiation of AuNPs solution in the presence of DPBF in 50/50 (v/v) EtOH/D_2O resulted in a ~ 60% higher DPBF photobleach when compared to EtOH/H_2O. However, it is important to highlight that, on average, the absorbance at 532 nm in the 50/50 (v/v) EtOH/D_2O solutions was ~ 20% higher when compared to the EtOH/H_2O samples, hence the solution mixture with D_2O absorbed more photons than the H_2O solution, which resulted in a higher amount of $^1O_2$ being generated by the AuNPs. Therefore, for the same AuNPs concentration, the actual DPBF photobleach difference is less than 60%. Nevertheless, our experimental results support the conclusion that the additional DPBF photobleach in the presence of AuNPs occurs due to photogenerated $^1O_2$, which as a higher lifetime, and hence a higher detectivity, in EtOH/D_2O when compared to EtOH/H_2O (see Table 2.2 and Table 2.4).

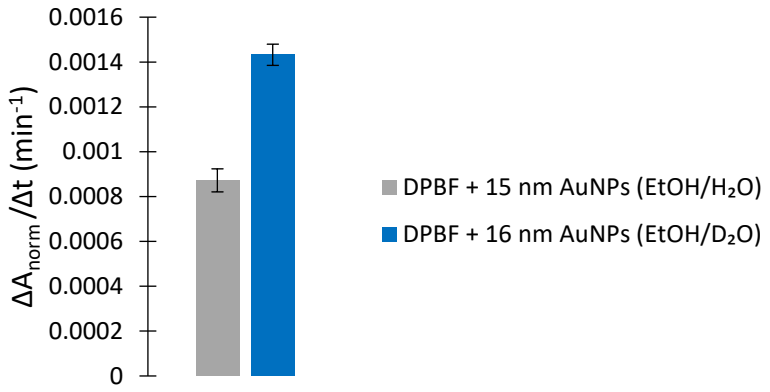

Figure 3.12 – Bar chart showing the gradient of the normalised DPBF decay (measured at 410 nm) in the irradiation time interval 20-60 min, in air-saturated solutions in 50/50 (v/v) ethanolic solutions with H_2O (average over five measurements) or D_2O (seven measurements) caused by the presence of 15 – 16 nm AuNPs upon CW-irradiation, 1 W. The EtOH/H_2O and EtOH/D_2O solutions had an absorbance of 0.45 ± 0.03 and 0.54 ± 0.01 at 532 nm, respectively. The grey and blue bars were obtained by subtracting the self-photobleach effect of DPBF, after shading correction, from the DPBF photobleach observed upon irradiation in the presence of AuNPs. The error bars show the standard error of the gradient.

Overall, our CW-irradiation results for DPBF in the presence of AuNPs clearly show that AuNPs generate ROS upon irradiation. However, at this point, it is not possible to confirm that the only ROS being generated is $^1O_2$ because DPBF is sensitive to other ROS as well.[26,27] Nonetheless, a comparison between the DPBF photobleach observed in EtOH/H_2O versus EtOH/D_2O strongly suggests that $^1O_2$ is involved, since the AuNPs effect in D_2O is larger than in H_2O.

3.4.2 Photogeneration of $^1O_2$ by irradiation of AuNPs detected by ABDA

The photogeneration of $^1O_2$ upon CW-irradiation of AuNPs was detected indirectly by UV-Vis spectroscopy using ABDA as a $^1O_2$ sensor. As described in chapter 1, ABDA reacts specifically and irreversibly with $^1O_2$ to generate an endoperoxide and does not react with any other ROS.[28–31]. However, as determined in chapter 2, ABDA is much less sensitive to $^1O_2$ than DPBF and this required the use of higher laser powers (3 W vs 1 W) and saturation of the solutions with O_2 to maximize $^1O_2$ photogeneration by AuNPs; furthermore, we used D_2O as solvent to maximize the $^1O_2$ lifetime, and hence the sensor detectivity. For a direct comparison with the DPBF results, the solution mixture EtOH/D_2O was also tested.

Before the irradiation of ABDA solutions in the presence of AuNPs, the ABDA photostability upon CW-irradiation was checked. Figure 3.13 shows the UV-Vis absorption spectra of O_2 saturated (1 bar) ABDA solution in the absence of AuNPs during CW irradiation at 532 nm with a power of 3 W, taken in 10 minutes intervals up to a maximum irradiation period of 60 minutes. No photodegradation of ABDA was observed upon irradiation in the absence of AuNPs, see also Figure 3.15. The absorbance of ABDA was constant throughout the irradiation period within the error of the measurement. Therefore, no correction comparable to the DPBF self-photobleach was required here to obtain the ABDA photobleach induced by the irradiation of AuNPs.

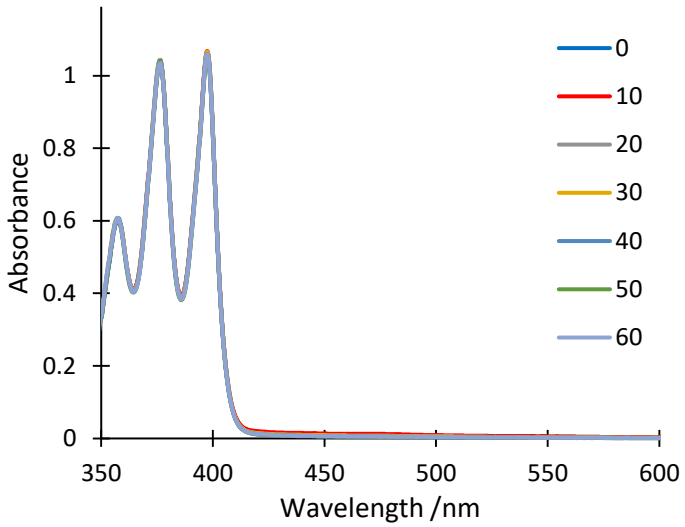

Figure 3.13 – UV-Vis Absorption spectra of O_2 saturated (1 bar) ABDA solution during CW-irradiation at 532 nm, 3 W, in D_2O. Absorbance spectra of ABDA were taken with 10 minutes intervals to a maximum irradiation period of 60 minutes.

Figure 3.14 shows the UV-Vis absorption spectra of ABDA in solution with 16 nm AuNPs [~ 1.1 (± 0.2) nM] during CW-irradiation at 532 nm, with a laser power of 3 W, in O_2 saturated D_2O solution. The absorbance spectrum of the solution mixture of ABDA and AuNPs is the sum of the two individual spectra – see Appendix 3, Figure A3. 15. Also, in the absence of laser irradiation, the absorbance of the solution mixture of ABDA and AuNPs remains stable (see Appendix 3 – Figure A3. 2A). In the presence of AuNPs, a small decrease of the ABDA absorbance was observed as the irradiation progressed, as highlighted in the inset of Figure 3.14. In the absence of laser irradiation, the absorbance of ABDA and AuNPs remains stable (see Appendix 3 – Figure A3. 2B) and the irradiation

does not affect the AuNPs. No significant variation of the characteristic SPR band of AuNPs absorbance at 520 nm was observed upon irradiation, see Figure 3.14.

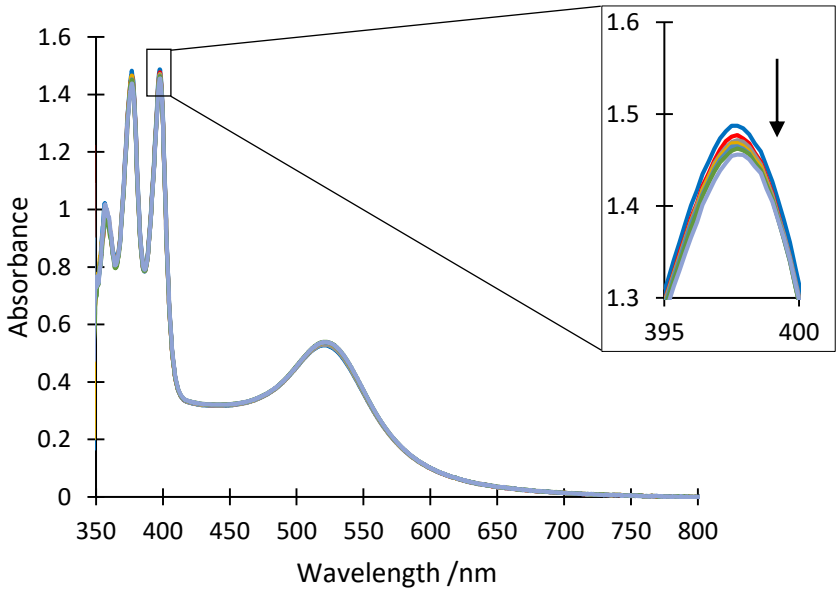

Figure 3.14 - UV-Vis absorption spectra of O_2 saturated (1 bar) ABDA solution during CW-irradiation at 532 nm, 3 W, in D_2O, in the presence of 16 nm AuNPs. Absorbance spectra were taken with 10 minutes intervals to a maximum irradiation period of 60 minutes. Inset: Detail of the ABDA absorption band between 395 and 400 nm. The arrow shows the direction of absorbance change.

The irradiation of O_2-depleted (N_2-saturated) ABDA solutions in the presence of AuNPs was also carried out (see Figure 3.15). An example of the UV-Vis absorption spectra of an ABDA solution with 16 nm AuNPs during CW-irradiation at 532 nm, with a laser power of 3 W, in N_2 saturated D_2O solutions can be seen in Appendix 3 – Figure A3. 11. Figure 3.15 shows the photostability of O_2-saturated ABDA solutions in D_2O in the absence of AuNPs, the photostability of N_2-saturated ABDA solutions in D_2O in the presence of 16 nm AuNPs and the time dependence of ABDA photobleaching in the presence of 16 nm AuNPs in O_2-saturated D_2O upon CW-irradiation at 532 nm, with a laser power of 3 W. The reproducibility of ABDA photobleach in the presence of AuNPs in O_2-saturated D_2O solutions can be seen in Appendix 3 – Figure A3. 12 and is indicated by the error bars in Figure 3.15.

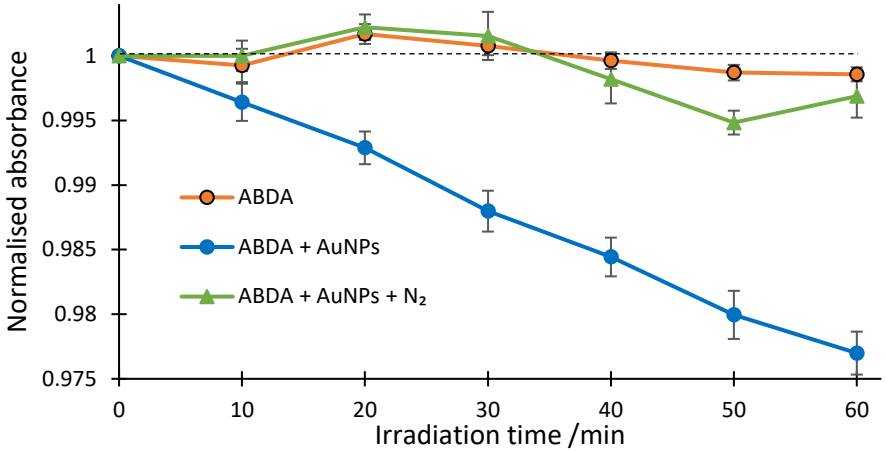

Figure 3.15 – Variation of the normalised ABDA absorbance at 398 nm in O_2-saturated solutions (1 bar) in D_2O in the absence and presence of 16 nm AuNPs, as well as N_2-saturated solutions (1 bar) upon CW-irradiation at 532 nm, 3 W. (ABDA – average over fourteen experiments, ABDA + AuNPs – nine experiments, ABDA + AuNPs + N_2 – three experiments). The dashed line shows a line at y=1 as a guide to the eye. The error bar shows the standard error of the measurement.

The loss of the absorbance of ABDA monitored at 398 nm during the CW-irradiation at 532 nm was mediated by the AuNPs and is in contrast to the photostability of ABDA in the absence of AuNPs. These results prove that AuNPs can, indeed generate ROS. Also, it can be further concluded that the ROS being generated is $^1O_2$ because ABDA reacts specifically with this ROS alone and does not react with any other ROS.[28–31] In contrast, no decrease of the ABDA absorbance was detected when N_2-saturated ABDA solutions in the presence of AuNPs were irradiated with 3 W. Upon reduction of the O_2 concentration in solution, AuNPs were no longer capable of generating $^1O_2$, and the ABDA photobleach was suppressed, thus further confirming the photogeneration of $^1O_2$ by AuNPs.

To better compare the ABDA photobleach against the DPBF photobleach in the presence of AuNPs, ABDA solutions were prepared in air and O_2-saturated 50/50 (v/v) EtOH/D_2O solutions and irradiated. Figure 3.16 shows the gradient of the ABDA photobleaching upon CW-irradiation at 532 nm in all solvent conditions tested, with a laser power of 3 W, in the presence of AuNPs. When ABDA in 50/50 (v/v) EtOH/D_2O was irradiated, the loss of ABDA absorbance decreased by ~40 % in O_2-saturated solutions and almost disappeared (decrease by ~85 %) in air-saturated solutions in comparison to O_2-saturated D_2O solutions. Our irradiation results compiled in Figure 3.16 clearly highlight that the ABDA absorbance photobleach changes due to the different O_2 concentration

and $^1O_2$ lifetime in the solution mixture upon irradiation of AuNPs. A more quantitative discussion of the results will be shown in the next section, 3.5.

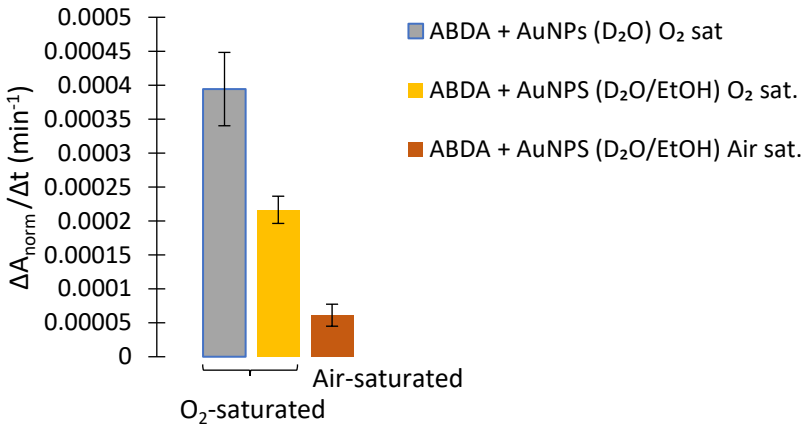

Figure 3.16 – Bar chart showing the gradient of the normalised ABDA absorbance decay (measured at 398 nm) in the presence of AuNPs in O_2-saturated D_2O solutions (grey – average over nine experiments) and O_2 and air-saturated solutions in 50/50 (v/v) D_2O/EtOH mixtures (yellow and brown, average over four and four experiments, respectively), upon CW-irradiation at 532 nm, 3 W. The error bars show the standard error of the gradient.

In summary, we have shown that AuNPs generate $^1O_2$ upon CW-irradiation at their SPR in aqueous solvents. This is the first conclusive proof of this effect, since the previous reports[7–9] were undertaken using DPBF as $^1O_2$ sensor, which is not exclusively sensitive to $^1O_2$, or seem to suffer from serious experimental artefacts, see section 3.5.4.

3.5 $^1O_2$ quantum yield of AuNPs

Here, we will use the experimental results regarding the photobleaching of ABDA and DPBF in the presence of AuNPs presented in the previous section to determine the $^1O_2$ generation quantum yield of AuNPs and compare it with the literature.

3.5.1 Method of quantum yield determination

The quantum yield of photogenerated $^1O_2$ (Φ_{NP}), i.e. the probability of AuNPs to generate a $^1O_2$ upon absorbing a photon, was determined by fitting the experimental data. Here, the time-dependent sensor absorbance, without normalization, but corrected for AuNPs absorbance (as described in section 3.2.5), was taken as data. In the case of

DPBF, the shading effect corrected self-photobleach was also subtracted (see section 3.2.6), and only data from 20 minutes were included. The data were fitted using the non-linear least-squares fitting routine described in Chapter 2 – section 2.2.5, slightly modifying C_1; Φ_{RB} was replaced by Φ_{NP} (Equation 3.4); A_0 and A(t) denote the initial absorbance and the time-dependent molecular probe absorbance during irradiation, and time t, respectively.

Equation 3.4

$$t = C_1\left(C_2\, ln\frac{A_0}{A(t)} + C_3[A_0 - A(t)]\right)$$

$$\text{where } C_1 = \frac{V\, N_A}{\varepsilon\, d\, N_{abs}\Phi_{NP}}, C_2 = \frac{\varepsilon\, d\, k_0}{k_r}, C_3 = \frac{k_r + k_q}{k_r}$$

Here, the experimental data were fitted with fixed C_3 and C_2 to determine C_1, which was then used to determine the value of Φ_{NP}. C_3, given by the ratio of the rate constants for physical and chemical quenching of $^1O_2$ by the sensor, was fixed to 1.35 and 1 for the fitting of the experimental data for ABDA and DPBF, respectively, based on literature reports, see section 2.3.4. C_2, which relates the rate constant for the chemical quenching of $^1O_2$ by the sensor to the intrinsic $^1O_2$ lifetime, was calculated for each solvent and probe using the k_r determined in chapter 2 (see Table 2.4), and the $^1O_2$ lifetimes (=1/k_0) and extinction coefficient values summarized in Table 2.2 and 2.3, respectively.

C_1 is given by the parameters related to the $^1O_2$ photosensitiser (Φ_{NP}), the sensor extinction coefficient (ε) and the experimental conditions (V – sample volume, d – the optical path-length and N_{abs} – the rate of photon absorption), all of which are known, with the exception of Φ_{NP}, which therefore can be determined from C_1. N_{abs} was determined from the power incident on the sample itself and the sample absorbance at 532 nm, which results exclusively from AuNPs, see Figure 2.1 and Figure 3.2. Each measurement was analysed individually, since the AuNPs and molecular probe concentration varied slightly between experiments. Therefore, the values of Φ_{NP} for the same conditions reported below (Figure 3.17) are the average of the individual Φ_{NP} and the errors the standard error.

3.5.2 Expected effects of oxygen concentration and viscosity

The reaction between the excited AuNPs and O_2 can be regarded as a bimolecular (second order) reaction, which depends on the concentration of the reactants and on the viscosity, via the second order rate constant, hence the value of Φ_{NP} is expected to depend on the O_2 concentration and solvent viscosity. It is obvious that in a solution mixture with a higher O_2 concentration, it is more likely for an O_2 molecule to come near a AuNPs to allow electron exchange by the Dexter mechanism to occur, hence increasing the amount of $^1O_2$ generated. Also, O_2 has a slower diffusion in a solvent mixture with a higher viscosity. Therefore, in a more viscous solvent, it is harder for the O_2 molecule to diffuse to the proximity of the AuNPs, which hinders $^1O_2$ generation. Table 3.1 summarizes the oxygen solubilities (K_s) and viscosities (η) of air-saturated solvents used in our irradiation experiments. As far as we are aware, there is no information in the literature that quantifies the viscosity and O_2 solubility in 50/50 (v/v) EtOH/D_2O mixtures, but our DPBF results suggest that they have a similar numerical value to 50/50 (v/v) EtOH/H_2O. Further interpretation of this observation will be discussed below.

Table 3.1 – Oxygen solubility (K_s) and viscosity (η) of different air-saturated solvent and solvent mixtures.

Solvent	**K_s[a] / mg L^{-1}**	**η[b] / mPa s**
H_2O	9.4 [18,32]	1.00 [33,34]
D_2O	9.9 [32]	1.25 [34]
EtOH/H_2O	23 [18,32]	2.56 [33]

[a] Solubility at 20 °C for air-saturated solutions.
[b] Viscosity at 20 °C.

3.5.3 $^1O_2$ quantum yield of AuNPs - Results

Figure 3.17 shows in a bar chart the $^1O_2$ generation quantum yield of AuNPs determined from the non-linear least-square fit of the absorbance change over time for both molecular probes, ABDA and DPBF, in different solvent and oxygen saturation conditions. Examples of the non-linear least square fitting result obtained for ABDA and DPBF in the presence of AuNPs under the same solvent conditions are shown in Appendix 3 – Figure A3. 13A and B.

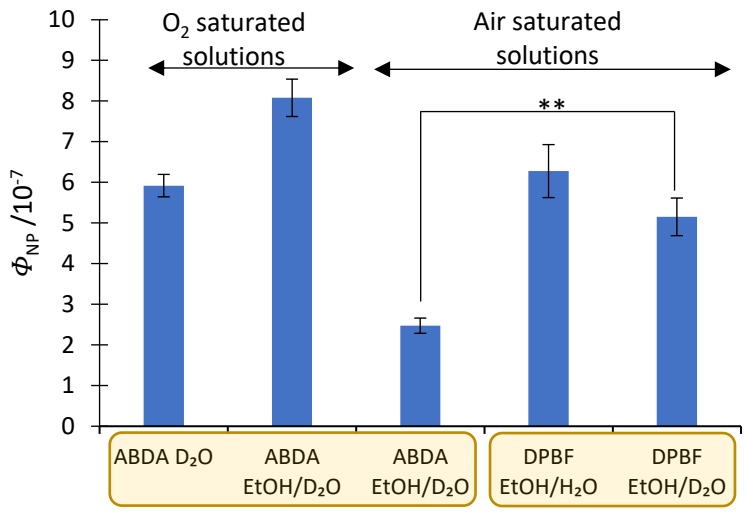

Figure 3.17 – Bar chart showing the $^1O_2$ quantum yield of AuNPs for different solvents and oxygen saturation conditions, determined from the photobleaching of ABDA and DPBF. ** indicates statistically significant differences between the results obtained with the two different $^1O_2$ molecular probes for the same solvent conditions, as determined by the ANOVA F-test at $p < 0.01$ ($p=0.0024$). Error bars show the standard error of the quantum yield.

DPBF: The $^1O_2$ quantum yield of AuNPs upon CW-irradiation at 532 nm determined from the rate of DPBF photobleach has a value of $(6.3 \pm 0.7) \times 10^{-7}$ and $(5.2 \pm 0.5) \times 10^{-7}$ for air-saturated solutions in EtOH/H_2O and EtOH/D_2O, respectively, i.e. the same Φ_{NP} within the error. The ANOVA F-test for Φ_{NP} determined from the DPBF photobleach showed no statistically significant difference between the two solvent conditions (p-value = 0.177).

ABDA: The $^1O_2$ quantum yield of AuNPs upon CW-irradiation at 532 nm determined from the rate of ABDA photobleach has a value of $(5.9 \pm 0.3) \times 10^{-7}$ and $(8.1 \pm 0.5) \times 10^{-7}$ for O_2 saturated solutions in D_2O and 50/50 (v/v) EtOH/D_2O, respectively. The irradiation of ABDA air-saturated 50/50 (v/v) EtOH/D_2O solutions in the presence of AuNPs yielded a $^1O_2$ quantum yield of $(2.5 \pm 0.2) \times 10^{-7}$. The irradiation of O_2-saturated ABDA solutions in 50/50 (v/v) EtOH/D_2O yielded a 3.5 times higher $^1O_2$ photogeneration quantum yield of AuNPs when compared to air-saturated solutions. This Φ_{NP} increase is lower than expected (5 times), assuming that the ABDA solutions in 50/50 (v/v) EtOH/D_2O were fully O_2-saturated, i.e. having a five times higher O_2 concentration in solution when compared to air-saturated conditions. Therefore, it is reasonable to suggest that our O_2 bubbling procedure does not saturate the solutions with O_2 completely. The irradiation of O_2-saturated solutions of ABDA in different solvents showed a Φ_{NP} which is ~30% higher in EtOH/D_2O when compared with D_2O. The difference in the Φ_{NP} values determined for

the two solvent conditions (D_2O vs EtOH/D_2O) agrees, within the error, with the ratio of the O_2 solubility and solvent viscosity.

Lastly and most importantly, Φ_{NP} determined from the photobleach of DPBF in a 50/50 (v/v) EtOH/D_2O air-saturated solution was found to have twice the value of the Φ_{NP} determined from the photobleach of ABDA under the same solvent conditions. The p-value (p-value = 0.0024) obtained from the ANOVA F-test for these sets of results strongly suggests that there is a statistically significant difference between the results. It is important to note that DPBF has been reported in the literature as a molecular probe not specific towards $^1O_2$. Therefore, it is reasonable to conclude that these results show that AuNPs can photogenerate $^1O_2$ since ABDA is sensitive only to $^1O_2$, but also suggest that AuNPs generate another ROS, which further increases the DPBF photobleach. For further discussion, see section 3.5.6.

Overall, the Φ_{NP} determined from our experimental results agrees with the upper value of Φ_{NP} reported by Chadwick *et al*. ($<10^{-6}$), which were based on experiments with DPBF alone.[9] However, the values are drastically smaller than the values reported by Vankayala *et al.*[8] and Pasparakis[7], who reported a AuNPs $^1O_2$ photogeneration quantum yield of 3 - 4%.

3.5.4 Critical analysis of AuNPs $^1O_2$ quantum yield reported in the literature

According to the literature, the reported efficiency with which AuNPs can generate $^1O_2$ varies over several orders of magnitude. Therefore, a critical analysis of the literature will be presented here.

Pasparakis determined the efficiency of $^1O_2$ photogeneration by 40 nm AuNPs using a (RNO)-histidine colourimetric assay and reported a Φ_{NP} of 0.03.[7] However, no results were shown at all that support this efficiency determination. The author also reported that the irradiation of 1 mL solution of DPBF in the presence of AuNPs ($A_{AuNPs\ at\ 530\ nm}$ = 0.3) with CW laser light at 532 nm with a laser power of 25 mW for 10 minutes caused a decrease of DPBF absorbance by ~10% and a slight broadening and red shift of the SPR peak due to the heat developed during the irradiation. Yet, under our irradiation conditions (see Figure 3.9) no AuNPs aggregation was observed when 1 W was used to

irradiate the same sample volume for 1 hour, even for AuNPs with an absorbance of 0.45 at the maximum of the SPR band. Additionally, and most importantly, our irradiation of DPBF solutions in the presence of AuNPs showed significant less DPBF photobleach in 10 minutes of irradiation when compared to the results presented by the author, although we used 20 times more power. Also, as described in appendix 1, the irradiation of DPBF solutions requires carefully controlled solution conditions to obtain reliable and reproducible results and can be distorted by minimal amounts of higher harmonic light emitted by the laser. The author did not show or describe any control experiments, i.e. the irradiation of DPBF in the absence of AuNPs, which suggest that his irradiation experiments were not done under similarly carefully controlled conditions. Lastly, the publication mentions that the same laser was used for CW and ns-pulse irradiation without giving any further details. To the best of my knowledge, such a laser does not exist, which suggests that the CW-irradiation was potentially nanosecond pulsed irradiation at higher repetition rates, which may cause significantly different results.[35] My supervisor, Dr. Martin Volk, has attempted to get further clarification from the author, but no clear response was given. Therefore, it seems likely that the Φ_{NP} value reported by the author was based on some artefacts, which are difficult to identify due to the lack of detailed information in the paper.

Vankayala *et al.* reported a similar efficiency of $^1O_2$ photogeneration by AuNPs as Pasparakis (0.037).[8] The authors estimated the Φ_{NP} by comparing the ratio of the integrated characteristic phosphorescence emission of $^1O_2$ in the range 1225 - 1300 nm upon irradiation of AuNPs and RB. Vankayala *et al.* also claim to have shown the photogeneration of $^1O_2$ upon laser irradiation of gold nanorods (AuNRs) at 940 nm, i.e. at the very tail of the SPR (see Figure 3.18), detected via the phosphorescence emission at 1270 nm.[11] The authors also measured the excitation spectrum by fixing the detection wavelength at 1263 nm and measuring the excitation spectrum in a standard emission spectrometer, see dotted line in Figure 3.18.

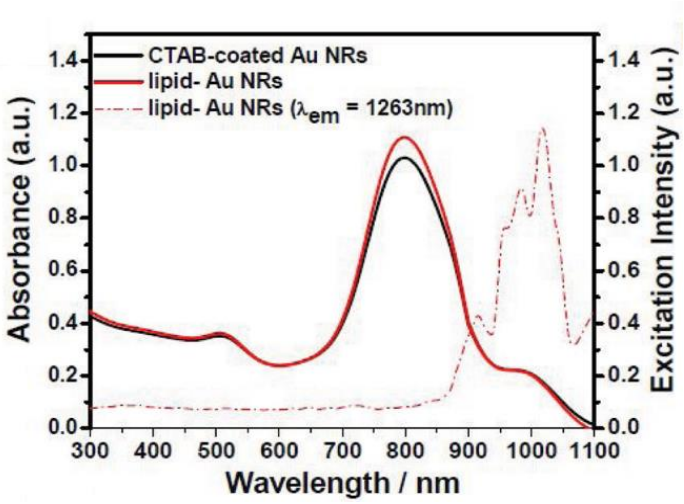

Figure 3.18 – Taken from Vankayala *et al.*.[11] Absorbance (solid lines) and excitation (dotted lines) spectra of nanorods (λ_{em} = 1263 nm).

The authors then suggested that $^1O_2$ could only be generated when the AuNRs were excited at the very tail of the SPR band above 875 nm. However, it would be reasonable to expect to see a higher $^1O_2$ generation at the peak maxima (~800 nm), not least because of the extremely fast electronic relaxation processes within gold nanoparticles, see section 1.2.3.2, Figure 1.8. Furthermore, the AuNRs tested by the authors were coated with cationic lipid, Lipofectamine 2000, and gold nanoparticles have been designed and reported as useful tools for surface-enhanced Raman scattering (SERS).[36,37] A simple conversion of the peak wavelengths of the excitation spectrum into vibrational wavenumbers (taking into account the 1263 nm emission wavelength) allowed a direct comparison of the peaks with Raman-active functional groups of Lipofectamin 2000, as shown in Table 3.2. This highlights the probability that the emission at 1263 nm does represent SERS of the AuNRs capping layer and not the luminescence of $^1O_2$.

Table 3.2 – Conversion and assignments of the peaks of the excitation spectrum shown in Figure 3.18.

Wavelength /nm	Wavenumber /cm^{-1}	Assignment
910	3071	Amine or Amide
975	2339	C-N
1025	1838	C=C
1100	1173	C-O-C

Overall, taking into consideration the misinterpretation of the results reported by both authors, it is reasonable to conclude that there are serious doubts about the results

for both publications which reported a $^1O_2$ photogeneration quantum yield of AuNPs much higher when compared to our results.

3.5.5 Theoretical estimate of Φ_{NP}

Our irradiation results of ABDA and DPBF showed that the CW-irradiation of AuNPs at their SPR generates $^1O_2$. Here, we will estimate the theoretical value of Φ_{NP} (Φ) and show that the $^1O_2$ generation quantum yield reported by Vankayala[8] and Pasparakis[7] is impossible to reconcile with the known rapid relaxation processes in AuNPs, as described in Chapter 1, section 1.2.3.2.

The literature suggests that the photogeneration of $^1O_2$ under CW-irradiation is mediated by the "primary hot" electrons, i.e. the electrons that are excited upon absorption of a photon but have not yet equilibrated by electron-electron scattering.[9] This is because, during CW irradiation, the excitation rate is so low that essentially only the energy of at most one photon is present at any time, so that the "hot" electrons do not have sufficient energy for the formation of $^1O_2$. During the lifetime of the "primary hot" electrons (0.1 ps), the excited electrons can either undergo electron-electron exchange with O_2 by the Dexter mechanism to generate a $^1O_2$ or undergo the relaxation process, as described in Chapter 1, section 1.2.3.2, which has a first order rate constant (k_a) of the electron-electron scattering process is 1 x 10^{13} s^{-1}.

Here, for the estimate of the Φ_{NP}, we assume that the reaction with O_2 is diffusion limited. The estimate given here will yield an upper limit of the $^1O_2$ photogeneration quantum yield of AuNPs. The diffusion-limited rate constant of a bimolecular reaction (k) is given by Equation 3.5, where R and D are the sum of the radii and the diffusion coefficients of O_2 and AuNPs in the solution, $R=R_{O2}+R_{NPs}$ and $D=D_{O2}+D_{NPs}$, respectively; N_A represents the Avogadro constant. Since the radius of O_2 is much smaller than AuNPs, i.e. $R_{NP} >> R_{O2}$, R can be approximated to the radius of the AuNPs ($R=R_{NP}$). Similarly, D can be approximated to the diffusion coefficient of O_2 because AuNPs are much larger than O_2 and hence move much more slowly (D_{D2O}=1.41 x 10^{-5} cm^2/s[38] and thus $D_{EtOH/D2O}$ = 0.7 x 10^{-5} cm^2/s, given the viscosity, see Table 3.1).

Equation 3.5

$$k = 4\,\pi\,R\,D\,N_A$$

Taking into consideration the rate constants calculated (k), the O_2 concentration in the ethanolic solution mixture (air-saturated [0.7 mM] and O_2-saturated [2.45 mM] - 3.5 times higher O_2 concentration suggested from our experimental results, see section 3.5.1) and the first order rate constant for the equilibration of the primary hot electrons (k_a), it was possible to estimate the maximum $^1O_2$ generation quantum yield of AuNPs (Φ_{max}) according to Equation 3.6, see Table 3.3. The theoretical Φ_{max} estimated here assumes that the reaction occurs every time an O_2 molecule encounters a AuNP, hence Φ_{max} is an upper limit under our irradiation conditions.

Equation 3.6

$$\Phi_{max} = \frac{k[O_2]}{k[O_2] + k_a}$$

Table 3.3 shows the maximum $^1O_2$ generation quantum yield (Φ_{max}) estimated from this equation and compares it with the Φ_{NP} determined from our experimental results for the irradiation of ABDA solutions.

Table 3.3 – Maximum $^1O_2$ generation quantum yield (Φ_{max}) for a diffusion limited reaction between an O_2 molecule and a photoexcited AuNP and Φ_{NP} determined from our ABDA experimental results in air-saturated and O_2 saturated solutions.

Solvent	Φ_{max} /10^{-7}	Φ_{NP} /10^{-7}
D_2O	95[b]	5.9[b]
	30[c]	
EtOH/D_2O[a]	100[b]	8.1[b]
	30[c]	2.5[c]

[a] 50/50 (v/v)
[b] O_2-saturated solution mixtures
[c] Air-saturated solution mixtures

The values of the maximum $^1O_2$ generation quantum yield Φ_{max} determined are four orders of magnitude smaller than the literature values for the $^1O_2$ generation quantum yield of AuNPs reported by Vankayala[8] and Pasparakis[7] for air-saturated aqueous solutions, which further confirms that their Φ_{NP} reports are highly unlikely to be correct. On the other hand, the theoretical Φ_{max} determined was found to be one order of magnitude larger when compared to our experimental results. However, it is important to highlight that the equilibration time of the primary hot electrons (0.1 ps) is only

approximately known and, most importantly, this theoretical Φ_{max} assumes that the reaction always occurs when a O_2 molecule encounter of a AuNPs, i.e. is a maximum value. Thus, our experimental results are in good agreement with this theoretical estimate.

3.5.6 Generation of other ROS by AuNPs

In Figure 3.17, we showed that the Φ_{NP} determined from the photobleach of DPBF in a 50/50 (v/v) EtOH/D_2O air-saturated solution was found to be twice the value of the Φ_{NP} determined from the photobleach of ABDA under the same solvent conditions, whereas the same Φ_{NP} would have been expected if the only reactive species being generated was $^1O_2$. According to the literature, ABDA reacts specifically with $^1O_2$ and does not react with any other ROS[28–31], whereas DPBF has been reported to be sensitive not only to $^1O_2$ but also to other ROS.[26,27] Therefore, we conclude that AuNPs can photogenerate $^1O_2$, but also suggest that AuNPs generate other ROS, which further increase the DPBF photobleach.

An alternative mechanism which in principle could enhance the DPBF photobleaching is field enhancement of the self-photobleach by the AuNPs, i.e. increased photon absorption by DPBF due to optical field enhancement at the AuNPs interface due to plasmonic resonance, which requires the DPBF molecules to be adsorbed to the AuNPs surface or to be in the close vicinity of the AuNPs. However, as shown in Appendix 3, Figure A3. 16, the absorbance spectrum of the solution mixture of DPBF and AuNPs is the sum of the two individual absorbance spectra, which suggests that DPBF molecules do not adsorb onto the AuNPs surface. Therefore, only a residual fraction of all DPBF molecules are near enough to the AuNPs to experience the field enhancement, which can not explain the 100% higher Φ_{NP} when compared to the ABDA photobleaching for the same solvent conditions, since the field enhancement effect enhances the absorbance only by a small factor, not several orders of magnitude.

To the best of our knowledge, this is the first evidence that irradiation of AuNPs at their SPR with visible light not only generates $^1O_2$, but also other ROS. Apart from $^1O_2$, there are two other ROS that can be generated in solution; hydroxyl radical (OH·) and superoxide anion radical ($O_2^{\cdot-}$). Given the well-known fact that alcohols are OH·

scavengers[39], it seems more likely that the second ROS species being generated in our irradiation experiments is $O_2^{\cdot-}$. Unfortunately, due to time constraints, it was not possible to further investigate which ROS is being photogenerated upon irradiation of AuNPs with visible light at their SPR.

3.6 Discussion

The irradiation of 15 – 16 nm AuNPs in their surface plasmon band with CW laser light (532 nm) leads to the generation of $^1O_2$, here detected indirectly by the variation of the absorbance of ABDA and DPBF. Overall, our results showed that less than one in a million photons absorbed by AuNP generates a $^1O_2$ under our irradiation conditions. The Φ_{NP} is indeed very low when compared with the PSs used nowadays in clinical PDT, such as Photofrin® ($\Phi_{SO} = 0.89$; $\mathrm{E} = 3000\ M^{-1}cm^{-1}$), ALA-induced protoporphyrin IX ($\Phi_{SO} = 0.56$; $\mathrm{E} = 5000\ M^{-1}cm^{-1}$), Foscan® ($\Phi_{SO} = 0.87$; $\mathrm{E} = 35000\ M^{-1}cm^{-1}$) or Chlorin (e6) ($\Phi_{SO} = 0.77$; $\mathrm{E} = 40000\ M^{-1}cm^{-1}$).[40,41] However, the small $^1O_2$ quantum yield of AuNPs is compensated by the extremely large absorption cross section of 15 – 16 nm AuNPs, 4 x 10^8 M^{-1} cm^{-1},[17] significantly larger than that of the organic dye molecules used in PDT.

Despite the small Φ_{NP} found in this thesis, AuNPs still hold great promises in the medical field for PDT applications due to the ability to selectively affect only the diseased tissue, namely due to their easy surface functionalization which allows AuNPs to be functionalized with specific molecules which are only recognized by particular types of cells, i.e. proteins or antibodies, and due to the localized action of $^1O_2$ (due to its short lifetime).[42,43] They also have much better stability against photo- or enzymatic degradation.

Recent work in our group showed that after 3 hours incubation of HeLa cells with 15 nm AuNPs@Citrate (2 nM), there were approximately 40,000 NPs in each cell and the irradiation of the incubated HeLa cells with a laser power of 3 W for 5 minutes caused significant cell death.[10] Note that the cell death has been demonstrated to occur following the irradiation of intracellular (endocytosed) AuNPs due to the ROS generated, because the irradiation levels were not high enough to cause hyperthermia.[9,44] These results showed clearly that the amount of $^1O_2$ generated in the cancer cells by our AuNPs was

enough to induce cell death. A further quantitative analysis shows that each AuNP (with an absorption cross section of 1.4 x 10^{-12} cm^2) absorbs 4 x 10^8 photons s^{-1} upon irradiation of the cell dish with a laser power of 3 W (beam diameter 1.85 mm). Hence, it was possible to determine the total number of photons absorbed in each single cell during the 5 minutes of irradiation (5 x 10^{15} photons). Taking into consideration the ϕ_{NP} (5.9 x 10^{-7}) determined in section 3.5.3, adjusted for air-saturated conditions (1.7 x 10^{-7}), a total of ~8 x 10^8 $^1O_2$ were generated during the 5 minutes of irradiation, which, taking into consideration the dimensions of a HeLa cell, yields a cumulative $^1O_2$ concentration of ~ 0.6 mM. This cumulative $^1O_2$ concentration is in good agreement with the cumulative $^1O_2$ concentration reported in the literature for the killing of different cancer cell, as shown in Table 3.4.

Table 3.4 – Cumulative $^1O_2$ concentration needed to kill several types of cells.

Cell type	**Cumulative $^1O_2$ concentration /mM**
MCF7	4.6[45]
EMT6 spheroids	12.1[46]
MLL	1.3 – 1.8[47]
AML5	0.2[48]

Overall, the $^1O_2$ photogeneration efficiency of 15 - 16 nm AuNPs determined here, although small, is sufficient to produce enough $^1O_2$ to kill cells, as evidenced by comparison with the literature (Table 3.4), further confirming that the recent results of HeLa cell killing found in our group are due to $^1O_2$ photogeneration. Lastly, the data presented above show that a $^1O_2$ quantum yield as high as 0.03 - 0.04, as suggested by some of the literature, should require a significantly lower irradiation dose to kill HeLa cells, thus further confirming the low Φ_{NP} as reported in section 3.5.3.

3.7 References

(1) Dykman, L. A.; Khlebtsov, N. G. Gold Nanoparticles in Biology and Medicine: Recent Advances and Prospects., *Acta Naturae.*, **2011**, *3*, 34.

(2) Yao, C.; Zhang, L.; Wang, J.; He, Y.; Xin, J.; Wang, S.; Xu, H.; Zhang, Z. Gold Nanoparticle Mediated Phototherapy for Cancer, *J. Nanomater.*, **2016**, *2016, 1.*

(3) Agostinis, P.; Berg, K.; Cengel, K.; Foster, T.; Girotti, A.; Gollnick, S.O.; Hahn, S.M.; Hamblin, M.R.; Juzeniene, A.; Kessel, D.; Koberlik, M.; Moan, J.; Mroz, P.; Nowis, D.; Piette, J.; Wilson, B.; Golab, J. Photodynamic Terapy of Cancer: An Update. *CA Cancer J Clin.* **2011**, *61*, 250.

(4) Lucky, S. S.; Soo, K. C.; Zhang, Y. Nanoparticles in Photodynamic Therapy. *Chem. Rev.* **2015**, *115*, 1990.

(5) Jain, S.; Hirst, D. G.; O'Sullivan, J. M. Gold Nanoparticles as Novel Agents for Cancer Therapy. *Br. J. Radiol.* **2012**, *85*, 101.

(6) Gamaleia, N.; Shton, I. Gold Mining for PDT : Great Expectations from Tiny Nanoparticles. *Photodiagnosis Photodyn. Ther.* **2015**, *12*, 221.

(7) Pasparakis, G. Light-Induced Generation of Singlet Oxygen by Naked Gold Nanoparticles and Its Implications to Cancer Cell Phototherapy. *Small* **2013**, *9*, 4130.

(8) Vankayala, R.; Sagadevan, A.; Vijayaraghavan, P.; Kuo, C. L.; Hwang, K. C. Metal Nanoparticles Sensitize the Formation of Singlet Oxygen. *Angew. Chemie - Int. Ed.* **2011**, *50*, 10640.

(9) Chadwick, S. J.; Salah, D.; Livesey, P. M.; Brust, M.; Volk, M. Singlet Oxygen Generation by Laser Irradiation of Gold Nanoparticles. *J. Phys. Chem. C* **2016**, *120*, 10647.

(10) Chadwick, S. Photodynamic and Photothermal Human Cancer Cell Killing Using Gold Nanoparticles, PhD thesis, *University of Liverpool*, **2015**.

(11) Vankayala, R.; Huang, Y.; Kalluru, P.; Chiang, C.S.; Hwang, K. C. First Demonstration of Gold Nanorods-Mediated Photodynamic Therapeutic Destruction of Tumors via Near Infra-Red Light Activation. *Small* **2014**, *10*, 1612.

(12) Turkevich, J.; Stevenson, P. C.; Hillier, J. A Study of the Nucleation and Growth Processes in the Synthesis of Colloidal Gold. *Discuss. Faraday Soc.* **1951**, *11*, 55.

(13) Frens, G. Controlled Nucleation for the Regulation of the Particle Size in Monodisperse Gold Suspensions. *Nat. Phys. Sci.* **1973**, *241*, 20.

(14) Ojea-Jiménez, I.; Romero, F. M.; Bastús, N. G.; Puntes, V. Small Gold Nanoparticles Synthesized with Sodium Citrate and Heavy Water: Insights into the Reaction Mechanism. *J. Phys. Chem. C* **2010**, *114*, 1800.

(15) Venyaminov, S. Y.; Prendergast, F. G. Water (H_2O and D_2O) Molar Absorptivity in the 1000–4000 cm^{-1} Range and Quantitative Infrared Spectroscopy of Aqueous Solutions. *Anal. Biochem.* **1997**, *248*, 234.

(16) Krpetić, Ž.; Davidson, A. M.; Volk, M.; Lévy, R.; Brust, M.; Cooper, D. L. High-Resolution Sizing of Monolayer-Protected Gold Clusters by Differential Centrifugal Sedimentation. *ACS Nano* **2013**, *7*, 8881.

(17) Haiss, W.; Thanh, N. T. K.; Aveyard, J.; Fernig, D. G. Determination of Size and Concentration of Gold Nanoparticles from UV-Vis Spectra. *Anal. Chem.* **2007**, *79*, 4215.

(18) Pan, G.; Yang, B. Effect of Surface Hydrophobicity on the Formation and Stability of Oxygen Nanobubbles. *ChemPhysChem* **2012**, 13, 2205.

(19) Olmsted, J. Photooxidation of Isobenzofurans. *J Am Chem Soc* **1973**, *95*, 6211.

(20) Mendenhall, G. D.; Howard, A.; Mendenhall, G. D. Autooxidation and Photooxidation of 1,3-Diphenylisobenzofuran: A Kinetic and Product Study. *Can. J. Chem.* **1975**, *53*, 2199.

(21) Wilkinson, F.; Brummer, J. G. Rate Constants for the Decay and Reactions of the Lowest Electronically Excited Singlet State of Molecular Oxygen in Solution. *J. Phys. Chem. Ref. Data*, **1981**, *10*, 809.

(22) Rodgers, M. A. J. Solvent-Induced Deactivation of Singlet Oxygen: Additivity Relationships in Nonaromatic Solvents. *J. Am. Chem. Soc.* **1983**, *105*, 6201.

(23) Schmidt, R.; Afshari, E. Collisional Deactivation of O_2 ($^1\Delta_g$) by Solvent Molecules. Comparative Experiments with $^{16}O_2$ and $^{18}O_2$. *Berichte der Bunsengesellschaft für Phys. Chemie* **1992**, *96*, 788.

(24) Herkstroeter, W. G.; Merkel, P. B. The Triplet State Energies of Rubrene and Diphenylisobenzofuran. *J. Photochem.* **1981**, *16*, 331.

(25) Merkel, P. B.; Kearns, D. R. Radiationless Decay of Singlet Molecular Oxygen in Solution. Experimental and Theoretical Study of Electronic-to-Vibrational Energy Transfer. *J. Am. Chem. Soc.* **1972**, *94*, 7244.

(26) Ohyashiki, T.; Nunomura, M.; Katoh, T. Detection of Superoxide Anion Radical in Phospholipid Liposomal Membrane by Fluorescence Quenching Method Using 1,3-Diphenylisobenzofuran. *Biochim. Biophys. Acta - Biomembr.* **1999**, *1421*, 131.

(27) Żamojć, K.; Zdrowowicz, M.; Rudnicki-Velasquez, P. B.; Krzymiński, K.; Zaborowski, B.; Niedziałkowski, P.; Jacewicz, D.; Chmurzyński, L. The Development of 1,3-Diphenylisobenzofuran as a Highly Selective Probe for the Detection and Quantitative Determination of Hydrogen Peroxide. *Free Radic. Res.* **2017**, *51*, 38.

(28) Lindig, B. A.; Rodgers, M. A. J. J.; Schaaplc, A. P.; Schaap, A. P. Determination of the Lifetime of Singlet Oxygen in Water-D_2 Using 9,10-Anthracenedipropionic Acid, a Water-Soluble Probe. *J. Am. Chem. Soc.* **1980**, *102*, 5590.

(29) Burns, J. M.; Cooper, W. J.; Ferry, J. L.; King, D. W.; DiMento, B. P.; McNeill, K.; Miller, C. J.; Miller, W. L.; Peake, B. M.; Rusak, S. A.; Rose, A. L.; Waite, T. D. Methods for Reactive Oxygen Species (ROS) Detection in Aqueous Environments. *Aquat. Sci.* **2012**, *74*, 683.

(30) Umezawa, N.; Tanaka, K.; Urano, Y.; Kikuchi, K.; Higuchi, T.; Nagano, T.; Cryst, M.; Cryst, L.; Kaupp, G. Novel Fluorescent Probes for Singlet Oxygen. *Angew. Chemie-*

International Ed. **1999**, *38*, 2899.

(31) Gomes, A.; Fernandes, E.; Lima, J., Fluorescence Probes Used for Detection of Reactive Oxygen Species. *J. Biochem. Biophys. Methods* **2005**, *65*, 45.

(32) Lawrence, H.; Battino, R.; Miyamoto, H.; Yampolski, Y.; Young, C. L. IUPAC-NIST Solubility Data Series. 103. Oxygen and Ozone in Water, Aqueous Solutions, and Organic Liquids (Supplement to Solubility Data Series Volume 7). *J. Phys. Chem. Ref. Data* **2014**, *43*, 33102.

(33) Khattab, I. S.; Bandarkar, F.; Fakhree, M. A. A.; Jouyban, A. Density, Viscosity, and Surface Tension of Water+ethanol Mixtures from 293 to 323K. *Korean J. Chem. Eng.* **2012**, *29*, 812.

(34) Millero, F. J.; Dexter, R.; Hoff, E. Density and Viscosity of Deuterium Oxide Solutions from 5-70.Deg. *J. Chem. Eng. Data* **1971**, *16*, 85.

(35) Jones, S. F., *Singlet Oxygen Evolution by Laser Irradiation of Gold Nanoparticles – A Potential Treatment of Cancer*; Master thesis, *University of Liverpool*, **2017**.

(36) Mu, Z.; Zhao, X.; Xie, Z.; Zhao, Y.; Zhong, Q.; Bo, L.; Gu, Z. In Situ Synthesis of Gold Nanoparticles (AuNPs) in Butterfly Wings for Surface Enhanced Raman Spectroscopy (SERS). *J. Mater. Chem. B* **2013**, *1*, 1607.

(37) Cao, X.; Hong, S.; Jiang, Z.; She, Y.; Wang, S.; Zhang, C.; Li, H.; Jin, F.; Jin, M.; Wang, J. SERS-Active Metal–organic Frameworks with Embedded Gold Nanoparticles. *Analyst* **2017**, *142*, 2640.

(38) Han, P.; Bartels, D. M. Temperature Dependence of Oxygen Diffusion in H_2O and D_2O, *J. Phys. Chem.* **1996**, *100*, 5597.

(39) Sicard-Roselli, C.; Brun, E.; Gilles, M.; Baldacchino, G.; Kelsey, C.; McQuaid, H.; Polin, C.; Wardlow, N.; Currell, F. A New Mechanism for Hydroxyl Radical Production in Irradiated Nanoparticle Solutions. *Small* **2014**, *10*, 3338.

(40) Fernandez, J. M.; Bilgin, M. D.; Grossweiner, L. I. Singlet Oxygen Generation by Photodynamic Agents. *J. Photochem. Photobiol. B Biol.* **1997**, *37*, 131.

(41) Ormond, A. B.; Freeman, H. S. Dye Sensitizers for Photodynamic Therapy. *Materials (Basel).* **2013**, *6*, 817.

(42) Dougherty, T. J.; Gomer, C. J.; Henderson, B. W.; Jori, G.; Kessel, D.; Korbelik, M.; Moan, J.; Peng, Q. Photodynamic Therapy. *J. Natl. Cancer Inst.* **1998**, *90*, 889.

(43) DeRosa, M. C.; Crutchley, R. J. Photosensitized Singlet Oxygen and Its Applications. *Coord. Chem. Rev.* **2002**, *233*, 351.

(44) Krpetić, Ž.; Nativo, P.; Sée, V.; Prior, I. A.; Brust, M.; Volk, M.; Inflicting Controlled Nonthermal Damage to Subcellular Structures by Laser-Activated Gold Nanoparticles. *Nano Lett.* **2010**, *10*, 4549.

(45) Anquez, F.; El Yazidi Belkoura, I.; Suret, P.; Randoux, S.; Courtade, E. Cell Death Induced by Direct Laser Activation of Singlet Oxygen at 1270 nm. *Laser Phys.* **2013**, *23*, 25601.

(46) Georgakoudi, I.; Nichols, M. G.; Foster, T. H. The Mechanism of Photofrin

Photobleaching and Its Consequences for Photodynamic Dosimetry. *Photochem. Photobiol.* **1997**, *65*, 135.

(47) Dysart, J. S.; Singh, G.; Patterson, M. S. Calculation of Singlet Oxygen Dose from Photosensitizer Fluorescence and Photobleaching During mTHPC Photodynamic Therapy of MLL Cells. *Photochem. Photobiol.*, **2005**, *81, 196*.

(48) Niedre, M. J.; Secord, A. J.; Patterson, M. S.; Wilson, B. C. In Vitro Tests of the Validity of Singlet Oxygen Luminescence Measurements as a Dose Metric in Photodynamic Therapy. *Cancer Res.* **2003**, *63*, 7986.

Chapter 4

4. Gold nanoparticles coated with bovine serum albumin as singlet oxygen photosensitisers

4.1 Introduction

The use of AuNPs as a potential tool for clinical practice has become increasingly popular, especially in the area of drug delivery, bioimaging and phototherapy.[1,2] Particularly relevant to this project, AuNPs have the ideal properties for PDT applications. They can be easily synthesised in a variety of sizes and shapes, have low toxicity and are easily functionalized.[3,4] The latter property plays an important role in modern gold nanotechnology.[5,6]

As with many NPs, "naked" AuNPs (AuNPs@Citrate) when dispersed in a biological environment, e.g. the bloodstream, are readily coated by a layer of different proteins, forming a so-called protein corona, hence most cells never encounter the "naked" particles. This uncontrolled corona formation can have consequences on the AuNPs' stability and performance, uptake and cell retention, or even give rise to new and potentially undesired properties.[7,8] In contrast, if the protein corona is generated in a controlled environment, it can have beneficial effects, such as an increased biocompatibility and specificity of the drug towards specific types of cells[9,10] Among various proteins, serum albumins are the most abundant circulating proteins in the blood, representing 52 - 62% of the total plasma protein fraction.[11] They play an essential part in several body biomechanisms, especially in binding and transport of both endogenous and exogenous molecules such as fatty acids, cholesterol, peptides, therapeutic drugs and metal ions.[12] Bovine serum albumin (BSA) is a globular protein with the approximate shape of an equilateral triangular prism (see Figure 4.1A), commonly used in biophysical and biochemical studies due to its availability, purity, low cost, and structural and functional similarities to human serum albumin.[13] According to the literature, the

incubation of citrate-stabilized AuNPs with BSA leads to the formation of a chemisorbed protein corona, and this binding is achieved by the formation of a covalent bond between gold and sulphur of cysteine 45 (highlighted in Figure 4.1 as a yellow sphere), located at the base of the triangular prism. This leads to the formation of a layer of proteins which stand "upright" on the AuNPs surface as shown below.[16]

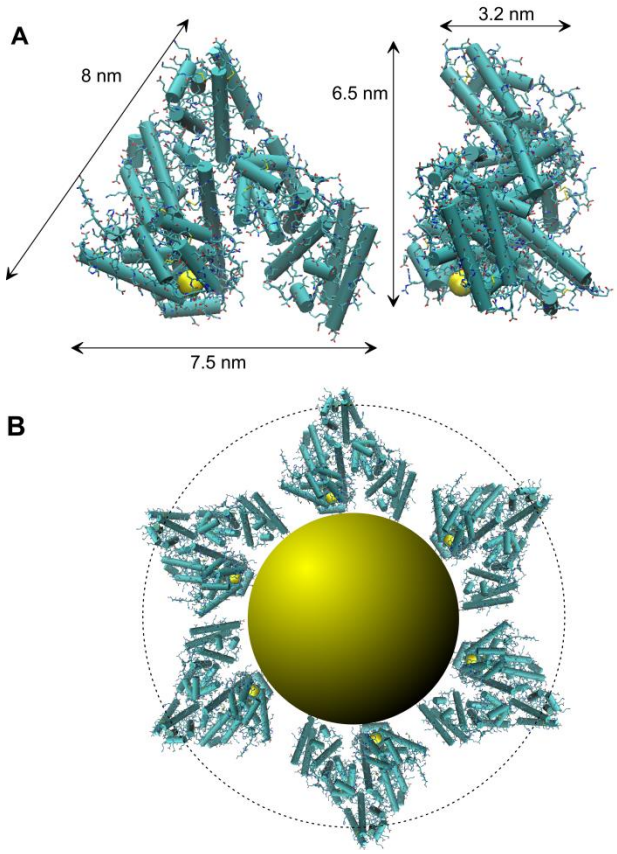

Figure 4.1 – A) Structure of BSA (PDB-ID 4F5S)[14], the cylinders represent α-helices, and the yellow sphere indicates the sulfur of cysteine 45 (created using VMD[15]). B) Cartoon representation of the protein corona formed by BSA on a AuNP; the dotted line indicates the effective corona thickness due to the surface functionalization. Image taken from [16]

Despite the benefits of the functionalization of AuNPs for biomedical applications, it has been reported in the literature that the functionalization of AuNPs with a relatively dense capping layer, i.e. PEG-OH (HS-$(CH_2)_{11}$-$(EG)_4$-OH), reduced the $^1O_2$ generation by AuNPs upon CW-irradiation considerably.[17] According to the authors, PEG-OH assembles at the surface of AuNPs in a very densely packed conformation which inhibits O_2 diffusion to the AuNP surface to undergo $^1O_2$ generation by the Dexter

mechanism. In comparison, due to its porosity and irregular shape, the literature suggests that BSA does not form close packed layers on the surface of AuNPs (see Figure 4.1B) [16] which may allow the O_2 dissolved in the solvent to diffuse to the surface of AuNPs.

Here, we functionalized AuNPs with different BSA incubation concentrations, resulting in capping layers of varying capping density and evaluated the $^1O_2$ photogeneration efficiency upon CW-irradiation (at 532 nm). The photogeneration of $^1O_2$ was confirmed indirectly by photobleaching of ABDA and DPBF, and the $^1O_2$ quantum yield of the functionalized AuNPs@BSA was determined and compared with that of citrate-stabilised AuNPs.

4.2 Experimental

4.2.1 Materials

ABDA, BSA and D_2O were purchased from Sigma-Aldrich, DPBF and ethanol were purchased from Fisher Scientific. Oxygen (O_2 - 99.5%) gas was purchased from BOC. All chemicals were used as received.

Before use, all glassware, cuvettes and stirrer bars were cleaned in Aqua Regia (3:1 HCl:HNO_3) and thoroughly rinsed with Milli-Q water and set to dry. A more detailed protocol for the cleaning of cuvettes and stirrer bars can be found in Appendix 1, section A1.1.

4.2.2 Singlet oxygen detection

$^1O_2$ was detected via photobleaching of ABDA and DPBF, as described in detail in Chapter 3, subsection 3.2.5.

4.2.3 Irradiation setup

The irradiation of AuNPs solutions capped with BSA was performed with the same irradiation setup described in Chapter 3, section 3.2.4.

4.2.4 Gold nanoparticles coated with BSA

4.2.4.1 Gold nanoparticles preparation and ligand exchange

15.8 nm AuNPs@Citrate in D_2O were used in this study. The synthesis and characterisation of these AuNPs were described in Chapter 3, subsection 3.2.2. AuNPs@Citrate were capped with BSA using the following protocol. A BSA stock solution in D_2O [8.77×10^{-4} M] was prepared and used on the following day for the ligand exchange experiment. The BSA stock solution was kept in the fridge overnight before use. The ligand exchange was done by adding an aliquot of BSA stock solution to 4 mL of citrate AuNPs solution to yield final BSA concentrations of 1.8♣, 4.4 and 41.8 µM. The ligand exchange was performed with different BSA concentrations to achieve different BSA capping layer densities.[16] The samples were prepared in glass vials, shaken vigorously for a few seconds and left standing overnight at room temperature.

4.2.4.2 Gold nanoparticles characterisation

Figure 4.2 shows the UV-Vis spectra of AuNPs@Citrate in D_2O and AuNPs incubated with different BSA concentrations in D_2O. The UV-Vis spectra were normalised to 1 at the SPR maxima.

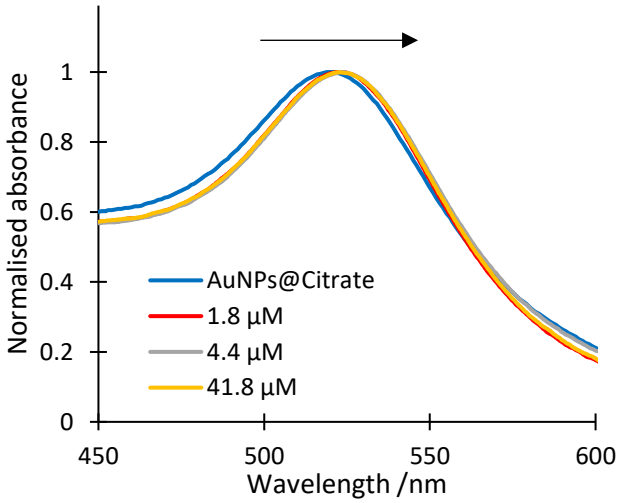

Figure 4.2 – UV-Vis spectra of AuNPs@Citrate in D_2O and AuNPs incubated with different BSA concentrations in D_2O, 1.8, 4.4 and 41.8 µM. UV-Vis spectra normalised to 1 at the SPR band maxima.

♣ - The preparation of 1.8 µM BSA /AuNPs solution required the stock solution to be diluted 1:6.

The characteristic SPR band of AuNPs, responsible for the red colour of the colloidal solution, was also observed for all AuNPs@BSA samples. A clear redshift of the SPR band was observed when the SPR band position for AuNPs@Citrate (520 nm) was compared with that for AuNPs@BSA (522 nm for the lowest BSA concentration used – 1.8 µM), hence confirming the protein corona formation. Increasing the BSA concentration from 1.8 to 41.8 µM resulted in a further redshift (1 nm) of the SPR, as expected for an increase of the capping layer density.

To further confirm the surface functionalization of AuNPs with BSA, all AuNPs@BSA samples were characterised by differential centrifugal sedimentation (DCS), and the effective capping layer thickness determined. Figure 4.3 shows the raw results of DCS experiments for citrate stabilised AuNPs before and after protein corona formation by incubation in BSA solution in D_2O.

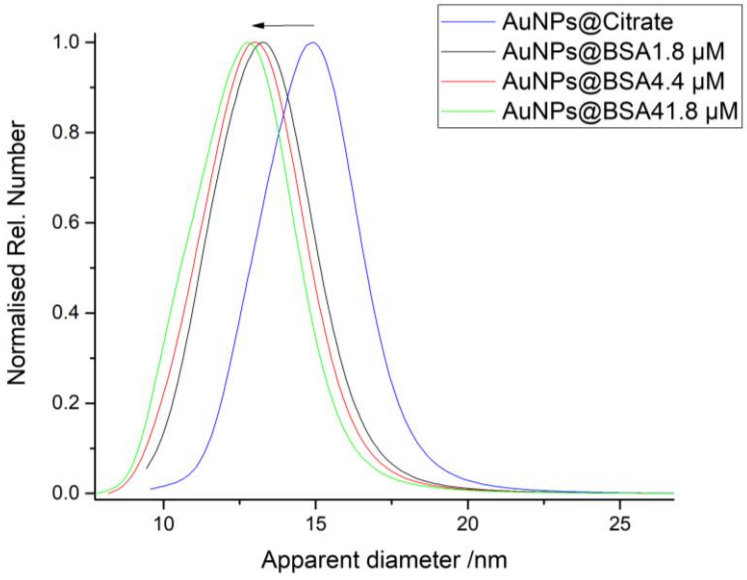

Figure 4.3 – Normalised number size distributions of AuNPs@Citrate in D_2O and AuNPs with BSA for different BSA incubation concentrations in D_2O, 1.8, 4.4 and 41.8 µM, respectively. Shown here are the raw data, i.e. the distribution of apparent particle diameters d_{DCS} as reported by the DCS software. The arrow shows the shift to smaller apparent size with increasing ligand size.

These distributions show that the AuNPs@BSA were highly monodisperse and that the width of the size distribution was not affected by incubation in BSA solution. The size distributions also show that upon incubation with BSA, the apparent particle size, i.e. the apparent particle diameter obtained directly from the DCS analysis (maxima of the distributions) decreases with the increase of the BSA incubation concentration. This is due to a necessary oversimplification in the analysis of the raw data, as mentioned in

chapter 3, section 3.2.2.2. Briefly, the DCS instrument records the sedimentation time that the AuNPs require for travelling from the injection point to the point where AuNPs are detected. The sedimentation time is then used to calculate the size, taking into consideration a calibration sample with a known diameter and the density of the AuNPs, here assumed to be the density of the gold core (ρ_{Au} = 19.3 g cm^{-3}), thus ignoring the contribution of the capping layer. Consequently, this causes an overestimation of the effective density of the NP, and an underestimation of the particle size.

In line with the result analysis described in section 3.2.2.2, here we used the AuNPs core diameter determined there (15.8 nm) and determined the thickness of the capping layer size (Table 4.1), taking into consideration the maxima of the distributions shown in Figure 4.3 and an overall capping layer density of 1.15 g cm^{-3}, as suggested by Davidson *et al.*[16]. The authors suggested that the density of the BSA corona is slightly smaller than the density of hydrated protein crystals (~ 1.25 g cm^{-3}) due to the higher porosity expected for a thin protein corona - due to its irregular shape, BSA does not form close packed layers on the surface of AuNPs (see Figure 4.1). A more detailed description of the DCS results analysis to obtain the capping layer thickness was given elsewhere.[16,18] Table 4.1 shows the wavelengths of the maxima of the SPR band of AuNPs@Citrate and AuNPs@BSA for different BSA incubation concentrations, as well as the capping layer thicknesses determined by DCS.

Table 4.1 - Table showing the maxima SPR band position and capping layer size of AuNPs@Citrate and AuNPs@BSA for different BSA incubation concentrations.

[BSA] / µM	Maximum SPR band / nm	Capping layer thickness/ nm
0	520	1 (Citrate)
1.8	522	3.2 (3.0)**
4.4	523	4.1 (3.8)**
41.8	523	4.2 (4.9)**

** - Literature results of the capping layer thickness of AuNPs@BSA for these incubation concentrations are shown in brackets.[16]

The thickness of the protein corona increased with an increase in the BSA incubation concentration, ranging from 3.2 to 4.2 nm. The capping layer thicknesses determined for BSA incubation at 1.8 and 4.4 µM are in good agreement with the results

reported by Davidson *et al.*.[16] However, the capping layer thickness determined for the incubation with the highest BSA concentration (41.8 μM) showed a significantly lower value when compared with the literature. This difference in the capping layer thickness most likely arises from experimental uncertainties, either during the capping stage or the DCS characterisation.

Overall, our results show that BSA binds spontaneously to the surface of AuNPs. Due to the BSA dimensions and shape, we believe that BSA binds to the surface of the AuNPs forming self-assembled monolayers generating a protein corona, as suggested by Davidson *et al.* (see Figure 4.1).[16]

4.3 Photogeneration of $^1O_2$ upon irradiation of AuNPs coated with BSA

Here, the photogeneration of $^1O_2$ upon CW-irradiation of AuNPs@BSA at 532 nm with different capping layers will be shown. As in Chapter 3, the $^1O_2$ generation will be investigated by measuring the photoinduced bleach of the chemical traps characterised in chapter 2, ABDA and DPBF. The irradiation of ABDA solutions in the presence AuNPs@BSA was done in O_2-saturated D_2O solutions to increase the O_2 concentration in solution, the lifetime of $^1O_2$ and the ABDA sensitivity towards $^1O_2$. The bubbling procedure was described in detail in chapter 3, section 3.2.3. The irradiation of DPBF solutions in the presence of AuNPs@BSA was done in air-saturated 50/50 (v/v) EtOH/D_2O mixtures.

4.3.1 Photogeneration of $^1O_2$ by irradiation of AuNPs@BSA detected by ABDA

Figure 4.4 shows the variation of the normalised ABDA absorbance at 398 nm in O_2-saturated solutions in D_2O in the presence of AuNPs@BSA incubated with different BSA concentrations, upon CW-irradiation at 532 nm with a power of 3 W. For comparison, the ABDA photobleaching results obtained upon irradiation of AuNPs@Citrate under the same irradiation and solvent conditions were added to the graph. A clear decrease of the

ABDA absorbance monitored at 398 nm was observed for all tested samples, due to the photosensitization reaction at 532 nm mediated by the AuNPs@BSA. Within the error of the measurement, the photobleaching of ABDA observed was independent of the BSA capping layer density. It would be interesting to investigate the effect of $^1O_2$ on the BSA, for example, by undertaking DCS measurements after the irradiation. However, due to time constraints, this was not possible as part of this project.

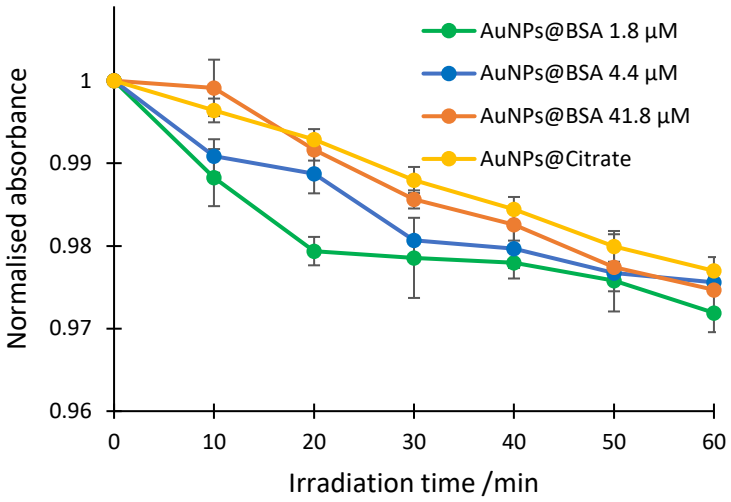

Figure 4.4 – Variation of the ABDA absorbance at 398 nm, normalised to the initial absorbance, averaged over several measurements in O_2-saturated (1 bar) D_2O solution upon CW-irradiation at 532 nm (3 W) in the presence of AuNPs@Citrate (for comparison) and AuNPs@BSA for different incubation concentrations, 1.8 (two measurements), 4.4 (two measurements) and 41.8 µM (two measurements). The samples were irradiated in 10 minutes intervals to a maximum irradiation period of 60 minutes. The error bars show the standard error of the experiment.

4.3.2 Photogeneration of $^1O_2$ by irradiation of AuNPs@BSA detected by DPBF

Figure 4.5 shows the variation of the normalised DPBF absorbance at 410 nm in air-saturated 50/50 (v/v) EtOH/D_2O solution mixtures, caused by the ROS generated by AuNPs@BSA incubated with different BSA concentrations, upon CW-irradiation at 532 nm with a power of 1 W. Note that the DPBF absorbance shown in Figure 4.5 is the DPBF absorbance change after subtraction of the self-photobleach of DPBF in the absence of AuNPs, corrected for the shading effect (as described in section 3.2.6). A clear decrease of the DPBF absorbance during the photosensitising reaction at 532 nm mediated by the AuNPs@BSA was also observed for all tested samples, independent of the capping layer

density. The DPBF photobleach effect in the presence of AuNPs functionalized with BSA also showed the two characteristic phases observed for the DPBF photobleaching, as described in the previous chapter.

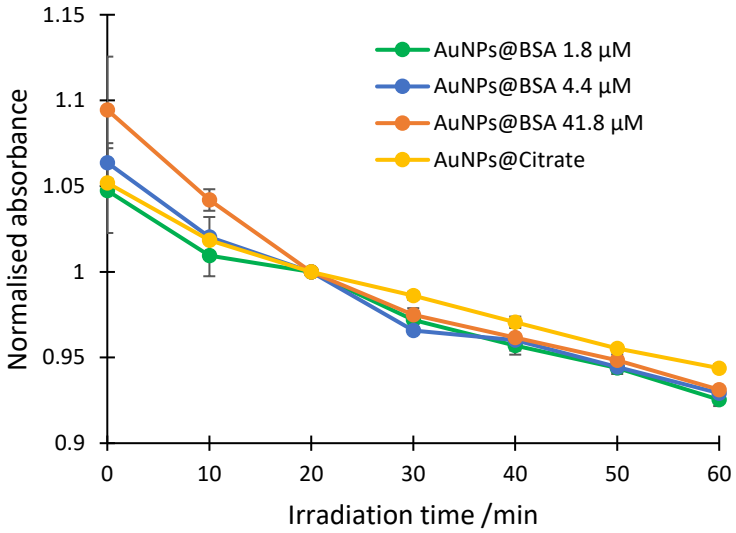

Figure 4.5 - Variation of the DPBF absorbance at 410 nm, normalised at 20 min, averaged over several measurements in air-saturated EtOH/D_2O solution upon CW-irradiation at 532 nm (1 W) in the presence of AuNPs@Citrate and AuNPs@BSA for different incubation concentrations, 1.8 (two measurements), 4.4 (two measurements) and 41.8 µM (three measurements). The DPBF absorbance is the DPBF absorbance variation after subtraction of the DPBF self-photobleach, corrected for the shading effect. The error bars show the standard error. Note that the error bars are smaller than the symbol size for the points after 20 minutes.

As in the previous section 4.3.1., the $^1O_2$ generated by AuNPs@BSA upon irradiation at 532 nm was found to be independent of the BSA capping layer density, and it is clearly very similar to the DPBF photobleach caused by the irradiation of AuNPs@Citrate, with potentially a slight increase, although this is barely statistically significant.

4.4 Quantum yield of $^1O_2$ photogenerated by AuNPs@BSA

In the preceding section, we have shown that AuNPs functionalized with BSA still generate $^1O_2$. Here, we will use the experimental results regarding the photobleaching of ABDA and DPBF in the presence of AuNPs@BSA presented in the previous section to determine the $^1O_2$ generation quantum yield of AuNPs@BSA and compare it with the AuNPs@Citrate. The quantification of the $^1O_2$ quantum yield of AuNPs@BSA ($\Phi_{NP@BSA}$)

was done by fitting the experimental data, i.e. the absorbance change over time of both molecular probes tested, ABDA and DPBF, using the same non-linear least-square fitting routine described in chapter 3, section 3.5.1, using Equation 3.4. As justified there, the ABDA results were fitted using C_3 = 1.35, and the DPBF results were fitted using C_3 = 1. The values of C_2 were determined as described in section 3.5, and $\Phi_{NP@BSA}$ was determined from the fit results for C1. Figure 4.6 shows in a bar chart the $\Phi_{NP@BSA}$ determined from these non-linear least-square fits. For comparison, the Φ_{NP} determined for AuNPs@Citrate obtained in both solvent conditions are also shown (diagonally striped bars).

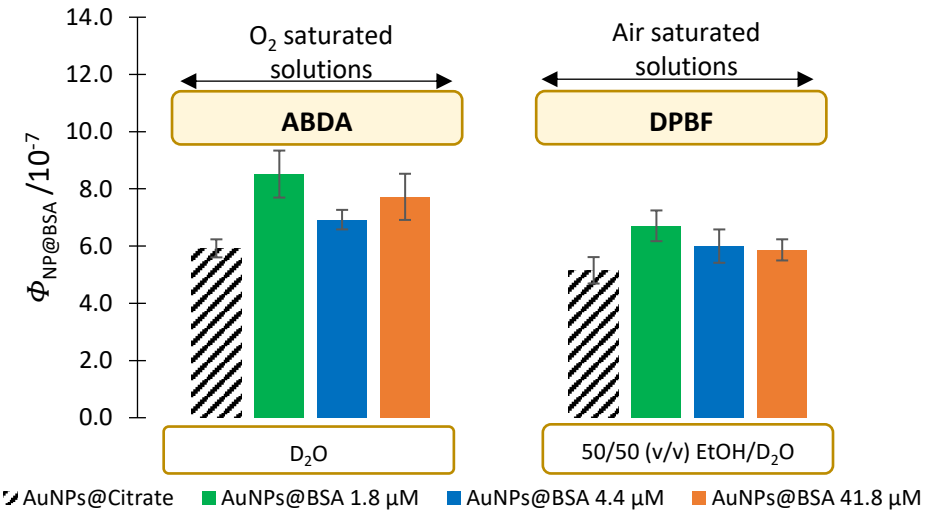

Figure 4.6 – Bar chart showing the $^1O_2$ quantum yield of AuNPs@ BSA incubated with different BSA concentrations, determined from a non-linear least-square fit of the absorbance change over time of both molecular probes, ABDA and DPBF. The irradiation of ABDA solutions in the presence of AuNPs@BSA was done in O_2-saturated (1 bar) D_2O solutions. The irradiation of DPBF solutions in the presence of AuNPs@BSA was done in air-saturated 50/50 (v/v) EtOH/D_2O solution mixtures. The error bars show the standard error.

The $^1O_2$ quantum yield of AuNPs functionalized with BSA upon CW-irradiation at 532 nm determined from the photobleach rate of ABDA in O_2-saturated D_2O solutions yielded a value of (8.5 ± 1.0) x 10^{-7}, (6.9 ± 0.4) x 10^{-7} and (7.7 ± 1.0) x 10^{-7}, for BSA incubation concentrations of 1.8, 4.4 and 41.8 µM, respectively.

In the case of DPBF, the $^1O_2$ quantum yield of AuNPs functionalized with BSA upon CW-irradiation at 532 nm in air-saturated 50/50 (v/v) EtOH/D_2O yielded a value of (6.7 ± 0.5) x 10^{-7}, (6.0 ± 0.6) x 10^{-7} and (5.9 ± 0.4) x 10^{-7}, for the BSA incubation concentration of 1.8, 4.4 and 41.8 µM respectively.

Table 4.2 – Table showing the $^1O_2$ quantum yield of AuNPs@ BSA incubated with different BSA concentrations, determined from a non-linear least-square fit of the absorbance change over time of both molecular probes, ABDA and DPBF. The irradiation of ABDA solutions in the presence of AuNPs@BSA was done in O_2-saturated (1 bar) D_2O solutions. The irradiation of DPBF solutions in the presence of AuNPs@BSA was done in air-saturated 50/50 (v/v) EtOH/D_2O solution mixtures.

	$\Phi_{NP@BSA}$ /10^{-7}	
	ABDA[a]	**DPBF[b]**
AuNPs@Citrate	5.9 (± 0.3)	5.2 (± 0.4)
AuNPs@BSA 1.8 µM	8.5 (± 1.0)	6.7 (± 0.5)
AuNPs@BSA 4.4 µM	6.9 (± 0.4)	6.0 (± 0.6)
AuNPs@BSA 41.8 µM	7.7 (± 1.0)	5.9 (± 0.4)

[a] in D_2O, O_2 saturated
[b] in 50/50 (v/v) EtOH/D_2O, air saturated

The irradiation of O_2-saturated D_2O solutions of ABDA in the presence of AuNPs functionalized with BSA yielded a $\Phi_{NP@BSA}$ ~30% higher when compared with the Φ_{NP} determined for the irradiation of AuNPs@Citrate. Statistical analysis (ANOVA f-test, p-value = 0.01) for these sets of results, i.e. $\Phi_{NP@BSA}$ and Φ_{NP}, marginally suggests that there is a significant difference between the results. Also, the $\Phi_{NP@BSA}$ determined for the AuNPs functionalized with BSA seems to be independent of the capping layer size tested. Statistical analysis (ANOVA f-test, p-value = 0.4) showed no statistically significant difference between the different $\Phi_{NP@BSA}$ determined upon irradiation of AuNPs incubated with different concentrations of BSA. The irradiation of air-saturated 50/50 (v/v) EtOH/D_2O solutions of DPBF in the presence of AuNPs functionalized with BSA also yielded a higher $\Phi_{NP@BSA}$ (~20%) when compared with the Φ_{NP} determined for the irradiation of AuNPs@Citrate. However, statistical analysis (ANOVA f-test, p-value = 0.3) suggest that the difference between the data sets is not significant.

Overall, it is reasonable to conclude that AuNPs@BSA generate $^1O_2$ with a similar $^1O_2$ quantum yield when compared to the Φ_{NP} obtained from the irradiation of AuNPs coated with a loosely bound citrate layer. As mentioned in section 4.1, BSA forms a porous corona with an irregular shape that does not form close packed layers on the surface of AuNPs (see Figure 4.1B).[16] Also, according to the literature, the BSA corona on AuNPs consists mainly of water (70%).[19] Therefore, is reasonable to suggest that the slight $\Phi_{NP@BSA}$ increase compared to Φ_{NP} is due a slightly better diffusion of O_2 to the surface of the AuNPs, hence increasing the available O_2 for $^1O_2$ generation by the Dexter mechanism

to occur. As described in section 3.3.2, a higher O_2 concentration in the close vicinity of the AuNP makes it more likely for $^1O_2$ generation by the Dexter mechanism to occur, hence increasing the $^1O_2$ yield.

Lastly, and most importantly, we showed that it is possible to tailor AuNPs with specific types of molecules maintaining (as shown here) their ability to generate $^1O_2$. We here used BSA because it simulates a possible capping layer formed when the "naked" AuNPs enter the bloodstream. However, the easy surface functionalization of AuNPs allow them to be tailored with more relevant biological molecules for specific biomedical applications.

4.5 Conclusion

The irradiation of 15.8 nm AuNPs@BSA with different capping layer densities at their SPR with CW laser light (532 nm) leads to the photogeneration of $^1O_2$, detected indirectly via the photobleach of ABDA and DPBF. The $\Phi_{\mathrm{NP@BSA}}$ is still very low when compared with the PSs used nowadays in clinical PDT. However, we proved for the first time, quantitatively and in aqueous solution, that AuNPs can be capped with biological molecules and, at the same time, retain their $^1O_2$ photogeneration efficiency.

Overall, our results broaden, even more, the potential application of AuNPs in PDT. Due to the easy functionalization of the AuNPs surface, the nanoparticles can be tailored to target specific cells and, afterwards, irradiated to generate $^1O_2$ to kill those cells.[20]

4.6 References

(1) Boulos, S. P.; Davis, T. A.; Yang, J. A.; Lohse, S. E.; Alkilany, A. M.; Holland, L. A.; Murphy, C. J. Nanoparticle–Protein Interactions: A Thermodynamic and Kinetic Study of the Adsorption of Bovine Serum Albumin to Gold Nanoparticle Surfaces. *Langmuir* **2013**, *29*, 14984.

(2) Hormozi-Nezhad, M. R.; Karami, P.; Robatjazi, H. A Simple Shape-Controlled Synthesis of Gold Nanoparticles Using Nonionic Surfactants. *RSC Adv.* **2013**, *3*, 7726.

(3) Glickman, R. D.; Millenbaugh, N. J.; Kirui, D.; Maswadi, S.; Thomas, R. J.; Oian, C. A. *Nanobiomaterials in Antimicrobial Therapy*; 1st Edition, Elsevier Oxford, **2016**.

(4) Gamaleia, N.; Shton, I. Gold Mining for PDT : Great Expectations from Tiny Nanoparticles. *Photodiagnosis Photodyn. Ther.* **2015**, *12*, 221.

(5) Wilson, R. The Use of Gold Nanoparticles in Diagnostics and Detection. *Chem. Soc. Rev.* **2008**, *37*, 2028.

(6) Thakor, S.; Jokerst, J.; Zavaleta, C.; Massoud, T. F.; Gambhir, S. S. Gold Nanoparticles: A Revival in Precious Metal Administration to Patients. *Nano Lett.* **2011**, *11*, 4029.

(7) Maiorano, G.; Sabella, S.; Sorce, B.; Brunetti, V.; Malvindi, M. A.; Cingolani, R.; Pompa, P. Effects of Cell Culture Media on the Dynamic Formation of Protein−Nanoparticle Complexes and Influence on the Cellular Response. *ACS Nano* **2010**, *4*, 7481.

(8) Mahon, E.; Salvati, A.; Bombelli, F.; Lynch, I.; Dawson, K. Designing the Nanoparticle–Biomolecule Interface for "Targeting and Therapeutic Delivery." *J. Control. Release* **2012**, *161*, 164.

(9) Gunawan, C.; Lim, M.; Marquis, C.; Amal, R. Nanoparticle–Protein Corona Complexes Govern the Biological Fates and Functions of Nanoparticles. *J. Mater. Chem. B* **2014**, *2*, 2060.

(10) Wang, F.; Yu, L.; Monopoli, M. P.; Sandin, P.; Mahon, E.; Salvati, A.; Dawson, K. A. The Biomolecular Corona Is Retained during Nanoparticle Uptake and Protects the Cells from the Damage Induced by Cationic Nanoparticles until Degraded in the Lysosomes. *Nanomedicine Nanotechnology, Biol. Med.* **2013**, *9*, 1159.

(11) Brandes, N.; Welzel, P.; Werner, C.; Kroh, L. Adsorption-Induced Conformational Changes of Proteins onto Ceramic Particles: Differential Scanning Calorimetry and FTIR Analysis. *J. Colloid Interface Sci.* **2006**, *299*, 56.

(12) Giménez, R. E.; Vargová, V.; Rey, V.; Turbay, M.; Abatedaga, I.; Morán Vieyra, F. E.; Paz Zanini, V. I.; Mecchia Ortiz, J. H.; Katz, N. E.; Ostatná, V.; Borsarelli, C. D.; Interaction of Singlet Oxygen with Bovine Serum Albumin and the Role of the Protein Nano-Compartmentalization. *Free Radic. Biol. Med.* **2016**, *94*, 99.

(13) Era, S.; Sogami, M. ^{1}H-NMR and CD Studies on the Structural Transition of Serum Albumin in the Acidic Region-The N→F Transition. *J. Pept. Res.* **2009**, *52*, 431.

(14) Bujacz, A.; Structures of Bovine, Equine and Leporine Serum Albumin. *Acta*

Crystallogr. Sect. D Biol. Crystallogr. **2012**, *68*, 1278.

(15) Humphrey, W.; Dalke, A.; Schulten, K. VMD: Visual Molecular Dynamics. *J. Mol. Graph.* **1996**, *14*, 33.

(16) Davidson, A. M.; Brust, M.; Cooper, D. L.; Volk, M. Sensitive Analysis of Protein Adsorption to Colloidal Gold by Differential Centrifugal Sedimentation. *Anal. Chem.* **2017**, *89*, 6807.

(17) Chadwick, S. J.; Salah, D.; Livesey, P. M.; Brust, M.; Volk, M. Singlet Oxygen Generation by Laser Irradiation of Gold Nanoparticles. *J. Phys. Chem. C* **2016**, *120*, 10647.

(18) Krpetić, Ž.; Davidson, A. M.; Volk, M.; Lévy, R.; Brust, M.; Cooper, D. L. High-Resolution Sizing of Monolayer-Protected Gold Clusters by Differential Centrifugal Sedimentation. *ACS Nano* **2013**, *7*, 8881.

(19) Belsey, N. A.; Shard, A. G.; Minelli, C. Analysis of Protein Coatings on Gold Nanoparticles by XPS and Liquid-Based Particle Sizing Techniques. *Biointerphases* **2015**, *10*, 19012.

(20) Niidome, T.; Yamagata, M.; Okamoto, Y.; Akiyama, Y.; Takahashi, H.; Kawano, T.; Katayama, Y.; Niidome, Y. PEG-Modified Gold Nanorods with a Stealth Character for in Vivo Applications. *J. Control. Release* **2006**, *114*, 343.

Chapter 5

5. Conclusion

On the basis of the work presented in the previous chapters, we have concluded that;

i) ABDA and DPBF have both the capability to detect $^1O_2$ accurately under the right conditions. DPBF is significantly more sensitive but suffers from chemical and light instability and is insoluble in neat aqueous conditions. On the other hand, ABDA can be used in fully aqueous solvents and it is easier to work with, making it an ideal candidate when $^1O_2$ evaluation requires harsher conditions; however, it is less sensitive, so requires longer irradiation time for detecting $^1O_2$ with the same accuracy.

ii) The rate constants (k_r) determined in this thesis from a coherent set of data for ABDA and DPBF allow an accurate determination of the quantum efficiency of new PSs.

iii) We have confirmed conclusively for the first time, using ABDA as the sensor, that CW-irradiation of AuNPs generates $^1O_2$.

iv) CW-irradiation of AuNPs generates $^1O_2$ with a very small quantum yield when compared with PSs used nowadays in clinical practice. However, the small quantum efficiency is compensated by the extremely large extinction coefficient.

v) DPBF photobleach results further suggest that AuNPs can generate other ROS as well.

vi) Capping AuNPs with BSA did not hinder the $^1O_2$ photogeneration efficiency when compared with the AuNPs@Citrate.

Despite the small $^1O_2$ QY of AuNPs determined in this thesis, the use of AuNPs as PDT agents is promising therefore, a future consideration would be the evaluation of different AuNPs with different sizes and shapes and evaluate their $^1O_2$ photogeneration

efficiency. Additionally, pursuing a better stability of AuNPs in a biological environment, AuNPs could be functionalized with different capping layers, varying the length and capping layer density. Finally, this project could also advance to experiments to further investigate the uses of AuNPs in PDT; AuNPs could be functionalized with more relevant biomolecules for cancer therapy and the $^1O_2$ photogeneration efficiency of the functionalized AuNPs evaluated.

Appendix 1

Irradiation of AuNPs with CW laser light has been shown to photogenerate $^1O_2$ with an unquestionably small quantum yield. Hence, it was necessary to carefully plan not only the irradiation experiments but also the sample preparation and handling. Here, we will discuss several crucial experimental design issues which were found to affect the results significantly.

The design of the experimental methods and optimised protocol presented in chapters 2 and 3 are the results of several improvements that arose from research issues that we faced during the last three years. Therefore, this appendix aims to describe how to carefully get accurate data from the irradiation experiments, especially when the amount of $^1O_2$ photogenerated over time is so small.

A1.1 Issues with sample preparation and handling

One of the most significant difficulties we faced during the irradiation experiments was the reproducibility of the results, especially when the molecular probes are not chemically or light stable, such as DPBF. We found that cell and stir bar maintenance and cleanliness are of utter importance.

The cuvettes and the stir bars had to be cleaned regularly with aqua regia (1:3 HNO_3:HCl) for half an hour and rinsed twice with soapy tap water. The cuvettes and stir bars were then further rinsed thoroughly multiple times (35 to 40) with Milli-Q water. After the thorough cleaning process, the cuvettes and stir bars were left overnight in Milli-Q water. Before use, the cuvettes and stir bars were rinsed with ethanol twice and left to dry. At this point, if the molecular probe to be used was DPBF, no further rinsing was necessary. On the other hand, if the molecular probe to be used was ABDA, the cuvettes and stir bars were rinsed with H_2O or D_2O, according to the solvent to be used in the experiment and left to dry. This aggressive cleaning process ensured that all impurities from previous experiments were removed, which allows the probe solution to be more stable.

We found that the irradiation of solutions that included AuNPs required the stir bar to be pre-coated with them, by incubation in a AuNPs solution for 15 minutes after the cleaning process. Figure A1. 1 A, B and C shows the absorbance spectra of AuNPs solutions in the absence of molecular singlet oxygen probes upon CW-irradiation at 532 nm with an irradiation power of 1 W in a freshly cleaned cuvette and varying the stir bar cleanliness conditions. For an easier comparison, the variation of the normalised absorbance of AuNPs at 520 nm over time upon irradiation is shown in D.

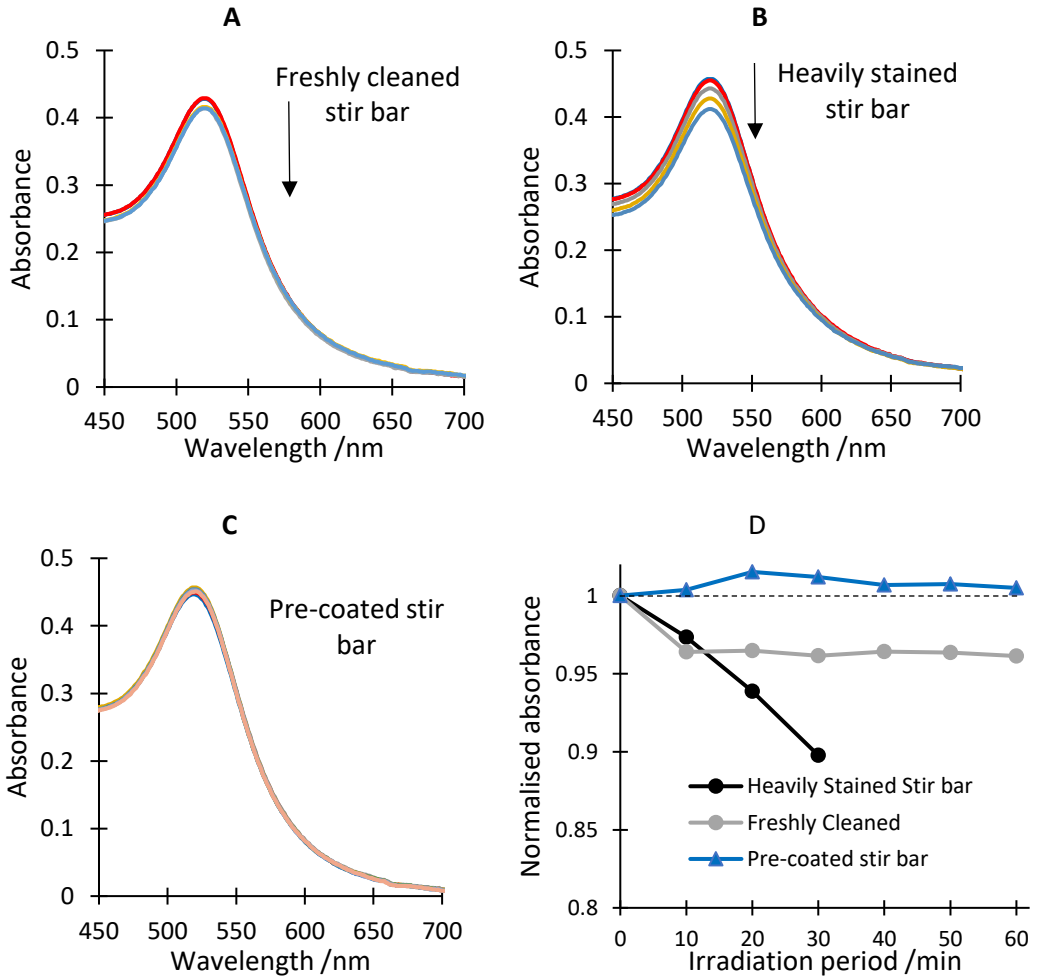

Figure A1. 1 – Absorbance spectra of AuNPs solutions in H_2O upon CW-irradiation at 532 nm, 1 W, in a freshly cleaned cuvette, using A) a freshly cleaned stir bar (1 hour of irradiation), B) a heavily gold-stained stir bar (30 minutes of irradiation) and C) a pre-coated AuNPs stir bar (1 hour irradiation). The absorbance spectra of AuNPs were taken with 10 minutes intervals. The arrow indicates the direction of change. D) Variation of the AuNPs absorbance at 520 nm, normalised at 0 min, for the irradiation conditions stated before for the spectra A, B and C. In D) the dashed line shows a line at y=1 as a guide to the eye.

The irradiation of AuNPs solutions in a freshly cleaned cuvette and stir-bar was observed to lead to a slight decrease of the AuNPs absorbance in the first 10 minutes of irradiation. After this period, the AuNPs absorbance remained stable throughout the remaining irradiation time (50 minutes), as shown in Figure A1.1 – A and D. In contrast, Figure A1.1 – B shows the irradiation of the same AuNPs solution using a heavily red-stained stir bar. As shown, a continuous decrease of the AuNPs absorption was observed throughout the irradiation period (Figure A1.1 – D). Note that the SPR band did not broaden, only decreased, which suggests that the AuNPs are precipitating, not aggregating. Figure A1.1 – C shows the irradiation of the AuNPs solution in a freshly cleaned cuvette after the 15 minutes "coating" process. No absorbance change of the SPR was observed (Figure A1.1 – D). Note that there is no visual difference between a freshly cleaned stir bar and a AuNPs pre-coated stir bar. Additionally, we found that upon continuous use of AuNPs solutions, AuNPs tend to attach to the surface of the stir bar, as well as to the walls of the cuvette. This effect is particularly visible if the cuvette and stir bar is in continuous contact with AuNPs solutions for more than 24 hours. After this period, both the cuvette and stir bar is visually red.

Overall, it is essential to highlight that when the cleaning process was not strictly followed, the results were not reproducible.

A1.2 Solvent quality

The solvent quality was also an issue, and it contributes significantly to the chemical stability of the $^1O_2$ molecular probes. All DPBF, ABDA or AuNPs solutions were prepared with high purity solvents (EtOH and D_2O ACS analytical grade) or fresh MQ H_2O. Figure A1.2 shows the variation of DPBF absorbance upon CW-irradiation at 532 nm with an intensity of 1 W, in a 50/50 (v/v) EtOH/H_2O solution prepared with drum ethanol (A) and ACS analytical grade ethanol (B). Note that these irradiation experiments were done in the absence of cut-off filter GG375 (see chapter A1.3 for the effect of this filter).

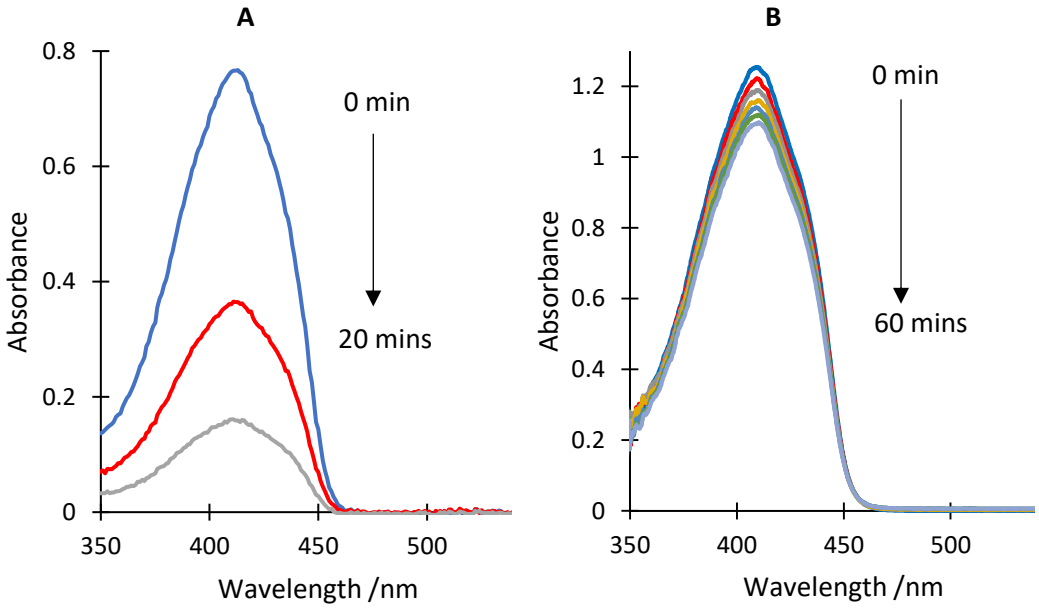

Figure A1. 2 - Photobleach of DPBF absorbance upon CW-irradiation at 532 nm, 1 W, in 50/50 (v/v) EtOH/H_2O air-saturated solution (in the absence of cut-off filter GG375). Absorbance spectra of DPBF were taken with 10 minutes intervals. A) solution prepared with drum ethanol (irradiation period of 20 minutes) and B) solution prepared with ACS analytical grade ethanol (irradiation period of 60 minutes). The arrows indicate the direction of absorbance change over time.

As shown (Figure A1.2 - A), the CW-irradiation of DPBF solutions prepared with drum ethanol was observed to induce a large decrease of the DPBF absorbance. The absorbance of DPBF decreased ~ 80% over an irradiation period of 20 minutes. In comparison (Figure A1.2 - B), under the same irradiation conditions, the DPBF absorbance of DPBF solutions prepared with ACS analytical grade ethanol only decreased ~ 13% over an irradiation period of 1 hour. Note that only under the latter conditions (Figure A1.2 – B), the DPBF photobleach was reproducible.

A1.3 Harmonic output from the laser

One of the main questions that always puzzled us was why DPBF and ABDA self-photobleach when irradiated with 532 nm CW laser light in the absence of AuNPs. DPBF does not appear to have any significant absorbance at 532 nm (see Figure A1.2), and ABDA does not absorb at all at 532 nm (see Figure A1.3). Figure A1.3 shows the variation

of ABDA absorbance in air-saturated D_2O, upon CW-irradiation at 532 nm with an intensity of 3 W in the absence of a cut-off filter.

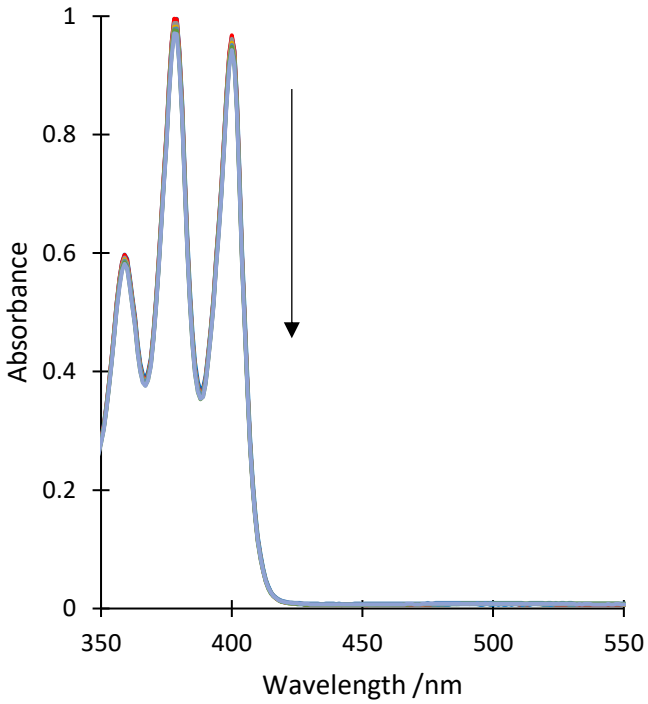

Figure A1. 3 – Photobleach of ABDA absorbance upon CW-irradiation at 532 nm, 3 W, in D_2O air-saturated solutions, in the absence of cut-off filter GG375. Absorbance spectra of ABDA were taken with 10 minutes intervals. The arrow indicates the absorbance change over time.

Upon irradiation, a slight decrease of the ABDA absorbance was observed (see Figure A1. 4), and even more in DPBF, see Figure A1.2 B. Following this observation, we investigated the possibility of the generation of harmonic light in the laser. The OPUS532 laser is running at 1064 nm and generates the 532 nm wavelength with an intracavity doubling crystal, i.e. there is a nonlinear crystal present which doubles the original light to 532 nm. We tested the hypothesis by placing a Schott GG375 cut-off filter between the sample and laser source to eliminate any light at wavelengths below 375 nm, repeating the irradiation experiments of ABDA solutions in the absence of AuNPs and comparing the results to those obtained in the absence of the filters.

Figure A1.4 shows the variation of the absorbance of ABDA at 398 nm upon CW-irradiation, with an intensity of 3 W, normalised to the absorbance before irradiation, in the absence of AuNPs, in the presence and absence of a cut-off filter GG375.

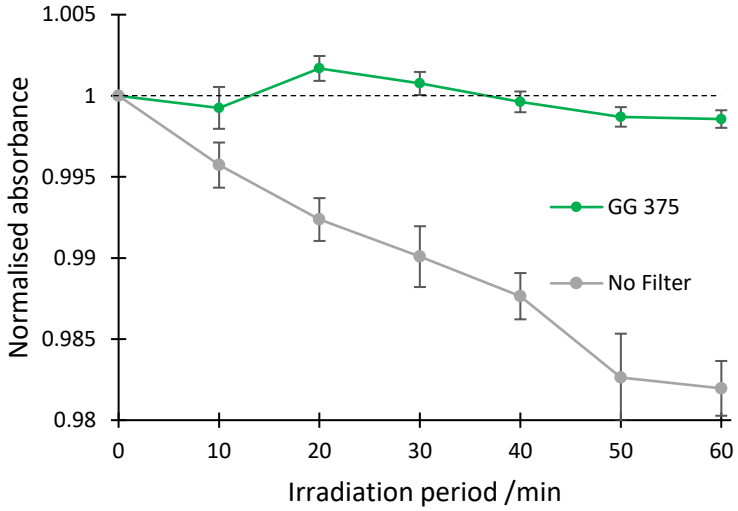

Figure A1. 4 – Variation of the ABDA absorbance at 398 nm, normalised at 0 minutes, upon CW-irradiation at 532 nm, 3 W, in air-saturated D_2O in the presence (solid green line – an average of fourteen experiments) and absence of a GG375 cut-off filter (solid grey line – an average of 8 experiments). The error bars represent the standard error of the experiment obtained from the standard deviation of several repeat experiments divided by the square root of the number of repeat experiments. The dashed line shows a line at y=1 as a guide to the eye.

No direct photodegradation of ABDA was observed upon CW-irradiation with an irradiation power of 3 W when the cut-off filter was used. The ABDA absorbance did not change as the irradiation progressed. In contrast, in the absence of the cut-off filter, a decrease of the ABDA absorbance by ~ 2% was observed. Our experimental results show that the laser setup was undoubtedly generating harmonic light, which we were able to block by using cut-off filters during the irradiation experiments. A theoretical calculation showed that an amount of 266 nm light as small as 0.02 mW when running the laser at 3W at 532 nm, would be enough to cause the observed ABDA photobleach in the absence of the cut-off filter (A_{ABDA}=2 at 266 nm), assuming that each absorbed photon leads to an ABDA molecule degradation. My supervisor, Dr Martin Volk, queried the manufacturer who did not rule out this possibility.

The irradiation experiments in the presence and absence of a cut-off filter were repeated for DPBF. Figure A1.5 shows the variation of the normalised absorbance of DPBF at 410 nm upon CW-irradiation, with an intensity of 1 W, in the presence and absence of the cut-off filter GG375.

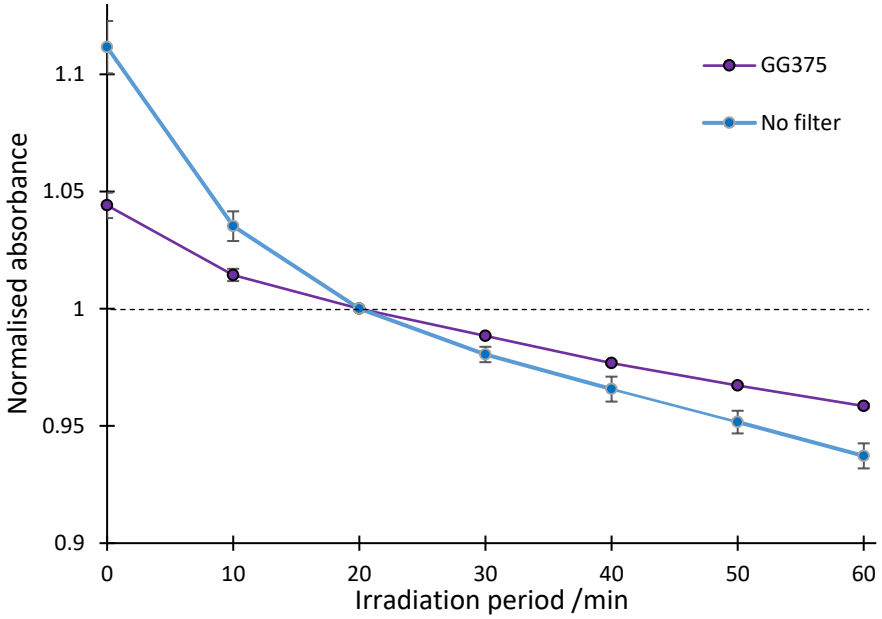

Figure A1. 5 – Variation of the DPBF absorbance at 410 nm, normalised at 20 minutes, upon CW-irradiation at 532 nm, 1 W, in air-saturated 50/50 (v/v) EtOH/H_2O, in the absence (blue solid line – average of five measurements) and presence of a GG375 cut-off filter (purple solid line – average of seven experiments). The error bars represent the standard error of the experiment obtained from the standard deviation of several repeated experiments divided by the square root of the number of repeated experiments. The dashed line shows a line at y=1 as a guide to the eye.

A clear decrease in the DPBF photobleach was observed even when the cut-off filter was used. The DPBF photobleach in the reproducible phase (20-60 min) decreased by ~ 35% when compared to the DPBF photobleach in the absence of a cut-off filter. Despite the reduction of the photobleaching effect, DPBF still photobleached in the presence of the cut-off filter. For further details, see section 3.3.2.1.

A1.4 Temperature effect

Another issue that needed to be considered that was causing reproducibility problems was the temperature. As stated before, ABDA does not absorb, and DPBF has only a very small residual absorbance at 532 nm. Consequently, no variation of the solution temperature was observed when ABDA and DPBF were irradiated in the absence of AuNPs. However, this is not true when solutions containing AuNPs are irradiated. Upon irradiation of the AuNPs solution, the electrons in the free electron cloud of AuNPs are

excited by light and, after the fast relaxation process of AuNPs described in section 1.2.3.2 (see Figure 1.8), the majority of the energy is going to be released to the solvent as heat.

Figure A1.6 shows the variation of the solution temperature over time while irradiating a solution of AuNPs with an absorbance of 0.4 at 532 nm with CW-irradiation with a power of 3 W, with and without a water bath, consisting of a three by two cm quartz container filled with room temperature water. The temperature was measured by placing a temperature probe (Picolog TC-08 with a thermocouple) inside the solution while being irradiated. Note that the probe was not in the laser beam path.

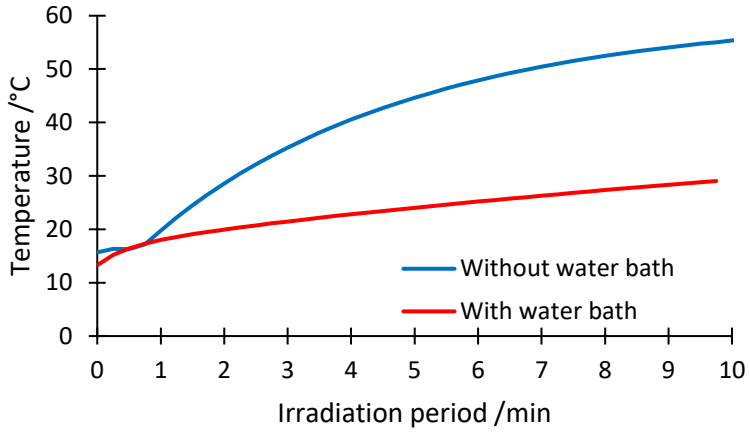

Figure A1. 6 – Variation of the solution temperature over time upon irradiation of AuNPs solutions with an absorbance of 0.4 at 532 nm with CW-irradiation at 532 nm, 3 W, with (solid red line) and without (solid blue line) water bath. Temperature measured with a temperature probe inside the solution while being irradiated.

As expected, the irradiation of AuNPs over a period of 10 minutes resulted in an increase of the solution temperature. The temperature of AuNPs solution irradiated while in the water bath increased by 14 °C over an irradiation period of 10 minutes. In comparison, the temperature of AuNPs solution irradiated without the water bath increased by 44 °C over the same time. Overall, our results showed clearly that the water bath significantly helps to control the temperature of the sample upon CW-irradiation.

Additionally, we also found that the variation of the temperature changed the extinction coefficient of ABDA slightly, which increased the uncertainty of the measurement. Figure A1.7 – A shows the variation of the normalised ABDA absorbance at 398 nm of an air-saturated solution in D_2O in the presence of AuNPs upon CW-irradiation with an irradiation power of 3 W, without a water bath. Note that the red dots show the normalised absorbance of ABDA at 398 nm measured deliberately straight after

each irradiation interval was finished, while the solution was still warm. The blue dots show the normalised absorbance of ABDA at 398 nm taken after the solution was allowed to cool down to room temperature.

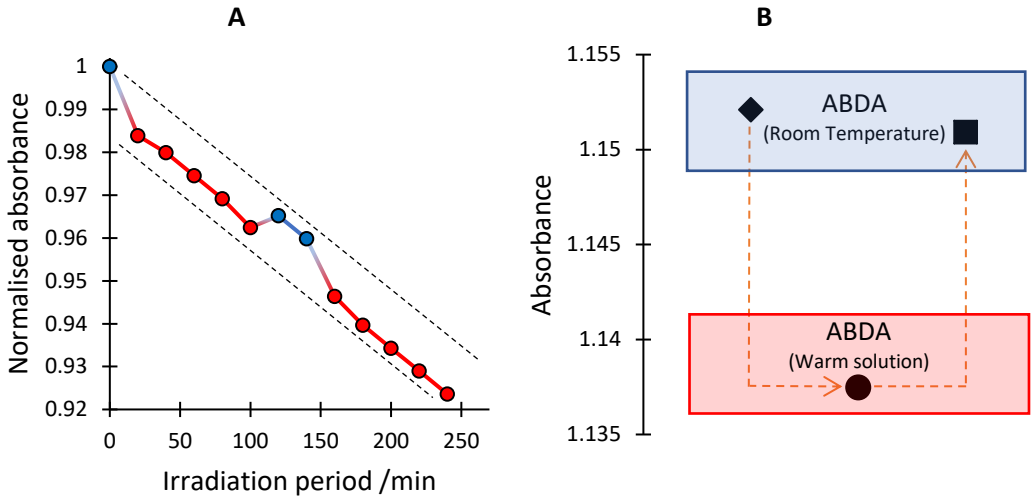

Figure A1. 7 – A) Variation of the ABDA absorbance at 398 nm, normalised to the absorbance before the irradiation, of an air-saturated solution in D_2O in the presence AuNPs upon CW-irradiation, 3 W, in the absence of a water bath. Absorbance spectra of ABDA were taken with 20 minutes intervals to a maximum irradiation period of 240 minutes. The red points show the normalised absorbance of ABDA measured as soon as the irradiation interval finished, while the solution was still warm. The blue points show the normalised absorbance of ABDA measured after waiting for the solution to cool down to room temperature after these irradiation intervals. Dashed lines highlight the linearity of the photobleaching. B) Absorbance variation (at 398 nm) of the same ABDA solution due to temperature; the solution was always kept in the dark stirring throughout the entire experiment ◆- ABDA solution just prepared ●- ABDA solution warmed up to 60 °C♣♣ ■- ABDA solution after cooling down to room temperature.

Our results showed a significant "apparent" drop of the ABDA absorbance during the first 20 minutes of irradiation in the presence of AuNPs (Figure A1.7 – A). After the first 20 minutes up to 100 minutes of irradiation, the ABDA photobleach in the presence of AuNPs was linear as the time progressed, as highlighted by the dashed lines. After 120 minutes of sequential irradiation, the warm ABDA solution with AuNPs was allowed to cool down to room temperature and only then the UV-Vis spectrum was measured. The same procedure was repeated for the following 20 minutes of irradiation (the point at 140 minutes). Note that the first point (the point at t = 0 minutes) and the points at t = 120 and 140 minutes (blue points) show the same photobleach linearity as the red points, as highlighted by the dashed lines. To further confirm the temperature effect, the remaining irradiation period was repeated following the protocol used during the first

♣♣ - The heat stirring plate was set to 60 °C.

100 minutes of irradiation. The same linearity of ABDA photobleach observed during the absorbance points between 20 and 100 minutes was observed for the last 80 minutes of irradiation (absorbance points between 160 and 240 minutes).

Our results suggest that the temperature was causing the extinction coefficient of ABDA to change slightly. To further investigate and confirm this effect, an ABDA solution in the absence of AuNPs were prepared, and the temperature effect investigated. Figure A1.7 – B shows the absorbance variation of the same ABDA solution due to temperature. Note that during this procedure, the ABDA solution was always kept in the dark stirring. An ABDA solution was prepared in a cuvette, and the UV-Vis spectrum was taken (◆). The cuvette was then placed on a hot stirring plate set to 60 °C for 20 minutes to warm up the solution. While still warm, a UV-Vis spectrum was re-measured (●). Afterwards, the solution was allowed to cool down to room temperature, and a final UV-Vis spectrum was measured (■). This experiment showed clearly that the extinction coefficient decreased by ~1.5% for a temperature increase of 40 °C, which is very similar to the effect suggested by the experimental results shown in Figure A1.7 – A.

Overall, our experimental results show that the "apparent" absorbance variation observed during the irradiation of ABDA in the presence of AuNPs (Figure A1.7 – A) is due to the variation of the temperature in the solution mixture. To overcome this issue, the samples were kept for 10 minutes in the dark after each irradiation interval to allow them to cool down to room temperature. Additionally, it is also reasonable to conclude that there is no decomposition of the endoperoxide♣ due to the temperature.[1]

A1.5 Oxygen concentration

The oxygen concentration in the solutions was another issue that needed to be considered. As shown in Chapter 3, the photogeneration of $^1O_2$ by AuNPs upon irradiation

♣ - The ABDA endoperoxide generated upon the reaction of $^1O_2$ with ABDA can be rapidly decomposed by cycloreversion, trigged by temperature.[1] The decomposition is observed upon heating the solution with temperatures above 60 °C. The half-live of anthracene 9,10-endoperoxides are typically years at room temperature.[1]

[1] - Kolemen, S.; Ozdemir, T.; Lee, D.; Kim, G. M.; Karatas, T.; Yoon, J.; Akkaya, E. U. Remote-Controlled Release of Singlet Oxygen by the Plasmonic Heating of Endoperoxide-Modified Gold Nanorods: Towards a Paradigm Change in Photodynamic Therapy. *Angew. Chemie - Int. Ed.* **2016**, *55*, 3606.

depends on the O_2 dissolved in the solution mixture (see Figure 3.15). The O_2 solubility in EtOH is ~ 6 times higher when compared with H_2O or D_2O.[2] However, upon mixing, the resulting ethanolic mixture becomes supersaturated due to a non-linearity of the solubility-concentration curve, as reported by Pan *et al.*.[2]

Therefore, to evaluate the supersaturation effect in our irradiation experiments, DPBF solutions were irradiated after different equilibration periods, and the DPBF photobleach compared. Figure A1.8 shows a comparison between the photobleach of DPBF in 50/50 (v/v) EtOH/H_2O in the absence of AuNPs when irradiated just after mixing EtOH with H_2O, or after letting the solution mixture equilibrate while stirring for different time lengths (1, 2 and 3 hours).

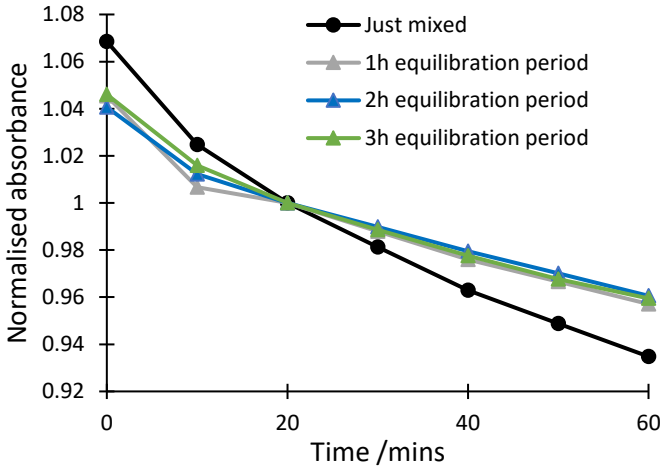

Figure A1. 8 - Time-dependent photobleach of the normalised DPBF absorbance at 410 nm (in the absence of AuNPs), CW-irradiation at 532 nm, 1 W, in air-saturated 50/50 (v/v) EtOH/H_2O, just after mixing EtOH with H_2O and after 1, 2 and 3 hours of equilibration period.

As shown, the supersaturated mixture of EtOH/H_2O (just mixed) showed an increased photobleach of DPBF in both irradiation phases when compared with all equilibrated samples. After 1 hour of equilibration period, the DPBF photobleach observed for all samples across the 3 hours equilibration period was similar and reproducible.

[2] - Pan, G.; Yang, B. Effect of Surface Hydrophobicity on the Formation and Stability of Oxygen Nanobubbles. *ChemPhysChem* **2012**, 13, 2205.

Appendix 2

A2.1 – Derivation of equation (Chapter 2, Equation 2.5)

Since the lifetime of $^1O_2$ is very short compared to the experimental time scale (minutes) on which the sensor concentration [S] changes, the steady-state concentration of $^1O_2$ at any given time *t* can be calculated by equating the rates of its photogeneration and its decay via solvent quenching or reaction with a sensor molecule (all parameters as defined in the main text):

$$\frac{N_{\text{abs}}\Phi_{\text{RB}}}{VN_{\text{A}}} = \left[k_0 + (k_{\text{r}} + k_{\text{q}})[\text{S}]\right][^1\text{O}_2]_{\text{ss}} \qquad \text{(S1) = (2.3)}$$

Using this steady-state concentration of $^1O_2$ from yields the rate of bleach of sensor S due to reaction with $^1O_2$:

$$\frac{d[S]}{dt} = -k_{\text{r}}[S][^1\text{O}_2] = -k_{\text{r}}[S]\frac{N_{abs}\Phi_{RB}}{VN_A\left[k_0 + (k_{\text{r}} + k_{\text{q}})[\text{S}]\right]} \qquad \text{(S2) = (4)}$$

In this equation, the sensor concentration [S] can be replaced by the (time-dependent) absorbance $A = \varepsilon d[\text{S}]$:

$$\frac{dA}{dt} = \varepsilon d\,\frac{d[S]}{dt} = -k_r A\frac{N_{\text{abs}}\Phi_{\text{RB}}}{VN_{\text{A}}(k_0 + (k_{\text{r}} + k_{\text{q}})\frac{A}{\varepsilon d})} = -A\frac{\varepsilon dN_{\text{abs}}\Phi_{\text{RB}}}{VN_{\text{A}}(\varepsilon d\frac{k_0}{k_{\text{r}}} + \frac{k_{\text{r}} + k_{\text{q}}}{k_{\text{r}}}A)} = -\frac{A}{C_1(C_2 + C_3A)} \qquad \text{(S3)}$$

where $C_1 = \frac{VN_{\text{A}}}{\varepsilon dN_{\text{abs}}\Phi_{\text{RB}}}$, $C_2 = \frac{\varepsilon dk_0}{k_{\text{r}}}$, and $C_3 = \frac{k_{\text{r}} + k_{\text{q}}}{k_{\text{r}}}$

Equation (S3) yields the following differential equation:

$$\frac{C_1(C_2 + C_3A)}{A}dA + dt = 0 \qquad \text{(S4)}$$

Equation (S4) can be solved by direct integration:

$$0 = \int_{A_0}^{A(t)} \frac{C_1(C_2 + C_3 A)}{A}\, dA + \int_0^t dt = C_1 C_2 \ln\frac{A(t)}{A_0} + C_1 C_3 (A(t) - A_0) + t \qquad \text{(S5)}$$

Equation (S5) can be re-arranged to yield Equation 2.5:

$$t = C_1\left(C_2 \ln\frac{A_0}{A(t)} + C_3[A_0 - A(t)]\right) \qquad \text{(S6) = (2.5)}$$

Table A2. 1 - Rate constant k_r for deactivation of $^1O_2$ by a chemical reaction with $^1O_2$ sensor and resulting $^1O_2$ sensitivity Φ_S at sensor concentrations corresponding to a maximum absorbance of 1, for ABDA and DPBF in different solvents, obtained from the data points using fits (equation 2.5) under the assumption of different values of parameter $C_3 = (k_r + k_q)/k_r$. The highlighted results are those reported in the main text.

$^1O_2$ sensor	solvent	C_3						
		1	1.1	1.2	1.35	1.6	2	2.5
		k_r (10^7 $M^{-1}s^{-1}$)						
ABDA[a]	H_2O	5.60	5.60	5.61	5.63	5.65	5.68	5.73
	D_2O	3.89	3.89	3.92	3.98	4.07	4.24	4.47
	EtOH/D_2O[b]	2.75	2.77	2.78	2.79	2.82	2.87	2.93
DPBF	EtOH/H_2O[b]	283	302	323	361	450	751	2600[c]
	EtOH/D_2O[b]	231	272	332	493	2900[c]	-451[d]	-182[d]
		Φ_S						
ABDA[a]	H_2O	0.0192	0.0192	0.0192	0.0192	0.0192	0.0191	0.0191
	D_2O[e]	0.183	0.180	0.178	0.175	0.171	0.164	0.157
	EtOH/D_2O[b, e]	0.0501	0.0501	0.0500	0.0499	0.0498	0.0495	0.0492
DPBF	EtOH/H_2O[b]	0.449	0.444	0.439	0.432	0.421	0.406	0.380
	EtOH/D_2O[b, e]	0.722	0.701	0.681	0.653	0.613	0.555	0.498

[a] ABDA samples contained 1% (v/v) DMSO.
[b] 50/50 (v/v).
[c] this result for k_r is unphysical since it is significantly larger than the maximum diffusion-limited reaction rate constant, compare the Discussion (section 2.3.5) of the main text. It is included here only for the sake of completeness.
[d] for large values of C_3, the fits of the DPBF data in EtOH/D_2O do not result in satisfactory results, see Figure A2.4, and yield a negative rate constant; this unphysical result is based on the fact that for $C_3 > 2$, i.e. $k_q > k_r$, the maximum theoretically possible value of Φ_S is 0.5, which is significantly smaller than the experimentally observed value as analysed by Equation 2.2. As discussed in the main text, the literature confirms that for DPBF $k_q < 0.1\ k_r$, so this physically impossible result for k_r is reported here only for the sake of completeness.
[e] assuming neat solvents, *i.e.* no contamination by H_2O.

A2.2 – Additional figures

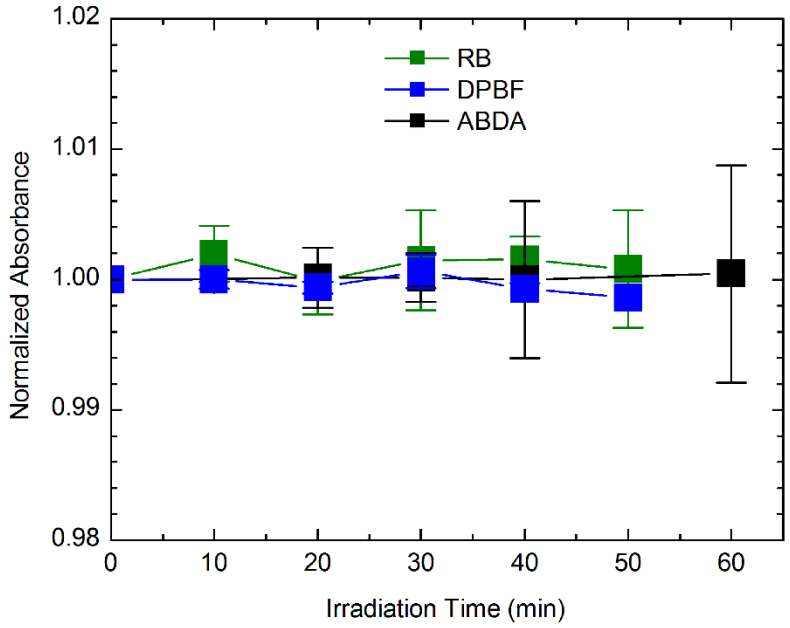

Figure A2. 1 - Photostability of RB, DPBF and ABDA upon irradiation when used separately. Shown here is the absorbance of RB in H_2O at 552 nm (green), DPBF in 50/50 (v/v) EtOH/H_2O at 411 nm (blue), and ABDA in D_2O at 400 nm (black), during irradiation with 0.14 mW CW laser light at 532 nm, normalised to the absorbance at the start of the irradiation, averaged over several repeat experiments; the error bars were calculated from the standard deviations for the individual experiments.

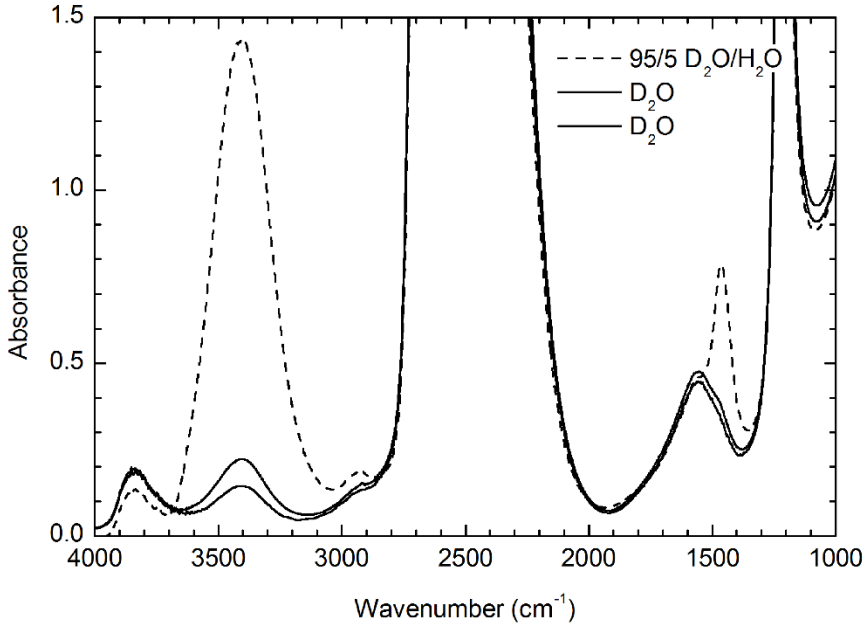

Figure A2. 2 - FTIR spectra of different D_2O batches and of a sample of D_2O to which H_2O (5% v/v) had been added explicitly, measured in a 50 µm pathlength IR cell with CaF_2 windows, using a BioRad FTS-40 spectrometer.

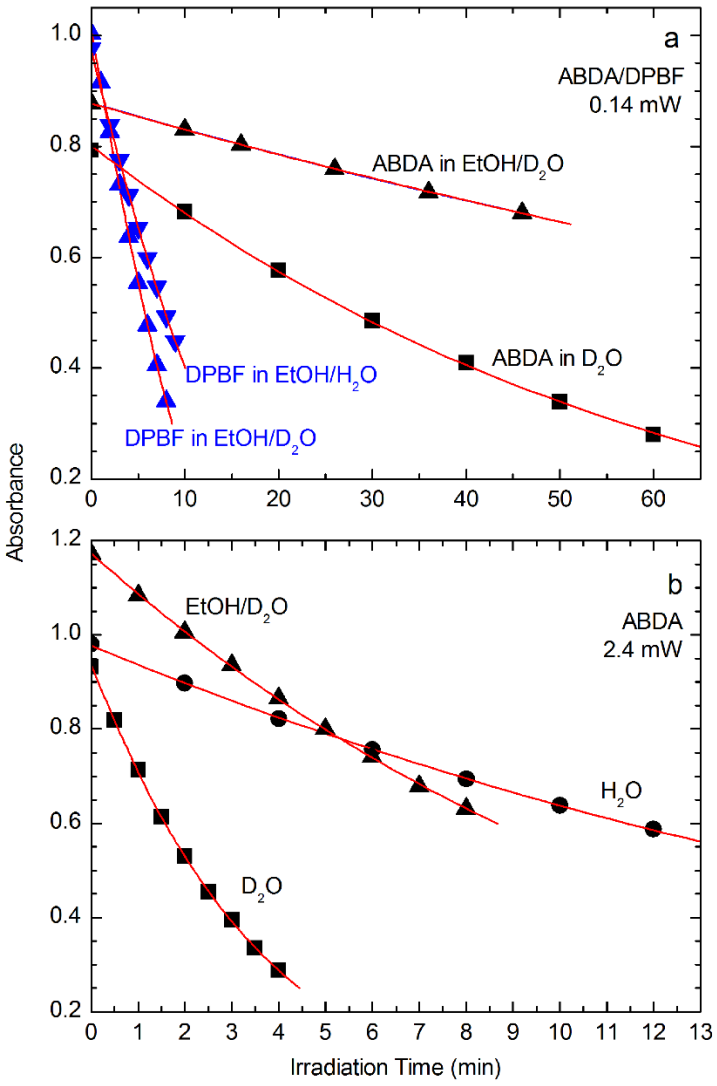

Figure A2. 3 – Example results of the photobleaching of ABDA (black) and DPBF (blue) in different solvents upon irradiation with 0.14 mW (a) or 2.4 mW (b) CW laser light at 532 nm in the presence of photosensitiser RB; shown here is the sensor absorbance at 398-400 nm (ABDA) or 410-412 nm (DPBF); the concentration of RB (~2 – 4 µM) varied sligltly from sample to sample, and hence the amount of photogenerated $^1O_2$, varied between the different curves, so that they are quantitatively not fully comparable; mixed solvents are 50/50 (v/v) mixtures. The red lines are fits of the data to Equation 2.5, where Parameter C_1 was calculated from the experimental parameters, the sensor extinction coefficient (Table 2.3) and the $^1O_2$ quantum yield of RB, Parameter C_3 was set to 1.35 (ABDA) or 1 (DPBF), as justified in the main text, and C_2 and A_0 were the free fit parameters. It should be noted that, unlike Figure 2.3, Figure A2.3 shows the time-dependent absorbance measured in individual experiments without any normalisation, as required for the application of Equation 2.5.

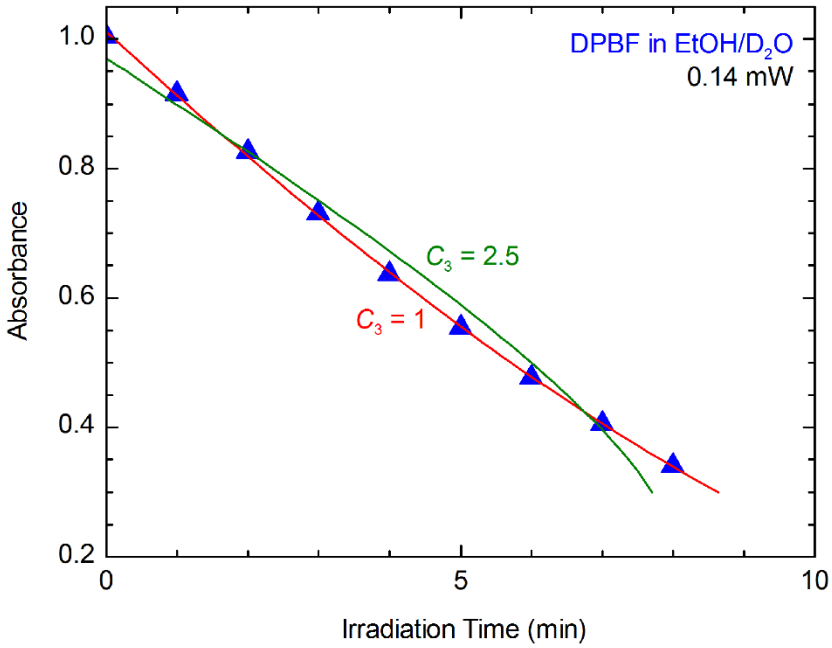

Figure A2. 4 - Fits of the example results of the photobleaching DPBF in 50/50 (v/v) EtOH/D_2O upon irradiation with 0.14 mW CW laser light at 532 nm in the presence of photosensitiser RB; shown here is the sensor absorbance at 410-412 nm (DPBF). The red line is the fit of the data to Equation 2.5 with Parameter C_3 set to 1, the green line the fit with C_3 = 2.5. Parameter C_1 was calculated from the experimental parameters, the sensor extinction coefficient (Table 2.3) and the $^1O_2$ quantum yield of RB, as justified in the main text, and C_2 and A_0 were the free fit parameters.

Appendix 3

A3.1 – Integration of Equation 3.2

Equation 3.2

$$P(x) = LP\ x\ 10^{\frac{-Ax}{d}}$$

Integrate P(x) from 0 to d,

$$< P >= \int \frac{P(x)}{d} dx = \frac{1}{d}\int P(x)\, dx = \frac{1}{d}\int LP\ x\ 10^{\frac{-Ax}{d}} = \frac{LP}{d}\int 10^{\frac{-Ax}{d}}$$

$$by\ substitution \qquad u = \frac{-Ax}{d} \qquad du = \frac{-A}{d} dx$$

$$P = \frac{LP}{d}\int -\frac{d}{A} 10^{u}\, du = -\frac{LP}{A}\int 10^{u}\, du$$

$$P = -\frac{LP}{A}\left[\frac{10^{u}}{\ln 10}\right] + C = -\frac{LP}{A}\left[\frac{10^{\frac{-Ax}{d}}}{\ln 10}\right] + C$$

Calculating over the beam path (d = 1 cm), i.e. from 0 to d,

Equation 3.3

$$P = LP\frac{(1 - 10^{-A})}{A \ln 10}$$

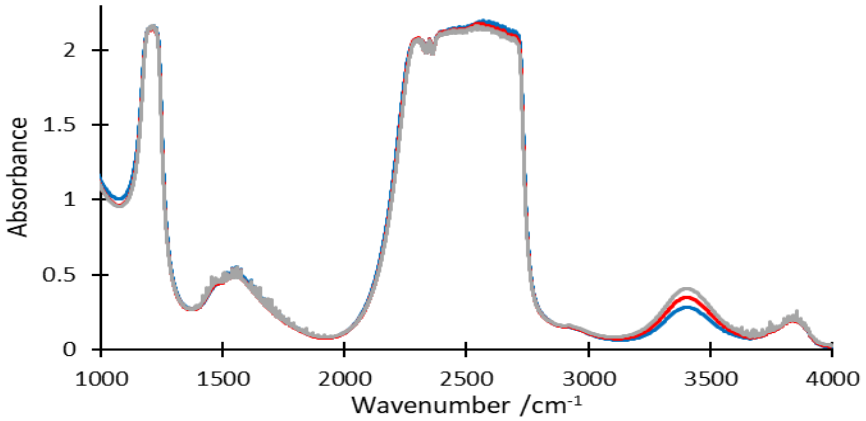

Figure A3. 1 - FTIR spectra of AuNPs in D_2O showing the increase of HOD content in the sample over six months. (Blue solid line – just synthesised, Red solid line –2 months later, and Grey solid line – 6 months later)

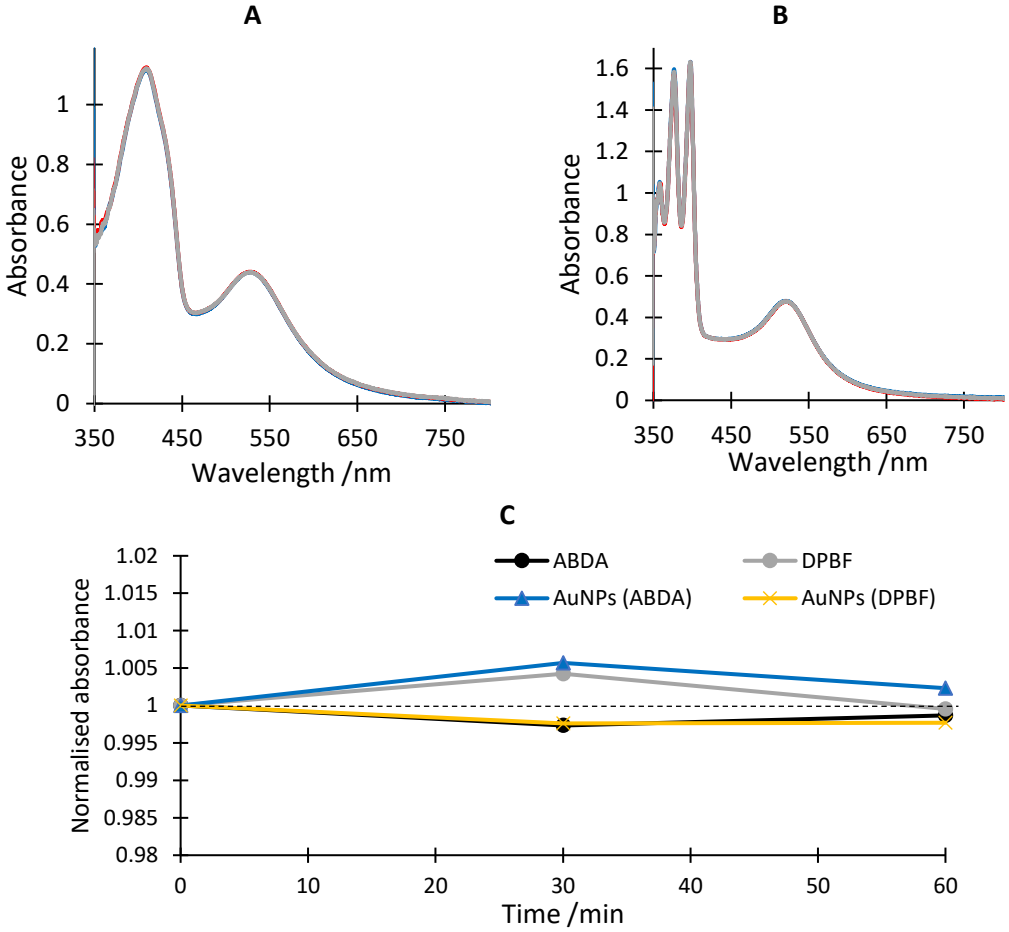

Figure A3. 2 - A) and B) Absorbance spectra of DPBF and ABDA in the presence of AuNPs. The absorbance spectra were taken while keeping the solutions in the dark with 30 minutes intervals to a maximum period of 60 minutes. C) Variation of the normalised DPBF (grey) and ABDA (black) absorbance at 410 (A) and 400 nm (B), respectively, and variation of the normalised AuNPs absorbance in the ABDA and DPBF solution (blue and yellow, respectively) at 532 nm obtained from both spectra (A and B) for the conditions described for A and B. The solution stability was checked in 30 minutes intervals. The dashed line shows a line at y=1 as a guide to the eye.

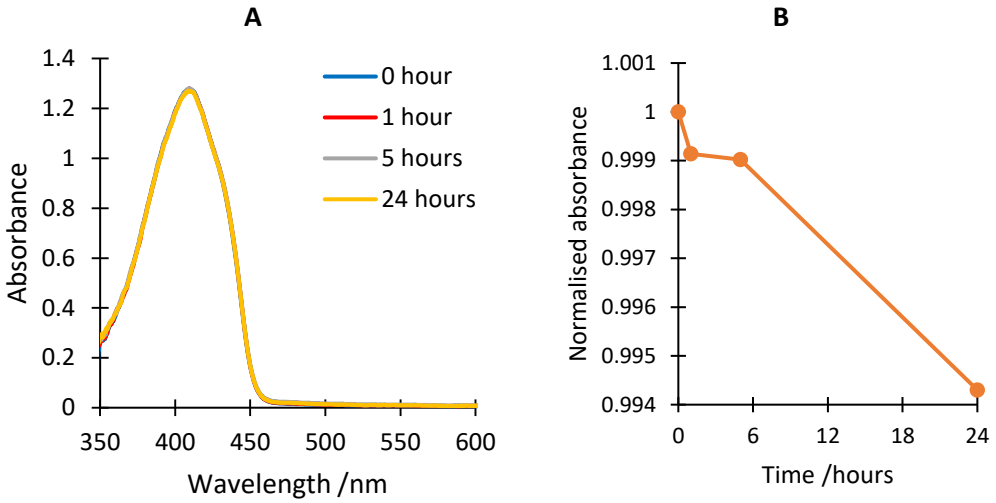

Figure A3. 3 – A) Absorbance spectra of DPBF in air-saturated 50/50 (v/v) EtOH/H_2O in the absence of laser irradiation obtained in a time frame of 24 hours and B) Variation of DPBF absorbance at 410 nm for the same time scale, normalised to absorbance at t=0.

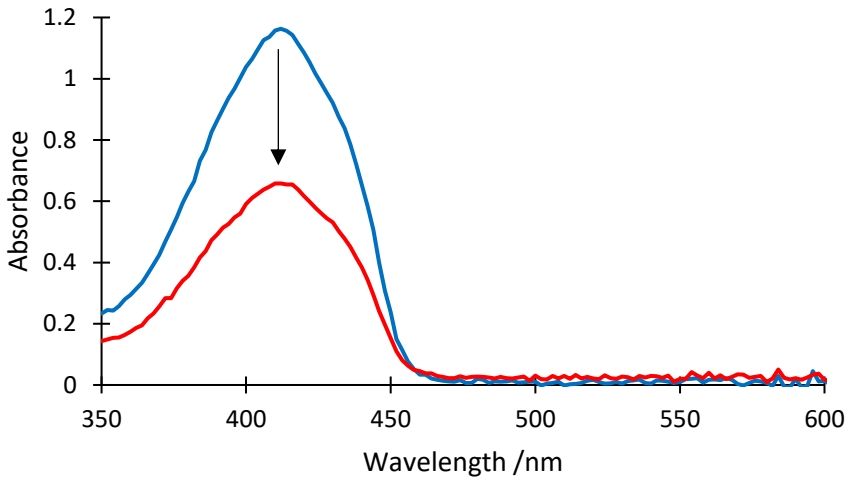

Figure A3. 4 – Bleaching of DPBF absorbance in the absence of irradiation in a 40/60 (v/v) EtOH/H_2O solution (air-saturated). The absorbance spectra of DPBF was taken within 10 minutes apart. The arrow indicates the direction of change over 10 minutes while the solution was kept stirring in the dark.

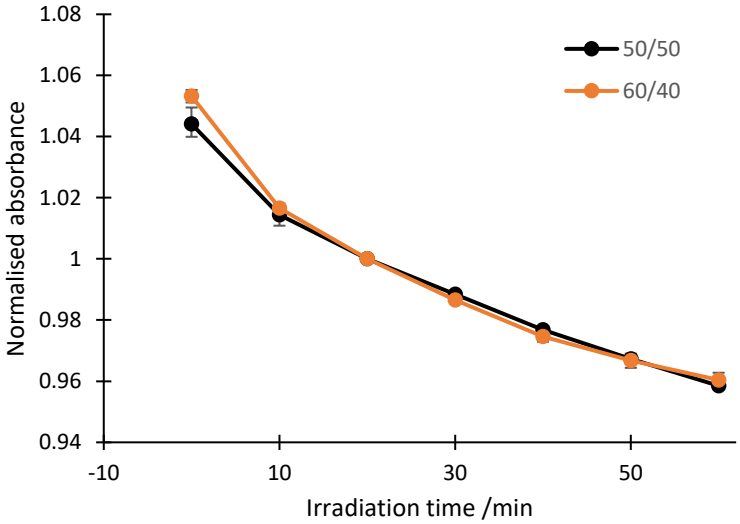

Figure A3. 5 – Variation of the normalised DPBF absorbance at 410 nm of several irradiation experiments in different air-saturated EtOH/H_2O solvent ratios, upon CW-irradiation at 532 nm, 1W. Blackline – 50/50 (v/v) Ethanol/H_2O – Average of seven experiments, and orange line – 60/40 (v/v) Ethanol/H_2O – Average of five experiments. The error bars show the standard error. The error bars are smaller than the symbol size for most points after 20 minutes.

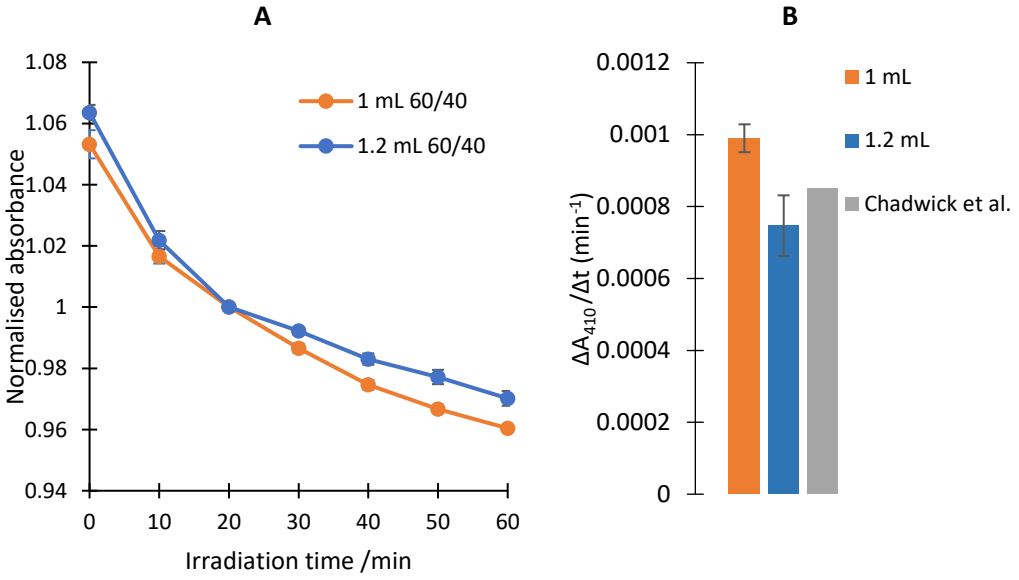

Figure A3. 6 - A) Variation of the DPBF absorbance at 410 nm, normalised at 20 min, in air-saturated solutions in 60/40 (v/v) EtOH/H_2O of several measurements of 1 and 1.2 mL, upon CW-irradiation at 532 nm, 1W. Orange line – 1 mL – average of five measurements, and blue line – 1.2 mL – average of two measurements. B) Bar chart showing the variation of the normalised DPBF absorbance (measured at 410 nm) per minute, i.e. $\Delta(A/A\ (20\ min))/\Delta t$ under the conditions described previously, as well as a comparison with the normalised DPBF absorbance reported by Chadwick *et al.*.[1] The error bars show the standard error. The error bars (in A) are smaller than the symbol size for most points after 20 minutes. [10]

[1] Chadwick, S. J.; Salah, D.; Livesey, P. M.; Brust, M.; Volk, M. Singlet Oxygen Generation by Laser Irradiation of Gold Nanoparticles. *J. Phys. Chem. C* **2016**, *120*, 10647

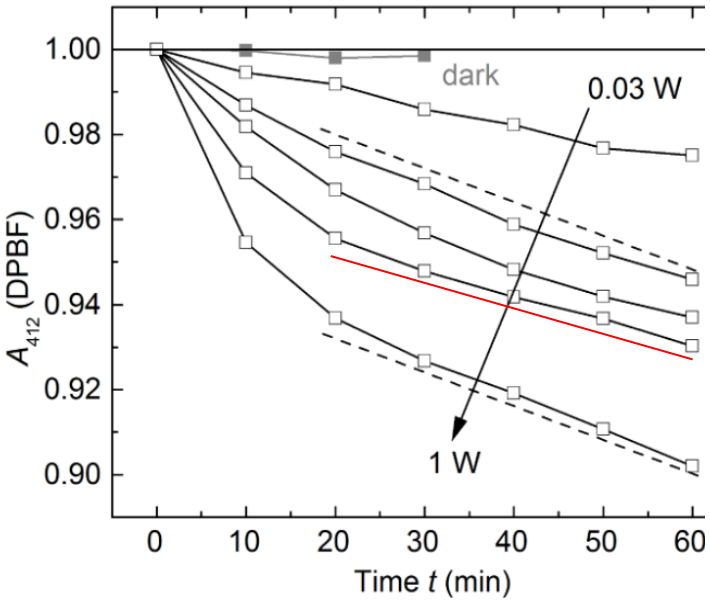

Figure A3. 7 - Taken from Chadwick *et al.*, SI.[1] Variation of the normalised DPBF absorbance at 412 nm in the absence of AuNPs under CW-irradiation at 532 nm at different laser powers (0.03, 0.1, 0.2, 0.5, 1 W). The solid red line was added here to highlight the results for 500 mW irradiation power.

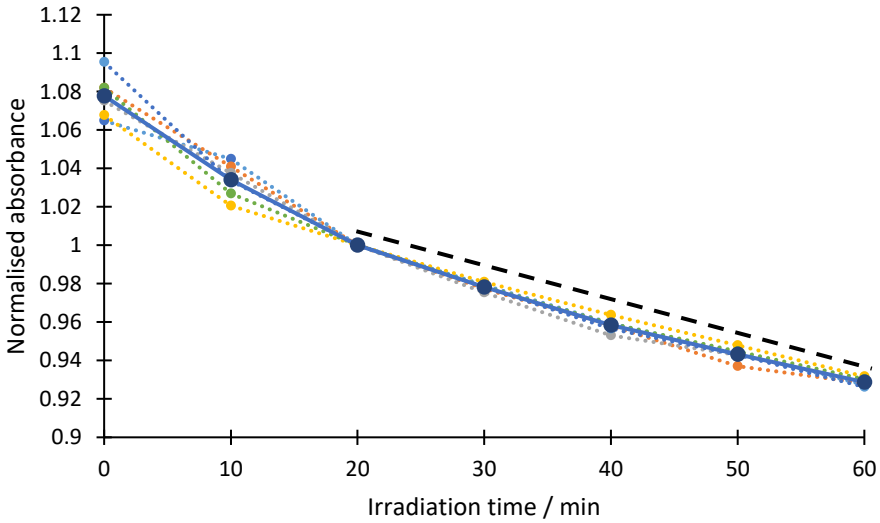

Figure A3. 8 - Variation of the DPBF absorbance at 410 nm, normalised at 20 min, upon CW-irradiation at 532 nm, 1 W, 50/50 (v/v) EtOH/D_2O; shown are six measurements (dotted lines) as well as the average of the six experiments (thick solid blue line). The absorbance of DPBF was normalised at 20 minutes due to the irreproducible variation of DPBF absorbance during the initial irradiation period. The dashed line highlights the linearity of the second, reproducible, phase present after 20 minutes of irradiation.

[1] Chadwick, S. J.; Salah, D.; Livesey, P. M.; Brust, M.; Volk, M. Singlet Oxygen Generation by Laser Irradiation of Gold Nanoparticles. *J. Phys. Chem. C* **2016**, *120*, 10647

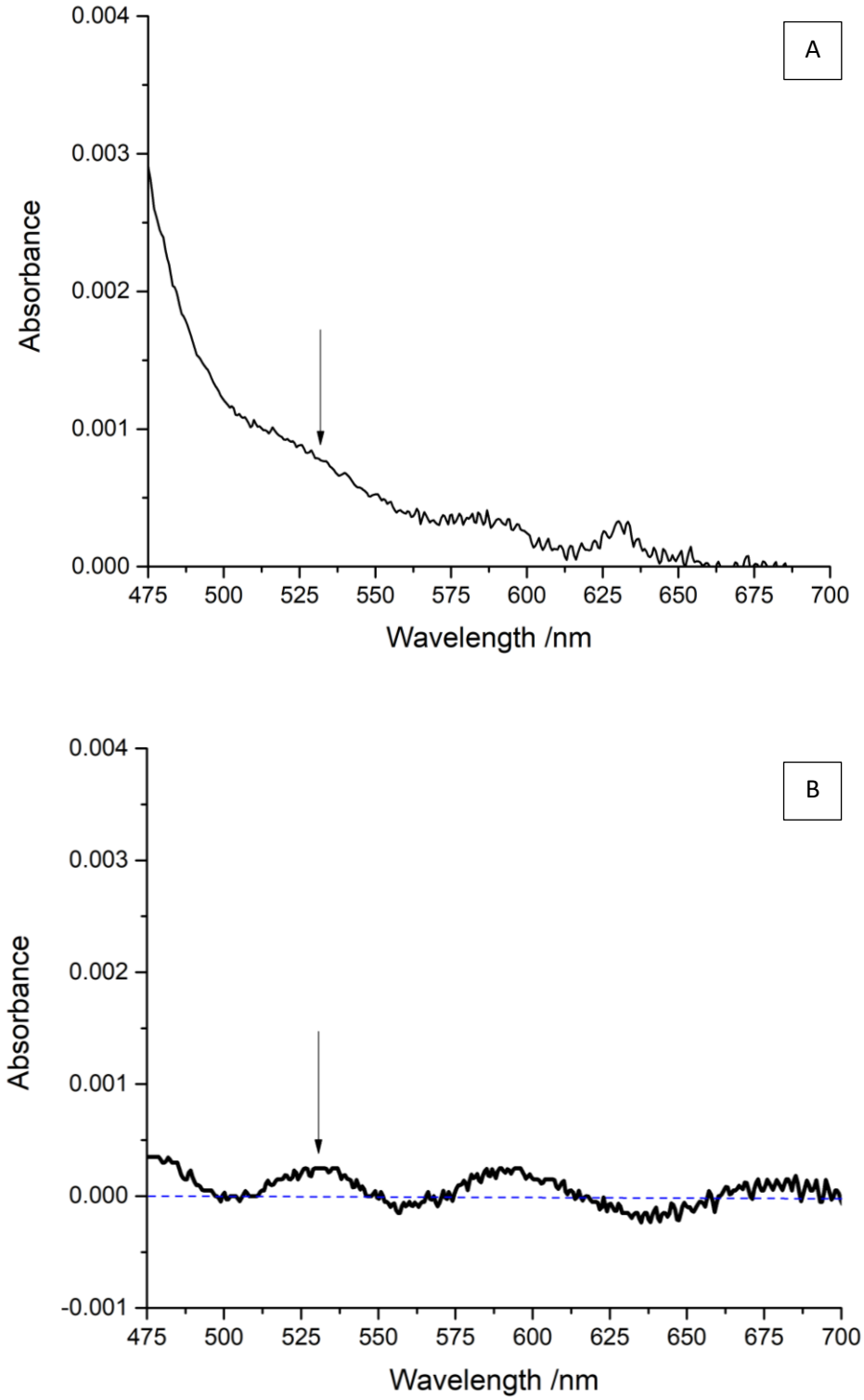

Figure A3. 9 – Average of four and two independent UV/Vis spectra of A) DPBF [0.04 mM – Abs = 1 at 410 nm] in 50/50 (v/v) EtOH/H_2O and B) ABDA [0.07 mM – Abs = 0.8 at 398 nm] in D_2O, respectively. The arrow points the laser irradiation wavelength (532 nm). The concentration of DPBF and ABDA used for these experiments is similar to the normal DPBF and ABDA concentration used in the irradiation experiments. These spectra were taken with a PerkinElmer UV/Vis Spectrometer Lambda 25. The blue dashed line shows a line at y=0 as a guide to the eye.

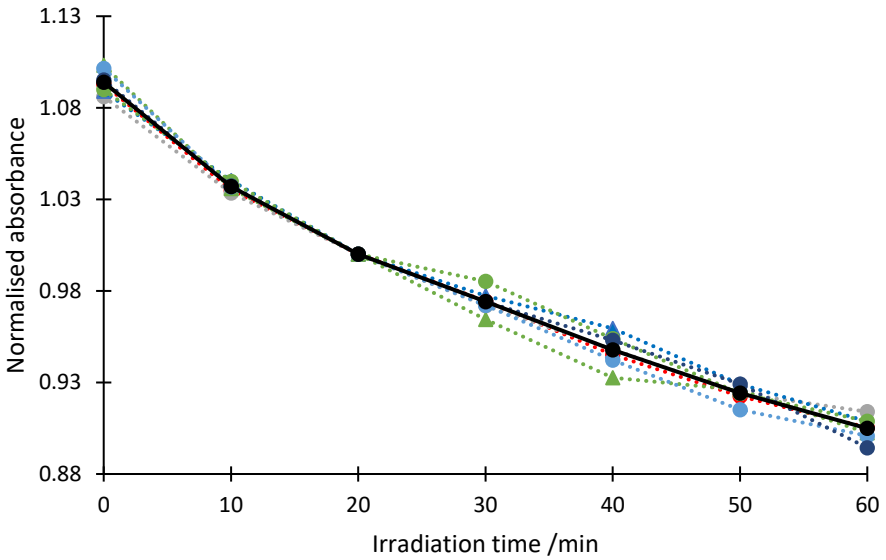

Figure A3. 10 - Variation of the DPBF absorbance at 410 nm, normalised at 20 min, upon CW-irradiation at 532 nm, 1 W, 50/50 (v/v) EtOH/D_2O in the presence of 15 nm AuNPs; shown are seven measurements (dotted lines) as well as the average of the seven experiments (thick solid black line). The absorbance of DPBF was normalised at 20 minutes due to the unpredictable variation of DPBF absorbance during the initial irradiation period.

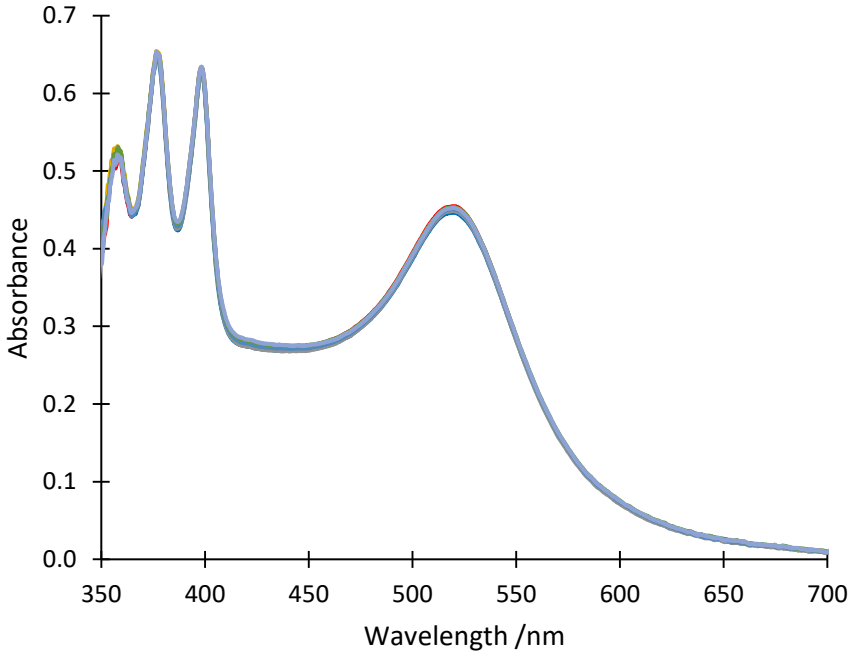

Figure A3. 11 – UV-Vis absorption spectra of N_2 saturated (1 bar) ABDA solution during CW-irradiation at 532 nm, 3 W, in D_2O, in the presence of 16 nm AuNPs. Absorbance spectra were taken with 10 minutes intervals to a maximum irradiation period of 60 minutes.

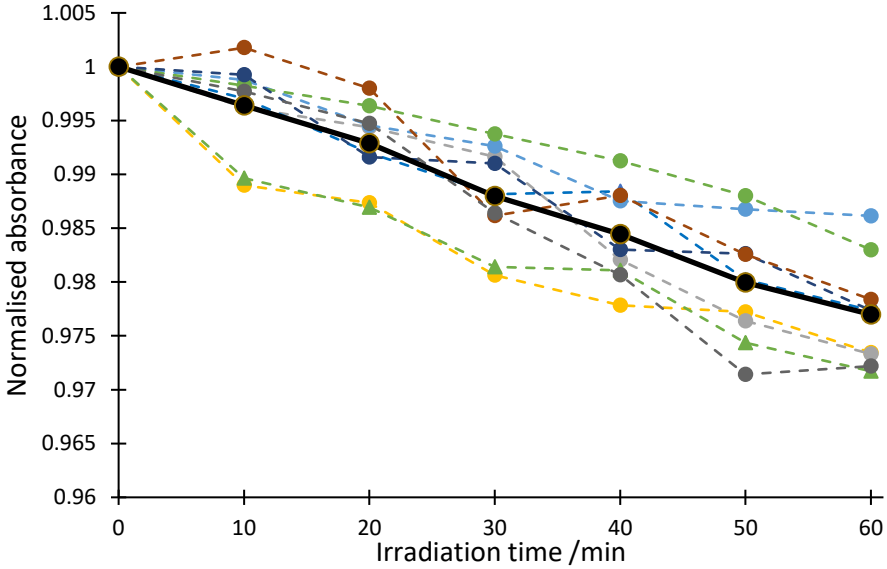

Figure A3. 12 - Variation of the ABDA absorbance at 400 nm, normalised at the start of the irradiation, upon CW-irradiation at 532 nm, 3 W, in O_2-saturated D_2O in the presence of 16 nm AuNPs; shown are nine measurements (dotted lines) as well as the average of the nine experiments (thick solid black line).

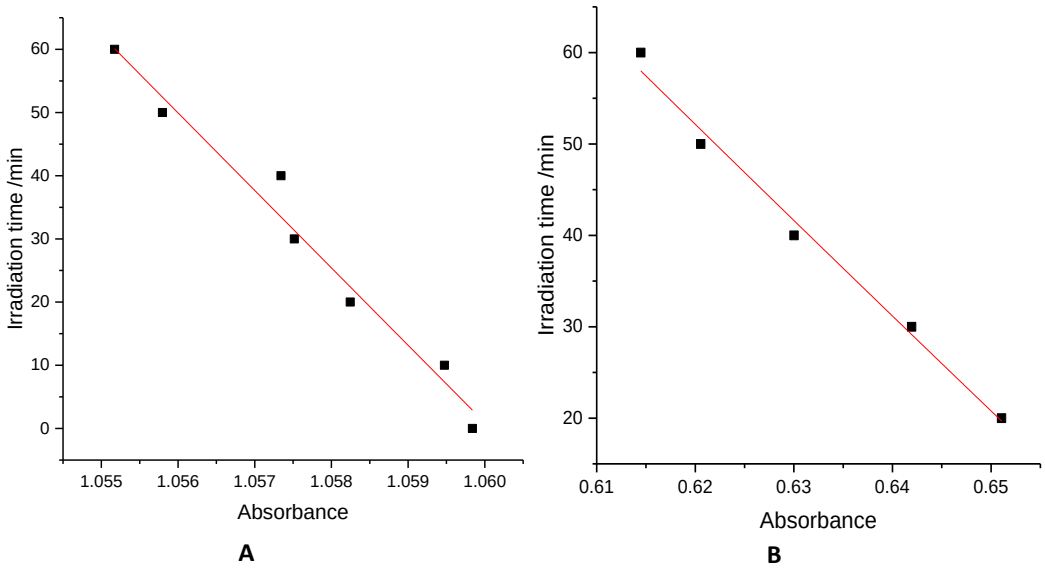

Figure A3. 13 – Fit of example results of the photobleaching of ABDA(A) and DPBF(B) in air-saturated 50/50 (v/v) EtOH/D_2O upon CW-irradiation at 532 nm in the presence of AuNPs with 3 and 1 W, respectively. Shown here is the irradiation time vs. absorbance of ABDA (398-399 nm) and DPBF (408-411 nm). The red line shows the fit of the data using Equation 3.4 with parameter C_3 set to 1.35 and 1 (ABDA and DPBF, respectively). C_2 was calculated for each solvent and probe using the $^1O_2$ lifetimes ($=1/k_0$) shown in Table 2.2, and the k_r and extinction coefficient values determined in chapter 2 (see Table 2.4 and 2.3, respectively).

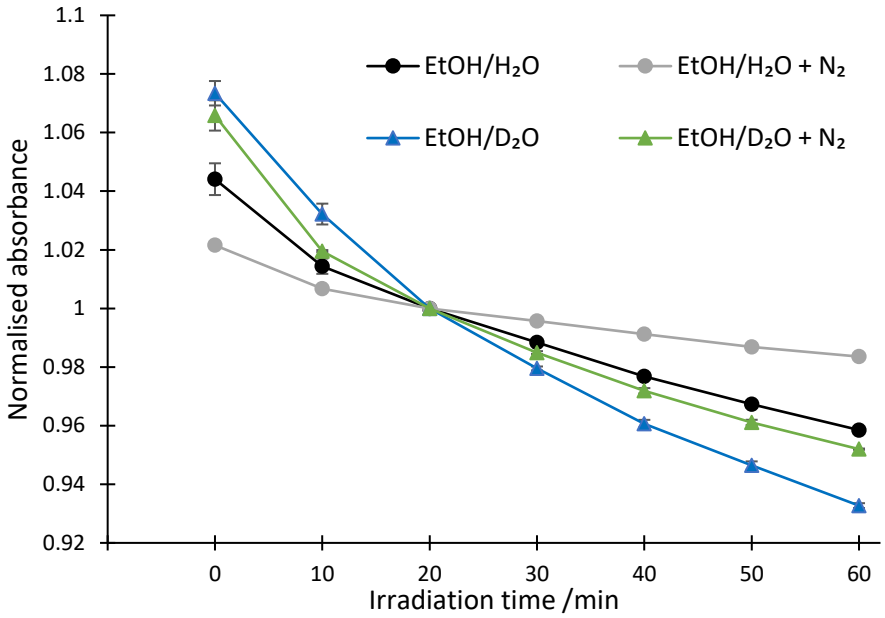

Figure A3. 14 –Variation of the normalised DPBF absorbance at 410 nm in air-saturated solutions in 50/50 (v/v) EtOH/H_2O (average of seven experiments) and N_2 saturated solutions in 60/40 (v/v) EtOH/H_2O (three experiments) and air and N_2 saturated solutions in 50/50 (v/v) EtOH/D_2O (six and two experiments, respectively) upon CW-irradiation at 532 nm, 1 W. The error bars show the standard error. The error bars are smaller than the symbol size for the points after 20 minutes.

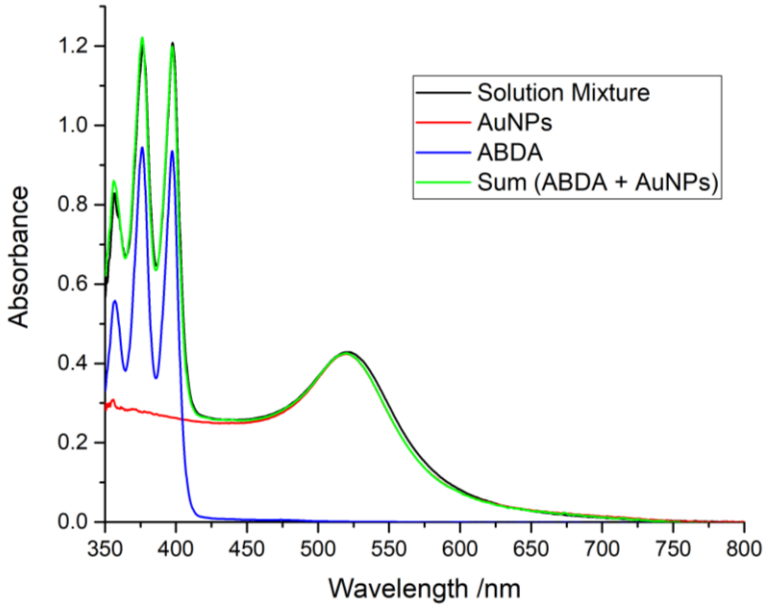

Figure A3. 15 – Absorbance of the individual spectra of AuNPs and ABDA (solid red and blue line), the absorbance spectrum of ABDA in the presence of AuNPs (solid black line), and the sum of the two individual spectra (solid green line), i.e. AuNPs and ABDA alone, scaled accordingly to match the solution mixture spectra. Here, we show that the absorbance spectrum of the solution mixture of DPBF and AuNPs are the sum of the two individual spectra.

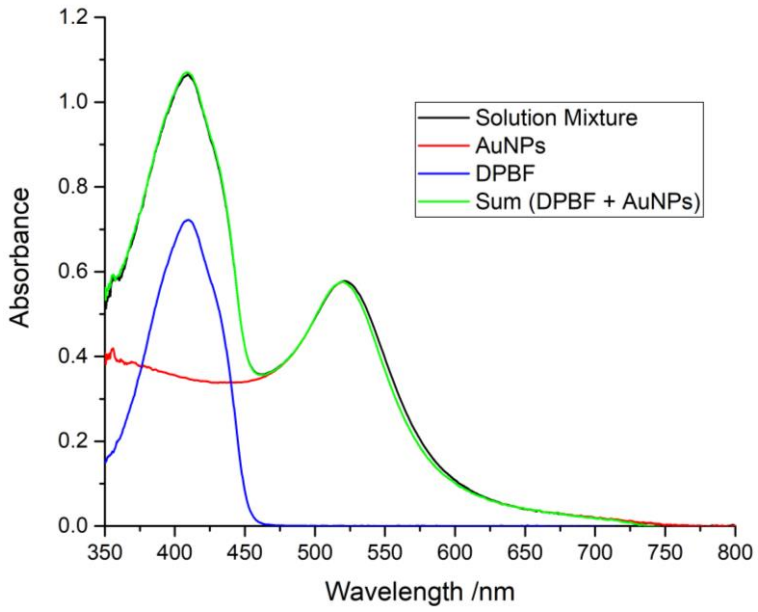

Figure A3. 16 – Absorbance of the individual spectra of AuNPs and DPBF (solid red and blue line), the absorbance spectrum of DPBF in the presence of AuNPs (solid black line), and the sum of the two individual spectra (solid green line), i.e. AuNPs and DPBF alone, scaled accordingly to match the solution mixture spectra. Here, we show that the absorbance spectrum of the solution mixture of DPBF and AuNPs are the sum of the two individual spectra.